STUDIES ON THE RAPID STRAINING ELECTRODE BEHAVIOR OF IRON, NICKEL AND THEIR CHROMIUM ALLOYS IN HIGH TEMPERATURE AND HIGH PRESSURE AQUEOUS SOLUTIONS

（高温高圧水溶液中における鉄、ニッケルおよびそれらの
クロム合金の急速ひずみ電極挙動に関する研究）

1986

SHINJI FUJIMOTO

STUDIES ON THE RAPID STRAINING ELECTRODE BEHAVIOR OF IRON, NICKEL AND THEIR CHROMIUM ALLOYS IN HIGH TEMPERATURE AND HIGH PRESSURE AQUEOUS SOLUTIONS

（高温高圧水溶液中における鉄、ニッケルおよびそれらのクロム合金の急速ひずみ電極挙動に関する研究）

1986

SHINJI FUJIMOTO

Preface

The works in this thesis were carried out under the guidance of Professor Toshio Shibata at The Department of Metallurgical Engineering, Osaka University for five years since 1982.

The object was to examine the initial anodic process of iron, nickel and their chromium alloys in high temperature and high pressure aqueous solutions in order to obtain the basic electrochemical information about corrosion behavior of iron and nickel base alloys in the high temperature and high pressure water environments.

November 1986 Shinji Fujimoto

Acknowledgements

The autor would like to express sincere appreciation to Professor T. Shibata of The Department of Metallurgical Engineering, Osaka University for his kind guidance, constructive discussion and encouragement throughout this work.

The auther also offers his appreciation to Professor Z. Morita and Professor Z. Kozuka of The Department of Metallurgical Engineering, Osaka University and Professor S. Nenno of The Department of Materials Science and Engineering, Osaka University for their constructive discussion and the preliminary examination of this thesis.

The author is very grateful to Dr. S. Taniguchi of The Department of Metallurgical Engineering, Osaka University for his helpful comments and suggestions. The author also wishes to thank Mr. J. Nakata of Osaka University for his constant help to the present studies.

Particular thanks are extended to Technical Research Laboratories, Sumitomo Metal Industries, Ltd. for provision of the specimen materials and to Hanshin Research & Development Laboratories, Nisshin Steel Co., Ltd. for the Auger analysis.

Finally, the author would like to thank his parents for their understanding and encouragement.

Contents

CHAPTER I

General Introduction

1.1 Corrosion Failures in High Temperature and High Pressure Water Environments

Material performance in plant industries is an important factor determining the reliability of the whole system. The utilization of metallic materials in high temperature and high pressure water environments is comprised in power generating plants, such as, nuclear[1], geothermal[2] and also ordinary thermal power generators[1],[3]-[4]. An extremely high reliability has been demanded particularly for nuclear power plants, because their failure will lead to a great economic loss and also to a social uneasiness.

In the nuclear power generators, mainly iron and nickel base alloys[5],[6], and also zirconium alloys are used in the high temperature, high pressure and high purity water. Austenitic stainless steels[7]-[9] are used for the cooling water tubing system in the boiling water reactor (BWR) plants, the commercial operation of which have been started early in 1960's. The failure of cooling water tubing was first detected in 1965 at Dresden-1 reactor, USA[10]. The failure was attributed to stress corrosion cracking (SCC) as a result of localized stress, sensitization of material and dissolved oxygen. At that time, the SCC problem of austenitic stainless steels has not become of serious interest. Since the intergranular stress corrosion cracking (IGSCC) of cooling water tubing made of stainless steel was detected for Dresden-2 reactor in 1974[11], similar failures were found in many reactors in the world including USA and Japan.

After that, extensive studies have been performed on SCC of austenitic stainless steel in BWR environment for understanding and developing the measures to prevent it[8],[14],[15]. Development of nuclear grade SUS316 steel[16], improved welding procedure[13],[17] and also strict control of water chemistry[13] have given effective countermeasures to the SCC problem of austenitic stainless steels in this environment[8],[18].

In the pressurized water reactor (PWR), high nickel alloys have been used as steam generator (SG) tubing, which forms a pressure boundary between the primary water and secondary side[19]-[24]. SG tubes of Alloy 600 are known to suffer with SCC and intergranular attack (IGA) from the secondary side. Few cases of SCC from primary side have been also reported[25]. SCC and IGA of high nickel alloys have been closely related to water treatment[22],[26],[27]. However, an exact understanding of mechanism has not yet been achieved to date[5],[6],[8]. The development of candidate materials for the high performance has been in progress[29]-[31]. In the case of PWR, the denting phenomena[22],[32],[33] are also an important corrosion trouble in the steam generator ; a thick magnetite layer deposits and grows in a crevice between SG tubing and a tube supporting plate made of carbon steel. These voluminous corrosion products press SG tubes to cause SCC with an acceleration of corrosion within the crevice[33],[34]. It is emphasized that the water chemistry plays an important role to control the phenomena.

As stated above, a considerable number of research has been conducted on corrosion attacks of iron and nickel base commercial alloys in this environment in order to establish practical means to prevent them. However, there have been few studies to examine the interaction of materials with the environments, because of

the experimental difficulty. The interaction here includes the basic electrochemical process of iron, nickel, stainless steels and high nickel alloys in high temperature and high pressure water environment.

1.2 Previous Studies on the Corrosion Behavior of Iron and Nickel Base Alloys in High Temperature and High Pressure Water Environments

Many corrosion researches have been performed on various materials, such as, iron, nickel, aluminum and zirconium alloys, in connection with steam-power boiler, high temperature hydrometallurgy, oil drilling, fuel cell, high temperature chemical reactor, and others[3],[35]. The basic electrochemical properties, for example, corrosion rate, solubility of metal and its oxide, and structure of oxide films have been investigated for a long time[36]-[39]. However, studies with electrochemical techniques have been conducted after the development of the reference electrode for high temperature and high pressure aqueous solution[40]-[44], because experiments in this environment are very difficult compared with that at room temperature and atmospheric pressure. At the international conference on "High Temperature High Pressure Electrochemistry in Aqueous Solution" in 1973 at Surrey, England[45], the attendants discussed the electrochemical researches and experimental techniques for high temperature water environments that were obtained until that time. It has been recognized that the corrosion behavior in high temperature and high pressure water is quite different and is not readily estimated from the knowledge obtained at room temperature.

It is generally recognized that SCC is caused by the

conjoint action of stress, environment and materials factor[46]. The residual stress and sensitization of material at heat affected zone (HAZ) due to welding, and dissolved oxygen (DO) of a high concentration are considered to be mainly responsible for IGSCC of stainless steels in high temperature and high pressure pure water[14],[15].

SCC of stainless steel is usually explained by an active path corrosion (APC) mechanism[47]-[49], i.e., SCC propagates by the preferential anodic dissolution at crack tip, as illustrated in Fig.1-1[48]. Therefore, the electrochemical reaction is an important factor to discuss the SCC phenomenon. SCC is liable to occur at some specified potential zones as described in Fig.1-2[50], which also illustrates various types of corrosion at each potential. The passive film seems to be unstable at these potentials in which SCC is prone to occur. The corrosion potential is determined by the dissolved oxygen (DO) concentration[51]-[53]. Therefore, the control of DO concentration is important to prevent SCC.

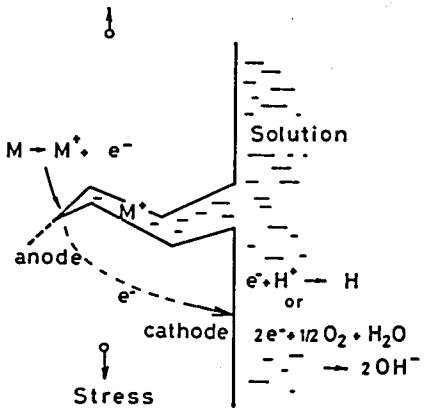

Fig.1-1 Schematic drawing of crack propagation by APC mecahnism in SCC.

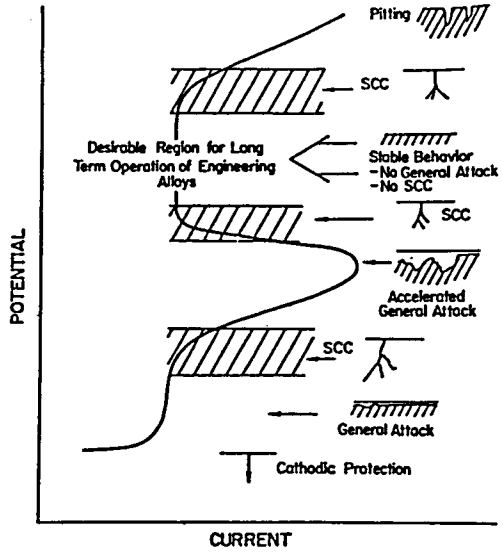

Fig.1-2 Schematic polarization diagram indicating corrosion types and SCC potential regions[50].

According to the APC theory, SCC propagates when anodic dissolution is localized at a crack tip[54]. In other words, the localized dissolution can be expected, if the dissolution at the crack tip is fast and that on the side wall of the crack is suppressed. Such a condition for stainless steels seems to be attained by sensitization, i.e., the precipitation of chromium carbides in a specific temperature range from 820 to 1120 K forms the chromium depleted zone along grain boundaries[55]. The passive film formed on the chromium depleted zone is less protective for dissolution. Then, SCC propagates along chromium depleted grain boundaries.

SCC and IGA of high nickel alloys occur under various conditions[5],[6],[19]. Condensed alkaline species have been supposed to be responsible for IGA and SCC[19],[56],[57]. The potential regions of SCC and IGA as commonly observed in caustic solutions are illustrated in Fig.1-3[58] with the polarization

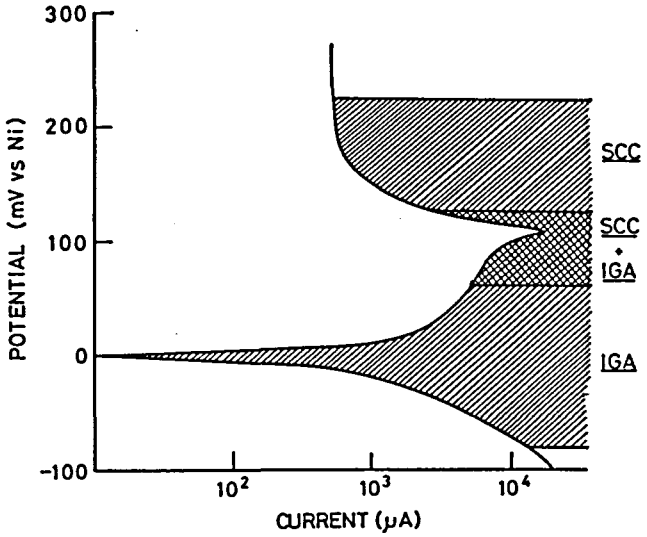

Fig.1-3 Superimposition of the potential areas for IGA and SCC of Alloy 600 on its polarization curve in 10 % NaOH + 1 % Na_2CO_3 solution at 573 K. Specimen area 1 cm^2 (58).

curve. The IGA zone includes not only anodic but also cathodic potential region. On the other hand, Coriou et al.[59] reported that Alloy 600 is susceptible to IGSCC in deaerated high temperature pure water. Moreover, a local acidification within crevice promotes active dissolution of chromium depleted grain boundary to cause IGSCC[60]. The presence of chromium depleted zone is considered to be not essential for SCC[24),(61),(62], contrary to SCC of stainless steels. The alloy microstructure has been known to play an important role in determining the corrosion resistance of high nickel alloys[19),(22)-(24)]. It is now generally accepted that thermal treatments, which control the grain size and structure of precipitates, determine the susceptibility to SCC and IGA. Nevertheless, the electrochemical mechanisms to cause IGSCC and IGA for high nickel alloys have not been understood yet consistently[5),(6),(25)].

As described above, not sufficient studies have been conducted on the basic electrochemical behavior of iron and nickel base alloys. The dissolution and film formation behavior of pure metals, and the effect of chromium addition to them have to be investigated in various environments, because these informations will provide a clue to understand the mechanism of localized attack.

1.3 Purpose and Arrangement of the Thesis

Localized corrosion attacks, including SCC, IGA, pitting, and corrosion fatigue (CF), are caused by breakdown of the passive film. In the case of SCC and CF, the passive film is broken mechanically. For IGA and pitting, on the other hand,

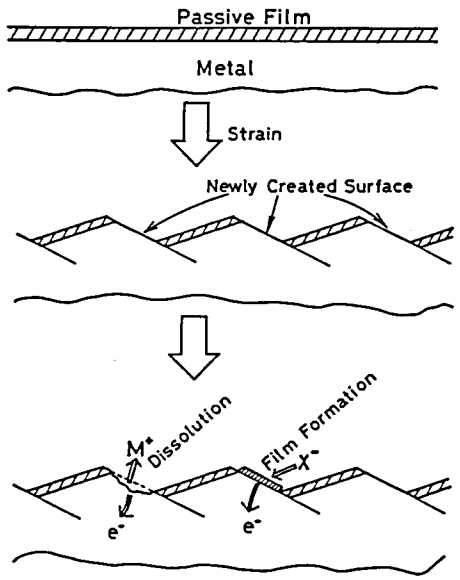

Fig.1-4 Schematic drawing of the dissolution and the film formation on the newly created surface emerged by straining.

some aggressive anions, such as Cl^- and SO_4^{2-}, break the passive film locally, and such film breakdown also gives an initiation site for SCC and CF. Whether these localized corrosion propagates or not is determined by the both rate of film breakdown and its repair, namely, repassivation.

The effect of alloying element and environmental factors, such as, potential, temperature and anion on the electrochemical behavior on bare surface, which is emerged by film breakdown, can be investigated by a rapid straining electrode technique[63)-67)]. Figure 1-4 illustrates the emergence of the newly created surface by straining and the following active dissolution and repassivation. The historical background and the principle of the rapid straining electrode technique are presented in the next chapter 2.1.

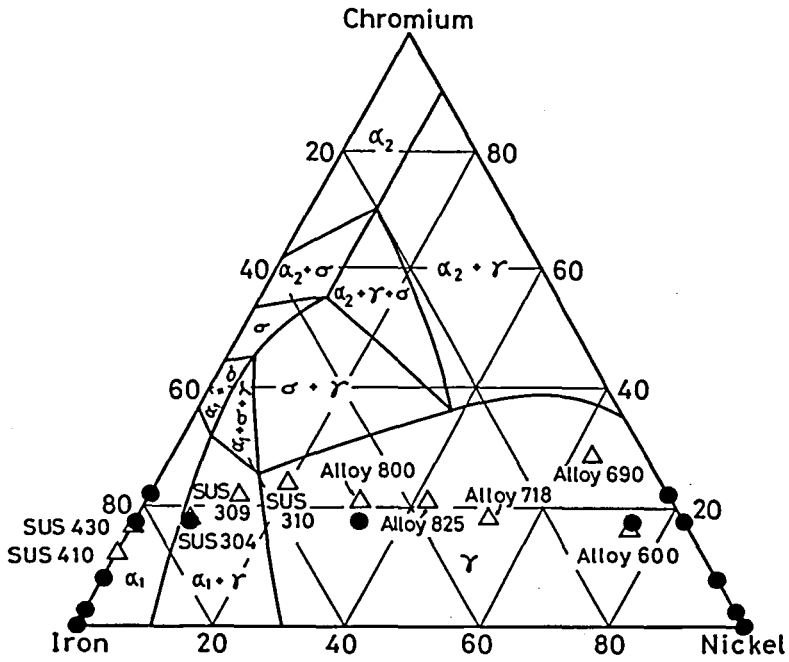

Fig.1-5 The Fe-Cr-Ni ternary diagram at 673 K, showing the locations of important commercial alloys and materials investigated in this work (●).

The purpose of this work is to investigate the dissolution and the subsequent film formation of iron, nickel and their chromium alloys by means of the rapid straining electrode technique.

The materials investigated in this work are Fe and Ni, and Fe-Cr and Ni-Cr binary alloys, and Fe-Cr-Ni ternary alloys. Their compositions are indicated in the Fe-Cr-Ni ternary diagram at 673 K presented in Fig.1-5, which also shows the location of important commercial alloys. The Fe-Cr alloys and Ni-Cr alloys including pure metals used in this work are ferritic and austenitic phase, respectively. Three Fe-Cr-Ni alloys of 18 mass% chromium are prepared as ternary alloy specimens, because many commercial alloys contain about 18 mass% chromium, as shown in this figure.

This thesis consists of the following nine chapters.

Chapter I of general introduction will be followed by Chapter II which describes the historical background and the principle of the rapid straining electrode and also the experimental apparatus used in this work.

Chapters III and IV deal with the straining electrode behavior of iron and nickel, respectively, in a sodium sulphate solution. The aggressive action of SO_4^{2-} ion on the breakdown of passivity for these metals is particularly emphasized.

Chapters V and VI deal with the dissolution and film formation mechanisms on the newly created surface of iron and nickel, respectively, in a borate buffer solution, because the SO_4^{2-} containing solution is not suitable environment for the basic investigation on the anodic behavior of iron and nickel, as demonstrated in the previous two chapters.

In Chapter VII, the straining electrode behavior of the Fe-

Cr and Ni-Cr alloys are examined in the borate buffer solution, in order to discuss the effect of chromium on the dissolution and the film formation of iron and nickel base alloys. Moreover, the composition of films formed on these alloys, obtained with Auger electron spectroscopy, is shown in order to discuss the repassivation behavior in terms of the film composition.

In Chapter VIII, the straining electrode behavior of Fe-Cr-Ni ternary alloys is examined in order to discuss the role of alloying elements for commercial alloys, and results of Auger analysis of films formed on these alloys are also described.

Finally, the concluding summary will be given in Chapter IX.

REFERENCES

(1)K. Tanno and A. Minato : Bull. of Japan Inst. of Metals, 22 (1983), 809.

(2)I. Matsushima : Bull. of Japan Inst. of Metals, 24 (1985), 993.

(3)k. Tanno and N. Kawashima : Seisan-to-Gijutsu (The production & Technique), 21 (1969), 23.

(4)H. Nishiyama : Boshoku Gijutsu, 31 (1982), 473.

(5)M. Kowaka : Tetsu-to-Hagané, 60 (1974), 427.

(6)S. Abe : Bull. of Japan Inst. of Metals, 16 (1977), 15.

(7)S. Szklarska-Smialowska and G. Cragnolino : Corrosion, 36 (1980), 653.

(8)M. Akashi : Boshoku Gijutsu, 29 (1980), 142.

(9)R. L. Cowan and G. M. Gordon : Proc. Int. Conf. on Stress Corrosion Cracking and Hydrogen Embrittlement of Iron Base Alloys, NACE (1978), p.1023.

(10)J. P. Higgens : Nuclear News, 11 (1968), 37.

(11)EPRI, Chicago Meeting, March, 4 (1975).

(12)H. H. Klepfer et al : "Investigation of Cause of Cracking in Austenitic Stainless Steel Piping", General Electric Company Report, No. NEDO 21000-1 (1975).

(13)Y. Ando : Genshiryoku Kogyo (Nuclear Engineering), 24, No.9 (1978), 9.

(14)S. H. Bush and R. L. Dillon : Proc. Int. Conf. on Stress Corrosion Cracking and Hydrogen Embrittlement of Iron Base Alloys, NACE (1978), p.61.

(15)M. Kowaka : Zairyo, 25, (1976), 1057.

(16)M. Kowaka, H. Nagano, K. Yoshikawa, M. Miura, K. Ohta and S. Nagata : Karyoku Genshiryoku Hatsuden (The Thermal and Nuclear power), 32 (1981), 1303.

(17)M. J. Povich and R. E. Smith : Corrosion/79, Paper No.235, NACE (1979).

(18)EPRI WS 79-174, Proc. Seminar on Countermeasures for Pipe Cracking in BWRs, (1980).

(19)D. Van Rooyen : Corrosion, 31 (1975), 327.

(20)C. F. Cheng : J. Nuclear Materials, 56 (1975), 11.

(21)R. Gransey : Nuclear Energy, 18 (1979), 117.

(22)S. J. Green and L. P. N. Paine : Nucl. Tech., 55 (1981), 10.

(23)Ph. Berge and J. R. Donati : Nucl. Tech., 55 (1981),88.

(24)R. Bandy and D. Van Rooyen : Corrosion, 40 (1984), 425.

(25)C. M. Owens : Materials Performance-NACE, 25 (1986), 49.

(26)J. R. Weeks : Nucl. Tech., 28 (1976), 348.

(27)W. D. Fletcher and D. D. Malinowski : Nucl. Tech., 28 (1976), 356.

(28)T. S. Bulischeck, D. Van Rooyen : Nucl. Tech., 55 (1981), 383.

(29)A. Sedriks, J. W. Schults, and M. A. Cordovie : Boshoku Gijutsu, 28 (1979), 82.

(30)G. P. Airey, A. R. Vaia and R. G. Aspden : Nucl. Tech. 55 (1981), 436.

(31)V. I. Gerasimov and A. V. Rjabchenkov : Metal Protection, 4 (1968), 441.

(32)R. Gransey : Nucl. Tech., 18 (1979), 117.

(33)G. E. von Nieda, G. Economy and M. J. Wootten : Materials Performance, 20 (1981),38.

(34)R. S. Pathania and E. G. McVey : Materials Performance, 19, July (1980), 34.

(35)T. Mukaibo and S. Masukawa : Denki-Kagaku, 32 (1964), 416.

(36)T. Mukaibo and S. Masukawa : Denki-Kagaku, 32 (1964), 336.

(37)T. Mukaibo, S. Masukawa, M. Maeda and M. Hoshido : Denki-Kagaku, 34 (1966), 388.

(38)M. C. Broom and M. Krulfeld : J. Electrochem. Soc., 104 (1957), 264.

(39)C. F. Cheng : Corrosion, 20 (1964), 341.

(40)T. Fujii : Boshoku Gijutsu, 23 (1976), 257.

(41)D. D. MacDonald : Corrosion, 34 (1978), 75.

(42)K. Sugimoto : Boshoku Gijutsu, 29 (1980), 521.

(43)T. Fujii : Denki-Kagaku, 48 (1980), 424.

(44)K. Tachibana : Boshoku Gijutsu, 34 (1985), 308.

(45)Proc. Int. Conf. on " High Temperature High Pressure Electrochemistry in Aqueous Solutions", Surrey England 1973, NACE-4 (1976).

(46)R. W. Staehle, "Fundamental Aspects of Stress Corrosion Cracking", NACE-1 (1969), p.6.

(47)B. E. Wilde and C. D. Kim : Corrosion, 28 (1972), 350.

(48)B. F. Brown : "Fundamental Aspects of Stress Corrosion Cracking", NACE-1 (1969), p.398.

(49)H. P. Leckie : "Fundamental Aspects of Stress Corrosion Cracking", NACE (1969), p.411.

(50)R. W. Staehle : "Mechanisms of Environment Sensitive Cracking of Materials", Eds. P. R. Swann, E. P. Ford and A. R. C. Westwood, Metals Soc., Guildford, (1977), p.574.

(51)J. Takabayashi and M. Hishida : Proc. EPRI-JPI Symp.B-11 (1978).

(52)M. E. Indigh and A. R. McIlree : Corrosion, 35 (1979), 288.

(53)N. Ohnaka and A. Minato : Boshoku Gijutsu, 34 (1985), 79.

(54)R. M. Latanision and R. W. Staehle : "Fundamental Aspects of Stress Corrosion Cracking", NACE-1 (1969), p.214.

(55)M. Henthone : "Localized Corrosion", ASTM, STP-516 (1972), p.66.

(56)G. J. Teus : Corrosion, 33 (1977), 20.

(57)I. L. W. Wilson and R. G. Apsden : Corrosion, 32 (1976), 193.

(58)R. Bandy and D. Van Rooyen : Proc. 9th Int. Cong. on Metall. Corros., Toront (1984), Vol.2, p.202.

(59)H. Coriou, L. Grall, Y. Le Gall and S. Vettier : 3rd Metallurgy Conference on Corrosion, Saclay (1959), p.161.

(60)D. F. Taylor : Corrosion, 35 (1979), 550.

(61)H. Coriou, L. Grall, C. Mahieu and M. Pelas : Corrosion, 22 (1966), 280.

(62)H. R. Copson, D. Van Rooyen and A. R. McIlree : Proc. 5th Int. Cong. on Metall. Corros., Tokyo (1972), P.376.

(63)N. Ohtani : Bull. of Japan Inst. of Metals, 12 (1973), 233.

(64)T. Murata : Boshoku Gijutsu, 21 (1972), 157.

(65)T. Murata : Boshoku Gijutsu, 22 (1973), 133.

(66)T. Murata : Tetsu-to-Hagané, 60 (1974), 580.

(67)T. Shibata : Boshoku Gijutsu, 33 (1984), 603.

CHAPTER II

Rapid Straining Electrode Test

2.1 Historical Background and Principle of Straining Electrode

Effects of strain on the electrochemical behavior of metals and alloys are long-standing interest[1],[2] in connection with both thermodynamic aspects and practical corrosion problems affected by stress.

Measurements of electrode potential under straining have been conducted since a long time ago[3]-[5]. The change of electrode potential with strain was explained only by the consideration of change in the excess energy from the view point of the thermodynamical equilibrium[5]-[8], because the exact understanding of the meaning of electrode potential had not been established yet. Therefore, the changes in potential actually measured were not in agreement with theoretical predictions[8]. The concept of the mixed potential was first introduced by Wagner and Traud in 1938[9]. Based on the mixed potential theory, the electrode potential is determined by both anodic and cathodic processes, and the electrode potential actually measured is explained kinetically. Eyring et al.[10]-[12] measured the transient of electrode potential with strain for various metal/solution systems. They discussed that the surface film is broken by a strain, which changes reaction rate for both anodic and cathodic processes resulting in shift of electrode potential, and then the potential returns to the initial value because the surface condition returns to the original state. They also measured the changes in current density with time for

straining electrode. Since the potentiostat[13] was developed and introduced to study the effect of stress or strain, the change of the current at a constant potential can be readily analyzed quantitatively, and the effect of strain on the anodic dissolution has been investigated by many authors[14]-[19].

Figures 2-1(a) and (b) are the schematic drawings of the change in the electrode potential in open circuit condition and the change in the current density in a constant potential or

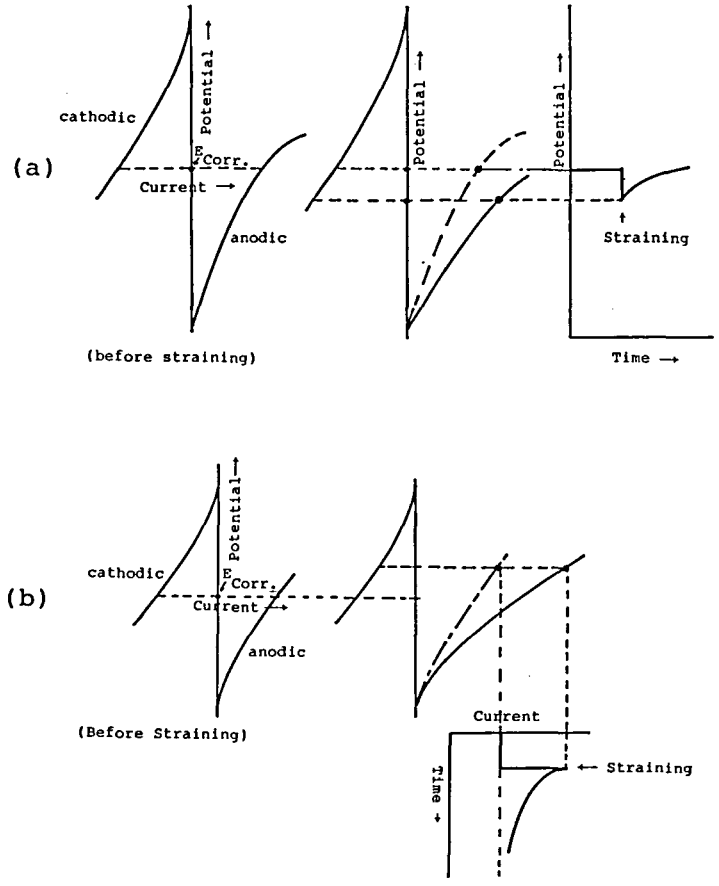

Fig.2-1 Illustration of (a)the change in electrode potential in open circuit condition and (b) the change in current density in potentiostatic condition due to a straining(20).

potentiostatic condition due to a straining, respectively illustrated by Murata[20]. When a straining is given at a open circuit condition, the anodic current increases with the increase in the area of anodic reaction sites which emerge as a newly created surface, and then the electrode potential (corrosion potential $E_{Corr.}$) shifts to less noble. The potential changes to the initial value with the decrease in the anodic current, because the reaction products formed on the newly created surface decrease the anodic reaction rate. On the other hand, the anodic current increases with increasing the area of anodic sites, then decreases with time due to the formation of

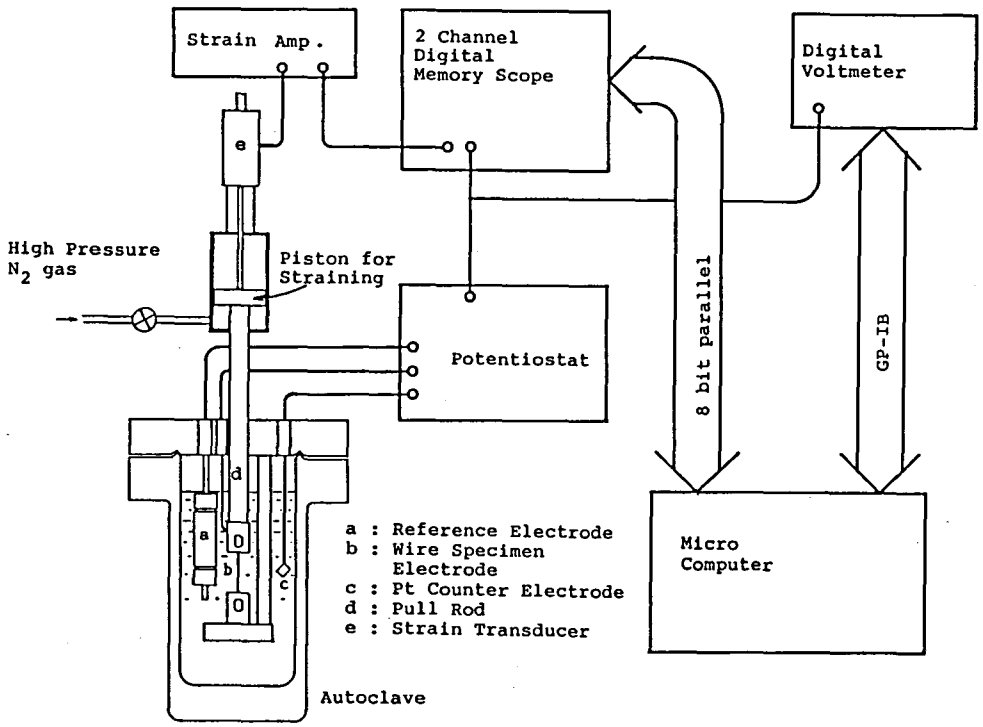

Fig.2-2 Schematic drawing of apparatus for the rapid straining electrode test in high temperature and high pressure aqueous solution.

corrosion products under the potentiostatic condition. When the passive film suppresses anodic dissolution, the increase in anodic current with straining is almost due to dissolution of substrate metal or alloy through the newly created surface, and the decrease in current with time is due to repassivation of the newly created surface. Therefore, the dissolution and film formation behavior on the newly created surface can be analyzed quantitatively by means of the straining electrode technique.

2.2 Apparatus for Rapid Straining Electrode Test in High Temperature and High Pressure Aqueous Solution

Figure 2-2 is schematic drawing of the testing apparatus. It consists of an autoclave system with a device for rapid elongation. A static type autoclave made of SUS316L with a volume of 1570 cm^{-3} was used. A pair of chucks for holding a wire specimen are equipped in the autoclave. The wire specimen of 0.35 mm diameter is attached to the chucks made of SUS316. The details of the chucks with a wire specimen are shown in

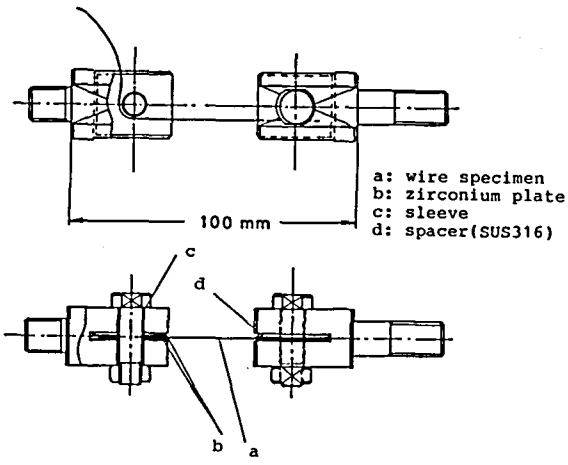

Fig.2-3 Details of the chuks with a wire specimen.

Fig.2-3. Between the chuck and the specimen, zirconia coated zirconium plates are inserted, and the bolts for fixing the specimen also covered with sleeves of the same material, in order to provide electrical insulation between the specimen and the autoclave. The length between the upper and the lower part of the chucks is 30 mm at minimum. Thus, the initial length of specimen exposed to a test solution is 30 mm. The upper part of the chuck is connected to a pull rod made of Hastelloy C. The pull rod passes through the autoclave lid plate with a water cooled pressure balanced fitting seal and is connected to a piston in a cylinder. When the specimen is to be strained, high pressure N_2 gas is introduced into the cylinder, and the piston moves rapidly giving a specified strain produced via an action of a stopper in the cylinder. The amount of strain is measured by a moving strain transducer of a differential transformer type. An internal Ag/AgCl/0.01 kmol·m^{-3} KCl reference electrode for measuring and controlling the potential of the specimen electrode, a counter electrode made of a small platinum plate (5mm x 5mm) and C-A thermocouple are also mounted in the autoclave. These three electrodes, namely, specimen, reference and counter electrodes are connected to a potentiostat in order to conduct the potentiostatic electrochemical measurements.

The electromotive force (EMF) of the reference electrode is converted to standard hydrogen electrode (SHE) scale at a given temperature as follows.

The EMF of Ag/AgCl electrode is given by the Nernst's equation :

$$E_{Ag/AgCl} = E^{\circ}_{Ag/AgCl} - (RT/F) \ln a_{Cl^-} \quad , \qquad (2\text{-}1)$$

where $E^{\circ}_{Ag/AgCl}$ is the standard potential of Ag/AgCl electrode, R the gas constant, F the Faraday constant, T the absolute temperature in K and a_{Cl^-} the activity of Cl^- ion. The temperature dependence of the standard potential of the Ag/AgCl electrode is given by the following equation reported by Greeley et al.[21],

$$E^{\circ}_{Ag/AgCl} = 0.23755 - 5.3783 \times 10^{-4} t - 2.3728 \times 10^{-6} t^2, \quad (2\text{-}2)$$

where t is the temperature in C.

The activity coefficient of Cl^- ion is also reported by Greeley et al.[22] for HCl. In the present work, the author used these data of activity coefficient for HCl. Recently, however, activity coefficients of Cl^- ion for KCl at elevated temperatures are reported by some authors[23],[24].

In the thesis, the electrode potential is expressed in the SHE scale.

The transient anodic current and the output of the straining transducer were recorded by the following digital equipments. Changes for the initial period of 1 s are recorded by a 2 channel digital memory scope at intervals of 1 ms. For the later period of about 50 s, only the change of anodic current was measured by a digital voltmeter at intervals of 0.083 s, the data measured by which are transferred to a micro computer via GP-IB interface. The data stored in the digital memory scope are also transferred to the micro computer via 8-bit parallel interface after the measurements are completed. The data processing was conducted automatically and instantaneously by the micro computer. An example of data displayed by the micro computer is presented in Fig.2-4. Figure 2-4(a) shows the changes in strain and current

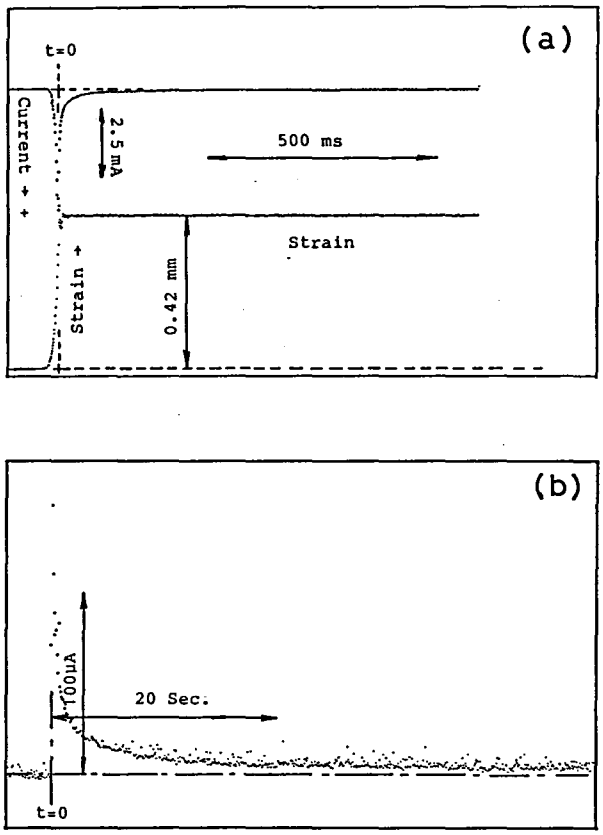

Fig.2-4 Example of the data displayed by a micro computer. (a)Changes in the current and strain measured by a 2-channel digital memory scope, (b)change in the current measured by a digital volt meter.

with time measured by the digital memory scope. Figure 2-4(b) shows the change in current density for about 50 s measured by the digital volt meter.

A schematic diagram of the change in anodic current and strain is presented in Fig.2-5. The current density on a newly created surface, i, is defined by the following equation[18] :

$$i(t) = (I(t) - I_r) / \Delta S$$
$$= \Delta I(t) / \Delta S \quad , \qquad (2\text{-}3)$$

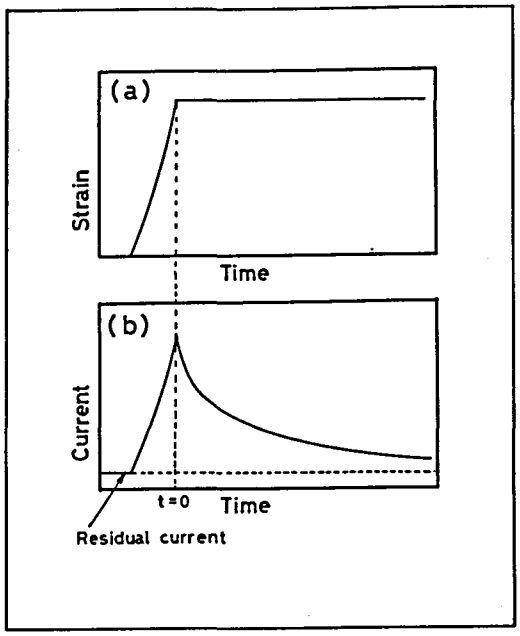

Fig.2-5 Schematic diagram of change in (a)strain and (b) anodic current.

where I(t) is the transient current at time t, I_r the residual current measured just before straining. Further, $\Delta I(t)$ is an increase of anodic current. ΔS is a small amount of increase of specimen surface, and is calculated by the next equation assuming that the wire specimen is elongated keeping its volume constant[18] :

$$\Delta S = (S_0 / 2)(\Delta l / l_0) , \qquad (2\text{-}4)$$

where l_0 is the initial length of the specimen(=30mm), S_0 the initially exposed area(=3.3×10^{-5} m^2) and Δl a small amount of elongation. Figure 2-6 is an example of computer display showing the change in current density with time.

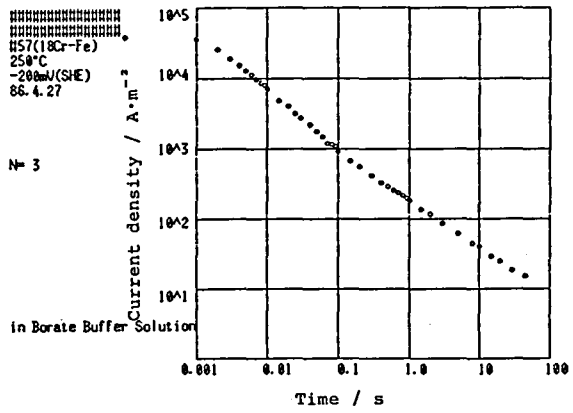

Fig.2-6 Example of computer display showing the change in the current density with time.

REFERENCES

(1)N. Ohtani : Bull. of Japan Inst. of Metals, 12 (1973), 233.

(2)R. M. Latanision and A. R. C. Westwood : "Advances in Corrosion Science and Technology", Plenum Press (1970), Vol.1, p.51.

(3)Osmand and Werth : Ann. Mines, 8 (1885), 1.

(4)H. Endo : Tetsu-to-Hagané, 14 (1928), No.4, 1.

(5)G. Tammann and C. Wilson : Z. anorg. Chem, 173 (1928), 156.

(6)M. T. Simnad and U. R. Evans : Trans. Faraday Soc., 46 (1950), 175.

(7)K. Nobe and Wm. F. Seyer : J. Appl. Phys., 29 (1958), 1632.

(8)M. T. Simnad and U. R. Evans : J. Iron Steel Inst., 156 (1947), 531.

(9)C. Wagner and W. Traud : Z. Elektrochem., 44 (1938), 391.

(10)A. G. Funk, J. C. Giddings, C. J. Christensen and H. Eyring : J. Phys. Chem., 61 (1957), 1179.

(11)A. G. Funk, D. N. Chakravati, H. Eyring, and C. J. Christensen : Physik. Chem., 15 (1958), 64.

(12)J. C. Giddings, A. G. Funk, C. J. Christensen and h. Eyring : J. Electrochem. Soc., 106 (1959), 91.

(13)K. F. Bonhoeffer : Z. Metallkunde, 44 (1953), 77.

(14)T. P. Hoar and J. M. West : Nature, 181 (1958), 835.

(15)S. Haruyama, S. Asawa and H. Nagasaki : Denki-Kagaku, 39 (1970), 564.

(16)A. R. Despic, R. G. Raicheff and J. O'M Bockris : J. Chem. Phys., 49 (1969), 926.

(17)J. R. Ambrose and J. Kruger : Corrosion, 28 (1972), 30.

(18)T. Shibata and R. W. Staehle : Proc. 5th Int. Cong. on Metall. Corros., 1972 , NACE (1974), p.145.

(19)F. P. Ford and M. Silverman : Corrosion, 36 (1980), 558.

(20)T. Murata : Tetsu-to-Hagane, 60 (1974), 116

(21)R. S. Greeley, W. T. Smith, Jr., R. W. Stoughton and M. H. Lietzke : J. Phys. Chem., 64 (1960), 652.

(22)R. S. Greeley, W. T. Smith, Jr., M. H. Lietzke and R. W. Stoughton : J. Phys. Chem., 64 (1960), 1445.

(23)H. F. Holmes and R. E. Mesmer : J. Phys. Chem., 87 (1983), 1242.

(24)W. F. Bogaerts and A. A. Van Haute : J. Electrochem. Soc., 131 (1984), 68.

CHAPTER III

Straining Electrode Behavior of Iron in High Temperature and High Pressure Sodium Sulphate Solution

3.1 Introduction

Extensive studies have been performed on the corrosion behavior of iron and carbon steels in high temperature alkaline solutions[1]-[6], in connection with power steam generators. Potter and Mann[6] reported the formation of porous double magnetite layers on the carbon steel in this environment.

Many studies have been conducted over the past decade on SCC of stainless steels in high temperature and high pressure neutral water[7]. Various conditions to assist SCC, such as potential, temperature and other environmental and metallurgical factors have been revealed in recent years. Moreover, considerable attentions have been denoted to magnetite deposition on a carbon steel used as a tube support plate in a steam generator of pressurized water reactor, relating to the denting phenomena[8]-[11]. In order to understand the corrosion and film formation behavior as well as the basic mechanism of SCC propagation for iron-base alloys, it is important to know the initial anodic behavior on a newly created surface.

In this chapter, the rapid straining electrode technique is introduced to study a transient anodic process on a newly created surface of iron at temperatures up to 573 K in a neutral Na_2SO_4 solution.

3.2 Experimental

The material used was electrolytic iron, whose chemical composition was as follows : 0.0013 O, 0.0007 N, 0.006 C, 0.0015 Si, 0.001 Al, 0.006 S and 0.005 Mn (mass%), and balance Fe. The material was remelted, cast in a vacuum and drawn to thin wire of 0.35 mm diameter. The wire specimen was degreased with acetone in an ultrasonic bath, annealed in a vacuum at 1073 K for 900 s, then water quenched. The specimen surface was neither polished nor given any further treatments.

The electrolyte used was 0.1 $kmol \cdot m^{-3} Na_2SO_4$ prepared with distilled water and reagent grade chemicals.

The testing apparatus was already described in Chapter II. The experimental procedures were as follows. After a specimen was mounted and the autoclave was closed, the solution was deaerated by purified N_2 gas. Then the autoclave was heated to a test temperature with a heating rate of about 0.15 $K \cdot s^{-1}$. Soon after the temperature was attained, the specimen was cathodically polarized to a potential about 100 mV less noble than the open circuit potential ($E_{Corr.}$) for about 600 s, and then anodic polarization curve was measured. In the straining electrode test, the specimen potential was shifted rapidly to a test potential after 600 s application of the cathodic polarization, and was kept at the same potential for about 3.6 ks in order to obtain a steady state of the specimen surface. The straining electrode test was conducted 5 ∿ 10 times at the same test potential for one specimen until it failed.

3.3 Results

3.3.1 Polarization curves

Anodic polarization curves of iron in 0.1 kmol·m^{-3} Na_2SO_4 at various temperatures are shown in Fig.3-1. The curves exhibit the presence of the passive state in a range from about -0.2 V to +0.5 V at 473 ∿ 553 K. The iron specimen, however, dissolved away without showing any passive state at 423, 433 and 453 K.

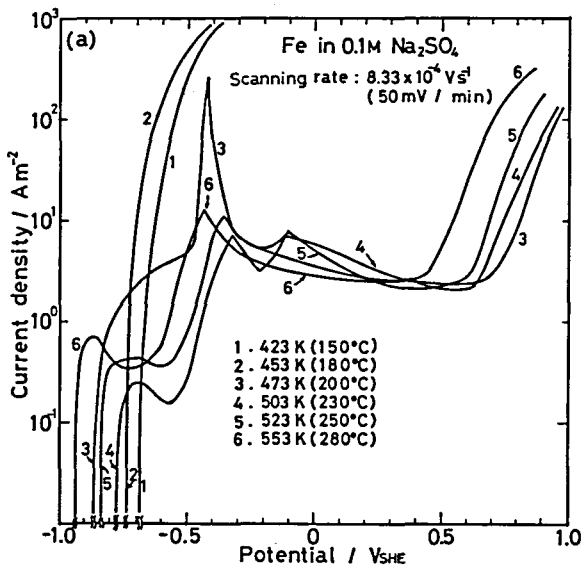

Fig.3-1 Anodic polarization curves of iron in 0.1 kmol·m^{-3} Na_2SO_4.

3.3.2 Straining electrode behavior

Typical changes in the transient current densities with time are shown in Fig.3-2 for a few sets of conditions. Two distinct regions in the current decay with time were observed after the elongation was stopped. The current decay followed a power law, except for the initial region of about 0.1 ∿ 0.2 s :

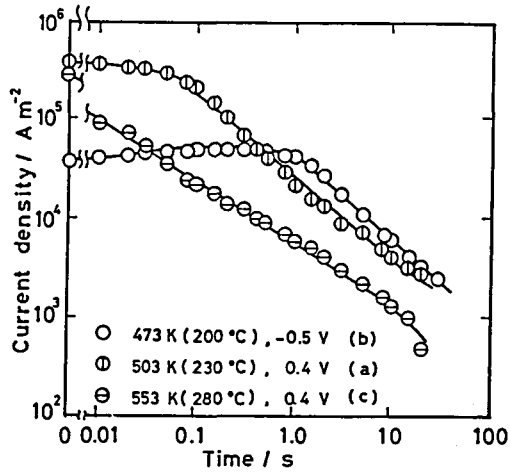

Fig.3-2 Typical changes in the anodic current density with time under a few conditions.

$$i = at^{-n} \qquad (3\text{-}1)$$

with n in the range of 0.6 ∿ 0.9. The current density increased slightly up to 0.1 ∿ 0.2 s and thereafter decayed with the power law at low temperature and at less noble potential (Fig.3-2(b)). To the contrary, the period of initial region was shorter than about 20 ms at higher temperature and at more noble potential, and then the current decayed with the power law (Fig.3-2(c)). The power n varied with potential and temperature. The value of n is a criterion of the repassivation ability, because the larger n means the higher repassivation rate. The length of the initial region also depends on the repassivation ability. Thus, this ability should be discussed in terms of n and the initial period.

As stated before, the measurements of straining electrode behavior were repeated for 5 ∿ 10 times at a fixed potential and temperature for one specimen. Examples of changes in transient

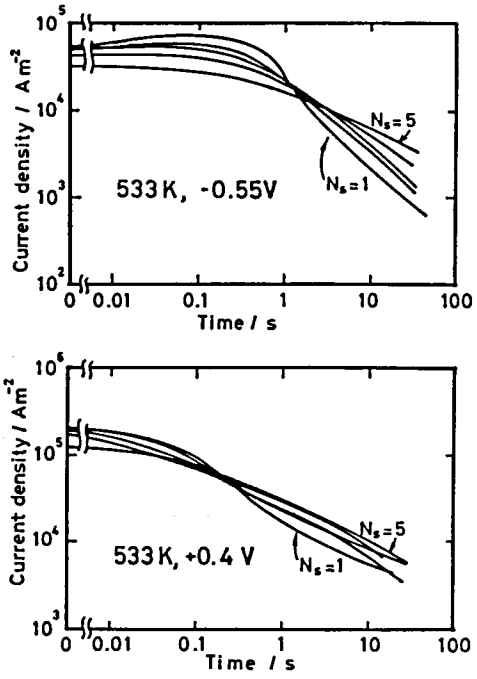

Fig.3-3 Changes in the transient current with the number of straining.

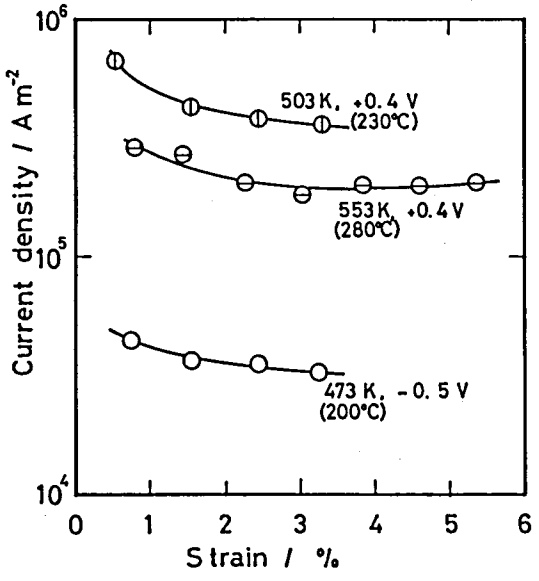

Fig.3-4 Changes in the initial currenst, i_0, with the total amount of strain under a few conditions.

current density with the number of straining, N_s, are shown in Fig.3-3. It is clearly seen that the current density immediately after the straining was stopped (t=0) decreased with increasing N_s, and that the slope of log i vs log t plot also changed with N_s. Figure 3-4 shows the change in the current density immediately after the elongation was stopped, i_0, with increasing total amount of strain for several conditions. i_0 decreased with the increase in the total amount of strain. The decrease in i_0 was particularly remarkable for the strain between about 0.8 and 1.6 %. Therefore, the current density obtained at the second straining, corresponding to the total strain of about 1.6 %, was used for the following analysis.

The measurements of straining electrode behavior were conducted mainly at 503 and 533 K. The decay curves followed the power law from 0.01 to 0.03 s with n being about 0.54 at

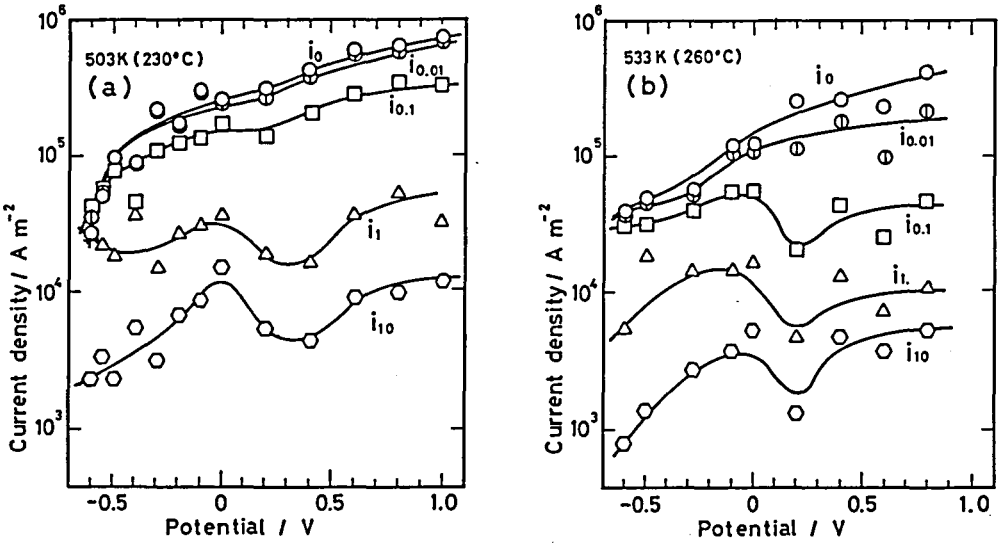

Fig.3-5 Potential dependence of the initial current density, i_0, and the transient anodic current density at 0.01, 0.1, 1 and 10 s after elongation is stopped, as indicated by subscripts, at (a)503 K and (b)533 K.

potentials above -0.1 V. On the other hand, the curves followed the power law from 0.1 ∿ 0.2 s at passive potentials of -0.6, -0.5 and -0.28 V, and the value of n ranged from 0.6 to 0.9. The period of initial region at 503 K was, as a whole, longer than that at 533 K, with n being 0.75 0.9 at the passive potential region.

Figures 3-5(a) and (b) show the potential dependence of current density at 0, 0.01, 0.1, 1 and 10 s after the elongation was stopped. The initial current i_0 increases slightly with increasing potential. The distance between each curve is proportional to the repassivation rate. The wider distance means the faster repassivation. i_1 and i_{10} show minimum at about 0.3 V for 503 K and at about 0.2 V for 533 K. This fact means that the repassivation is rapid at these potentials, which just corresponds to the minimum passive current shown in polarization curves in Fig.3-1. However, curves of i_0, $i_{0.01}$, and $i_{0.1}$ cross

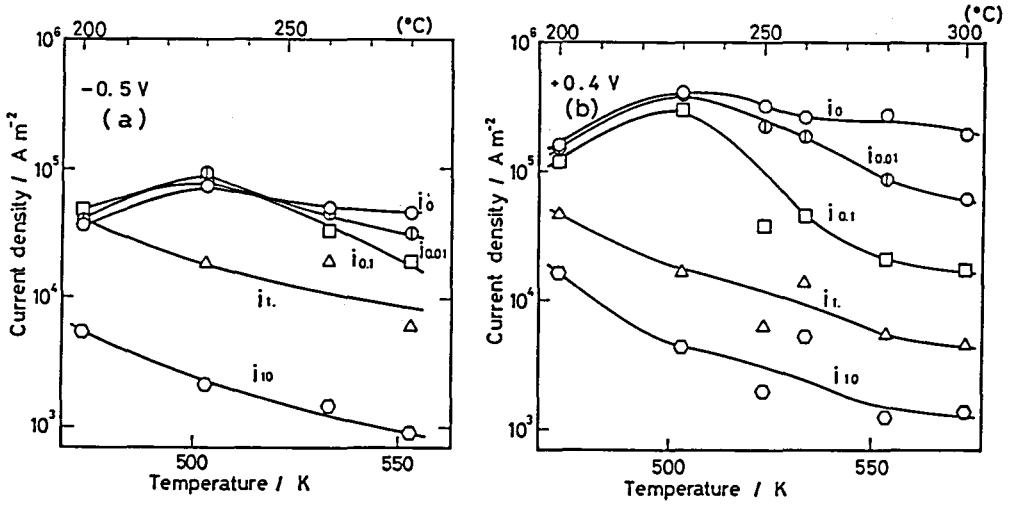

Fig.3-6 Temperature dependence of the transient anodic current density at (a)-0.5 V and (b)+0.4 V.

each other at the less noble potential region at 503 K. This fact means that the current density increased for a while after the elongation was stopped, as mentioned above.

Figures 3-6(a) and (b) show the temperature dependence of current density at the active potential of -0.5 V and at the passive potential of 0.4 V, respsectively. i_0 as well as $i_{0.01}$ and $i_{0.1}$ show a maximum at 503 K both at -0.5 and 0.4 V. This figure also shows that i_1 and i_{10} decrease with increasing temperature at both of the active and the passive potentials. The current density after 10 s still decreased, but its change was not so large, while the back current noise was relatively large. Thus, the value of i_{10} was used to represent the steady current density, because it could be definitely determined after being separated from the back current noise.

3.4 Discussion

3.4.1 Transition temperature for no passivation

Figure 3-7 shows schematically that the initial current on the newly created surface has a maximum at 503 K, and the steady state current decreases with increasing temperature, as mentioned before. If these curves were extrapolated to lower temperatures, they would cross each other. For this case, the higher steady state current can be expected compared with the initial dissolution current. Thus, no passivation does occur at the lower temperatures. This transition for no passivation is likely to occur at around 460 K. In fact, no passivation was observed for anodic polarization curves and for the straining electrode test at 423 $\sim$ 463 K.

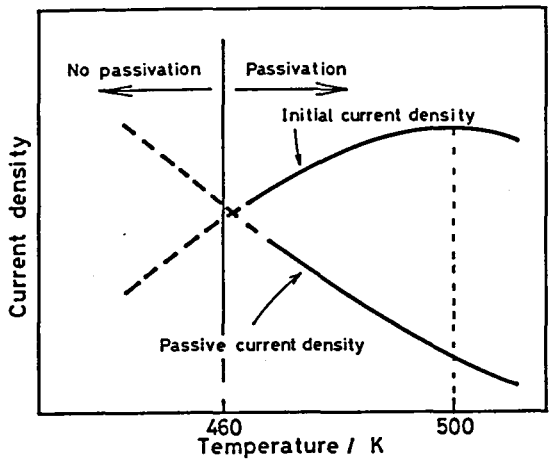

Fig.3-7 Schematic diagram of the current density on the newly created surface and the passive current density.

3.4.2 Active dissolution process

The current density on the newly created surface showed a slight increase even after straining was stopped at less noble potentials and at low temperatures, as shown in Fig.3-2. The increase in the current density after straining was stopped did not occur owing to a rapid film formation at noble potentials and at high temperatures. The changes in i with t, however, did not follow Eq.(3-1) and showed slower repassivation rate than that expected from the equation, in the initial period. Not only film formation but also active dissolution was supposed to occur in the initial period of repassivation.

Referring to the mechanism of active dissolution for iron at room temperature[12),(13)], the next reaction occurs on the newly created surface :

$$\text{Step A} : Fe + OH^- \rightarrow (FeOH)_{ads} + e^- \quad (3\text{-}2)$$

$$\text{Step B} : (FeOH)_{ads} \rightarrow (FeOH)^+ + e^- \quad (3\text{-}3)$$

$$\text{Step C} : (FeOH)^+ \rightarrow Fe^{2+} + OH^- \ . \quad (3\text{-}4)$$

OH^- ions in the solution near the bare surface are consumed instantaneously after the bare surface emerges, in the reaction of step A. Thus, the concentration of H^+ ion adjacent to the bare surface increases, namely, pH decreases locally as a result of dissociation of H_2O. $(FeOH)^+$ is also formed as an intermediate product of the series of reactions. Then, excess H^+ thus formed diffuses gradually into bulk solution, resulting in pH restoration which promotes the reaction of the step A. Thereafter, the anodic current increases with time. When dissolved $(FeOH)^+$ or Fe^{2+} exceeds its solubility, oxide or hydroxide deposits on the bare surface, namely, the film formation, resulting in the anodic current decreasing with time.

3.4.3 Strain dependence of active dissolution period

As shown in Figs.3-3 and 3-4, i_0 decreased with the increase in the total amount of strain. This fact seems to be brought about by a change in morphology of slip step of exposed metal surface.

The area of bare surface created by emergence of the slip step is proportional to the amount of given elongation, Δl, as defined by Eq.(2-4). The area actually must be corrected

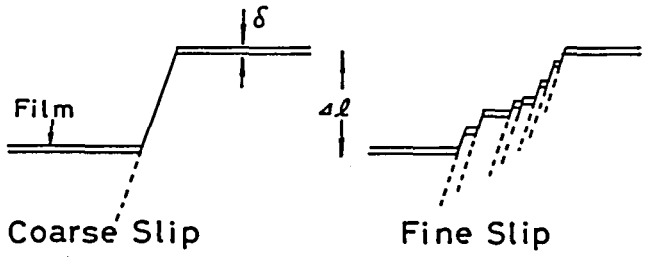

Fig.3-8 Schematic sketch of two kinds of slip stepes. The coarse slip gives a larger effective area than the fine slips.

considering the thickness of film, δ , and the number of slip steps, N, included in the given elongation of Δl, as illustrated in Fig.3-8, which indicates two types of slip steps. Consequently, the effective area, ΔS_e, is expressed by the following equation[14] :

$$\Delta S_e \propto \Delta l - N \delta \quad . \tag{3-5}$$

This relation suggests that the fine slip steps, namely a larger number of slip steps, create a less effective area. It is supposed that the dislocation density increases with increasing strain. Dislocations in iron are known to form a tangled or cell wall structure which may create fine steps. Therefore, the more total strain creates the less effective area of newly created surface. Consequently, the apparent initial current density decreases with the increase in the total strain.

3.4.4 Film formation behavior

The transient anodic current on the newly created surface must be discussed in terms of the film formation which is directly connected to the accumulated charge.

Figure 3-9 shows the change in the total amount of charge with time. The charge, Q, is calculated by numerical integration of the i vs t curve. The curves of log Q vs log t show nearly straight lines with the slope of almost unity in the initial region at the active potential (Fig.3-9(a)). The slope gradually decreases with time in the later region. These facts indicate that the anodic current in the initial region was consumed mostly by the active dissolution, while a slight suppression of anodic current occurred in the later region due to

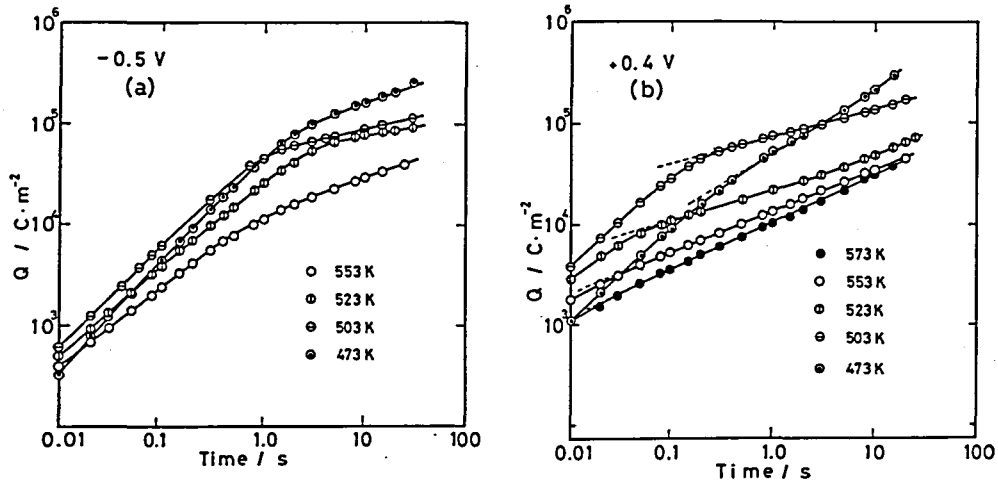

Fig.3-9 Changes in the total amount of charge, Q, with time at several temperatures at (a)-0.5 V and at (b)+0.4 V.

the formation of corrosion products. The curves in the initial region also show nearly straight lines with the slope being less than unity such as 0.54 ∿ 0.9 at the passive potential (Fig.3-9(b)). That is, the active dissolution was already suppressed by the film formation even in the initial region. The film formation becomes more rapid with increasing temperature, because the slopes of curves decrease with increasing temperature. After 0.03 ∿ 0.25 s passed, the slopes change to smaller values as can be seen in Fig.3-9(b).

Since the anodic current decay follows the power law, the amount of charge, Q, is derived from the following integration of Eq.(3-1) :

$$Q = \int_0^t i\,dt = \int_0^t at^{-n}dt$$

$$=(a(1-n))t^{1-n} + C, \qquad (3\text{-}6)$$

$$Q - C = (a/(1 - n))t^{1-n} \quad (3\text{-}7)$$

$$= (a/(1 - n))(i/a)^{(1-n)/-n} . \quad (3\text{-}8)$$

Accordingly, the current density is expressed as a function of Q :

$$i = k / (Q - C)^{m} , \quad (3\text{-}9)$$

where, k and C are constants, and m=n/(1-n). The value of C is proportional to the charge passed during the initial region, that is, the dissolution charge, $Q_{d,i}$. Thus, Eq.(3-9) is modified to

$$i = k / (Q - Q_{d,i})^{m} . \quad (3\text{-}10)$$

The relation between log i and log $(Q - Q_{d,i})$ is shown in Fig.3-10. The value of $Q_{d,i}$ is determined so as to fit the experimental data to Eq.(3-10), and is shown in Fig.3-11. It is important to note that the slopes of all curves for 503, 523, 553

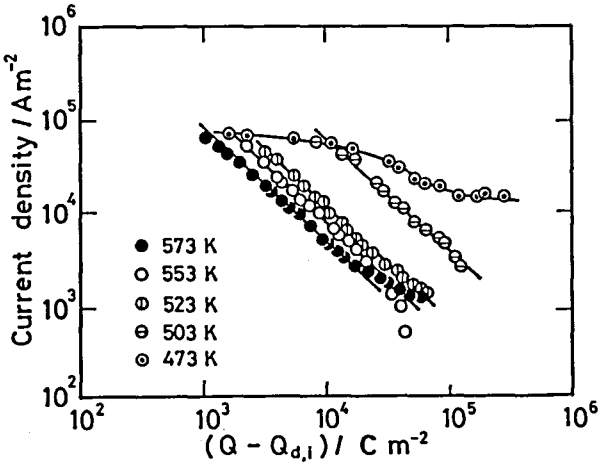

Fig.3-10 Current density, i , vs the amount of charge, $(Q - Q_{d,i})$, in log - log scale at several temperatures at 0.4 V.

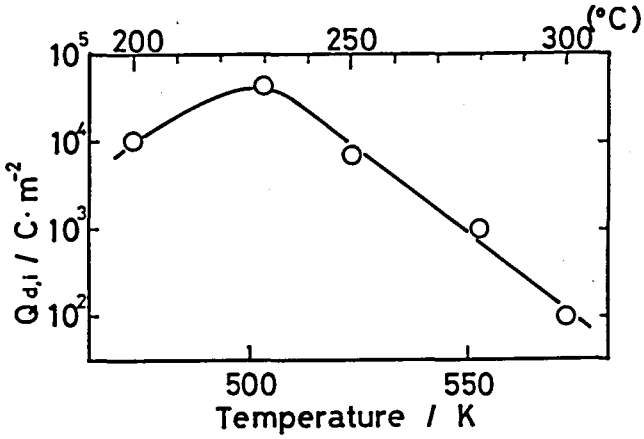

Fig.3-11 Temperature dependence of the initial dissolution charge, $Q_{d,i}$.

and 573K are all nearly -1. This means m=1 for Eq.(3-10). Consequently, the exact relation can be expressed as the following Eq.(3-11) :

$$i = k / (Q - Q_{d,i}) . \qquad (3\text{-}11)$$

This equation is known as the parabolic rate law of film growth. It should be emphasized that the reaction constant, k, decreased with increasing temperature, the value of k being determined from the intercept in Fig.3-9. The parabolic law suggests that the film growth is determined by the diffusion of reaction species through the film. Thus, k includes the diffusion constant D. Assuming that the amount of charge accumulating as the film is a part of the total charge and that the ratio of $\alpha = Q_{film}/Q_{total}$ is constant, the following equation is obtained :

$$Q_{film} = \alpha (Q - Q_{d,i}). \qquad (3\text{-}12)$$

Then, Eq.(3-11) is expressed by

$$i = k'D / \alpha \ (Q - Q_{d,i}) \ . \qquad (3\text{-}13)$$

The iron oxide formed in the high temperature water is known to be magnetite, which is formed by the following Shikkor's reaction[15],

$$3Fe^{2+} + 4H_2O \longrightarrow Fe_3O_4 + 6H^+ + H_2 \ . \qquad (3\text{-}14)$$

The oxide film is formed at the oxide/solution interface by deposition of Fe_3O_4 from Fe^{2+} ion, which is produced by anodic dissolution[16],[17]. The solubility of magnetite in a neutral high temperature water decreases with increasing temperature[18],[19]. The lower solubility means to make Fe^{2+} ion precipitate more easily. Then, the ratio of α included in k increases with increasing temperature. Therefore, the negative temperature dependence of k is supposed to be caused by the difference between temperature dependence of both D and α. The activation energy for the diffusion of iron in magnetite is, however, known to be about 190 $kJ \cdot mol^{-1}$[20]. On the other hand, the change in the free energy for the solubility of magnetite is calculated[19] to be merely -19 $kJ \cdot mol^{-1}$. Therefore, the observed negative temperature dependence of k could not be expected to be caused only by the difference between these energies. This fact suggests that the rate constant k includes another parameter with the temperature dependence being more negative than that of D/α. Such a parameter is supposed to be the porosity or the number of the site of diffusion path in the oxide film[16]. A more compact film contains fewer porosity or

fewer diffusion paths. Thus, higher temperature might accelerate the formation of the more compact film. Consequently, the negative temperature dependence of k could be explained more rationally by assuming the above parameters of D, α , and the shape of porosity and/or diffusion paths included in the oxide film.

The film formation kinetics, however, could not be analyzed definitely for all temperatures at the active potentials, in the present work. It is most probable that a less protective film is formed under these conditions.

3.4.5 Strain dependence of repassivation rate

The repassivation observed in the straining electrode technique occurs on the slip step which is surrounded by a pre-formed oxide layer as already stated. Therefore, the surface film has a heterogeneous structure with many defects, because the specimen surface is covered with a mixture of pre-formed thick passive film and newly-formed thin film. The heterogeneity of surface film increases with increasing the number of straining. Thus, the number of defects in the oxide layer also increases. The repassivation rate is determined by diffusion of Fe^{2+} ions through defects in the film as discussed in section 3.4.4. The increase in the number of diffusion path would increase the dissolution current. Thus, the repassivation was slowed with the increase in the total amount of strain. Moreover, a localized dissolution tends to occur after many times of straining electrode tests, resulting in failure of the specimen.

3.4.6 Consideration of SCC

When SCC proceeds by an active path corrosion (APC) mechanism, a crack propagates more readily under such a condition that dissolution on the side wall of the crack is suppressed and active dissolution at the crack tip is fast, thus self-sustaining dissolution being continued. In the present experiment, the repassivation rate in the power law region showed a maximum in the passive potential region at 0.3 V for 503 K and at 0.2 V for 533 K, as shown in Fig.3-5, and the active dissolution in the initial stage showed the maximum rate at 503 K, as shown in Fig.3-10. These facts suggest that a favorable situation to assist SCC of iron in 0.1 kmol·m^{-3} Na_2SO_4 could be attained under the condition of 503 K and 0.3 V. In fact, it is reported that carbon steels suffer with SCC under conditions similar to those discussed above[21),(22)].

3.5. Conclusions

Using the rapid straining electrode technique, the initial process of anodic behavior on the newly created surface of iron was investigated in 0.1 kmol·m^{-3} Na_2SO_4 at temperatures up to 573K.

(1) Two regions were observed for the change in the transient anodic current with time. The current density decayed following a power law ; $i = at^{-n}$ with n in a range of 0.5 ∿ 0.9, except for the initial region.

(2) The initial current, i_0, increased slightly with increasing potential and showed a maximum at 503 K. The steady current on the passivated surface decreased with increasing temperature.

(3) At 503 ∿ 573 K and at the passive potential, the passive

film grew following a parabolic growth law : $i=k/Q$, but the reaction constant k showed a negative temperature dependence.

(4) Iron did not show any passive state, in a temperature range 423 $\sim$ 463 K.

(5) A favorable condition to assist SCC of iron in this environment could be attained under the condition of 503 K and 0.3 V.

REFERENCES

(1)M. C. Bloom and M. Krulfield : J. Electrochem. Soc., 104 (1957), 264.

(2)D. L. Douglass and F. C. Zyzes : Corrosion, 13 (1957), 433.

(3)O. Asai and N. Kawashima : DENKI-KAGAKU, 33 (1965), 444.

(4)T. Mukaibo and S. Masukawa : DENKI-KAGAKU, 33 (1965), 576.

(5)J. E. Castle and H. G. Masterson : Corros. Sci., 6 (1966), 93.

(6)E. C. Potter and G. M. W. Mann : Proc. 1st Int. Cong. on Metallic Corros., London, (1961), p.417.

(7)Z. Szklarska-Smialowska and G. Cragnolino : Corrosion, 36 (1980), 653.

(8)R.Gransey : Nucl. Energy, 18 (1979), 117.

(9)G. E. von Nieda, G. Economy and M. J. Wootten : Mater. Performance, 20 (1981), 38.

(10)S. J. Green and J. P. N. Paine : Nucl. Technology, 55 (1981), 10.

(11)J. R. Park and D. D. MacDonald : Corros. Sci., 23 (1983), 295.

(12)N. Sato, G. Okamoto : Bull. Japan Inst. Metals, 5 (1966), 590.

(13)J. O'M. Bockris, D. Drazic and A. R. Despic : Electrochim. Acta, 4 (1961), 325.

(14)T. Shibata and R. W. Staehle : Proc. 5th Int. Cong. on Metallic Corros., USA (1975), p.487.

(15)G. Schikkor : Z. anorg. allagem. Chem., 212 (1933), 33.

(16)G. J. Bignold, R. Gransey and G. M. W. Mann : Corros. Sci., 12 (1972), 325.

(17)L. Tomlinson : Corrosion, 37 (1981), 591.

(18)F. J. Shipko and D. L. Douglass : J. Chem. Phys., 60 (1956), 1519.

(19)F. H. Sweeton and C. F. Baes, Jr. : J. Chem. Thermodynamics, 2 (1970), 479.

(20)M. H. Davies, M. T. Simnad and C. E. Birchenall : Trans. AIME, 191 (1951), 889, (J. Metals).

(21)F. Umemura and T. Kawamoto : Boshoku Gijutsu, 30 (1981), 276.

(22)H. Choi, F. H. Beck, Z. Szklarska-Smialowska and D. D. MacDonald : Corrosion, 38 (1982), 136.

CHAPTER IV

Straining Electrode Behavior of Nickel in High Temperature and High Pressure Aqueous Solution Containing Sulphate Ion

4.1 Introduction

Nickel base alloys are used as corrosion resistant materials in high temperature and high pressure water environments which are commonly comprised in both BWR and PWR. It has been reported that Alloy 600 seriously suffers with localized attacks such as IGSCC and IGA. The electrochemical dissolution, film formation and its breakdown are supposed to play an important role to cause the above failures. However, there have been few studies to examine the basic electrochemical process of nickel or high nickel alloys[1] in the high temperature and high pressure water environment because of the experimental difficulty.

This chapter deals with the very initial anodic behavior on the newly created surface of nickel in high temperature and high pressure aqueous solutions containing sulphate ions. The film formation and its breakdown were mainly discussed with the emphasis on an aggressive action of sulphate ion.

4.2 Experimental

The specimen was commercial nickel wire (0.35 mm diameter), whose chemical composition was : 0.028 C, 0.0032 P, 0.0037 S, 0.06 Si, 0.38 Mn, 0.29 Co, 0.09 Fe, 0.007 Cu, 0.001 Cr (mass%), and balance Ni. The wire was degreased, then annealed in a vacuum at 1073 K for 900 s followed by water quench. Solutions used in the present experiment were 0.1 kmol·m^{-2} Na_2SO_4, a borate

buffer solution, i.e., 0.15 kmol·m^{-3} H_3BO_3 + 0.0375 kmol·m^{-3} $Na_2B_4O_7$ and borate buffer solutions with additions of Na_2SO_4 of some concentrations. These solutions were prepared with reagent grade chemicals and distilled water.

The straining electrode tests were conducted at a series of constant potentials over a wide potential range from the active to passive at intervals of 100 mV. When one elongation was given, the change of anodic current was recorded for about 1 min. The specimen potential was switched to a noble potential soon after the measurement of anodic current was completed and kept for a few tens minutes to reach a steady state, and then the next straining was given.

The strain for one elongation was about 1.5 % with a strain rate of about 0.25 s^{-1}.

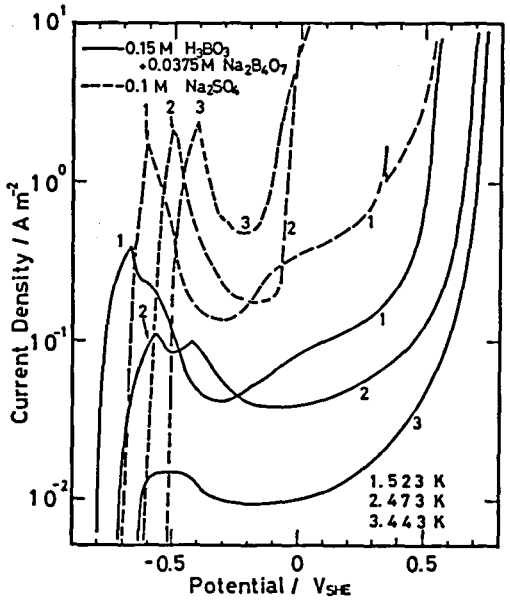

Fig.4-1 Anodic polarization curves of nickel in a borate buffer solution and a sodium sulphate solution.

4.3 Results

4.3.1 Polarization curves

The polarization curves measured in 0.1 $kmol \cdot m^{-3} Na_2SO_4$ and the borate buffer solution at various temperatures are shown in Fig.4-1. The polarization curves in the borate buffer solution show a wide and steady passive region. The current density in the sodium sulphate solution is more than five times as large as that in the borate buffer solution to the contrary. In addition, it should be noted that the current density increases abruptly at a critical potential before the potential reaches to the oxygen evolution region. These facts suggest that the passivity of nickel in the sodium sulphate solution is unstable in contrast with that in the borate buffer solution.

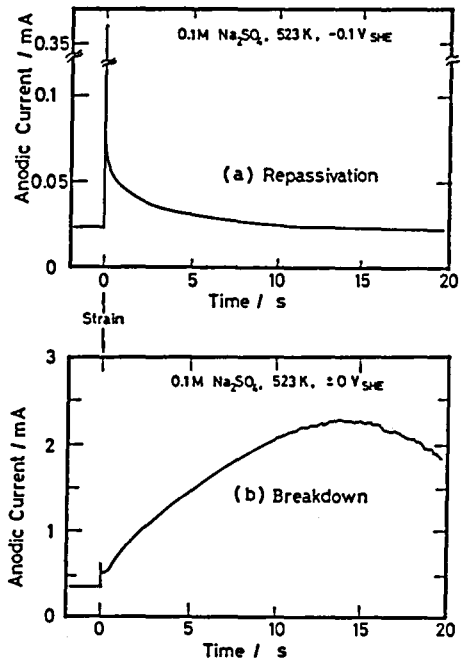

Fig.4-2 Typical changes in the anodic current with time on the newly created surface showing (a) repassivation and (b) breakdown.

4.3.2 Straining electrode behavior

Two types of changes in the anodic current were found for the surface newly created in the 0.1 kmol·m^{-3} Na_2SO_4 solution, as shown in Fig.4-2. The first type shows a rapid decay after the elongation was stopped. This behavior is, therefore, called the repassivation type (Fig.4-2(a)). In the second type, the anodic current shows no rapid decay and sometimes increases gradually, depending on the applied potential and temperature (Fig.4-2(b)). The second is called the breakdown type, because the passive film breaks down locally as will be described later. The regions of the repassivation and the breakdown are illustrated in Fig.4-3 as a function of temperature and potential. The repassivation was observed at less noble potentials. The breakdown was observed at potentials more noble

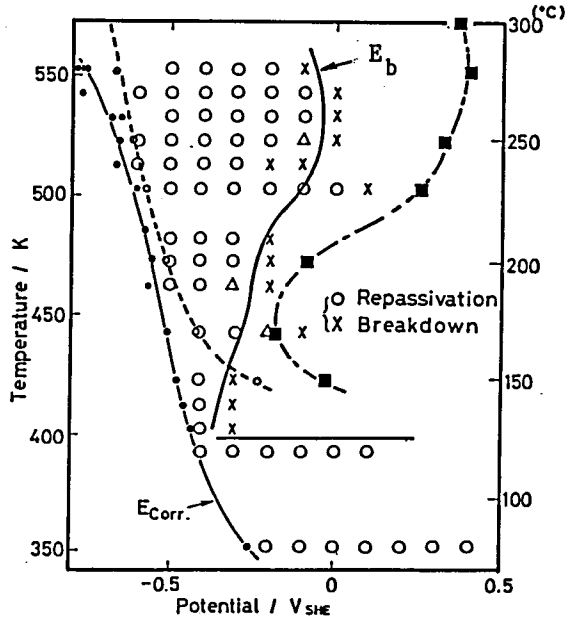

Fig.4-3 Potential-temperature diagram showing regions of repassivation and breakdown. The area between broken line and the dash-dotted line is the passive region obtained from polarization curves shown in Fig.4-4.

than a critical potential, which is called the breakdown potential, E_b, shown as a solid line in this figure. The region between the breakdown potential and the corrosion potential, $E_{Corr.}$, is called the repassivation region. The symbol Δ indicates the intermediate case where the repassivation or the breakdown could not be precisely determined. The repassivation region becomes wider with the increase in temperature above 403 K. The breakdown, however, did not occur at any potential and any temperature tested below 393 K. The broken line in Fig.4-3 shows the peak current potentials, E_p, found in the polarization curves measured in the same solution, shown in Fig.4-4. The dash-dotted line shows the critical potentials, E_c, at which the current density increased again as the potential increased. Thus, the area between these two lines indicates the passive region exhibited by the polarization

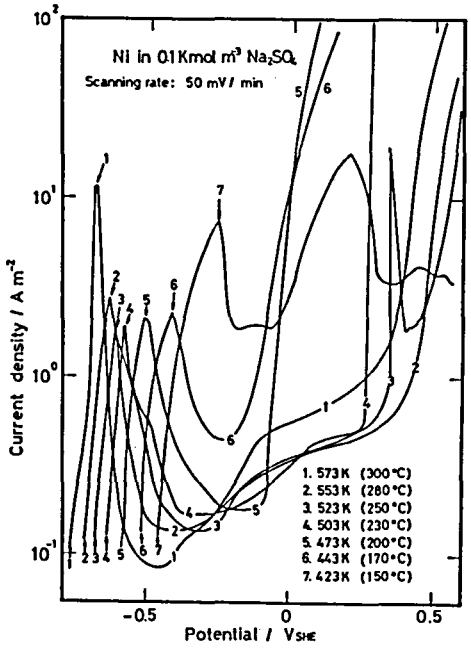

Fig.4-4 Anodic polarization curves of nickel in 0.1 kmol·m^{-3} Na_2SO_4 for a temperature range from 423 to 573 K.

curves. It is noticed that the passive region found in the polarization curves becomes wider with the increase in temperature, as does the repassivation region determined by the straining electrode.

The straining electrode test in the borate buffer solution showed no breakdown at any temperature and any potential tested. This corresponds to the fact that the polarization behavior in the borate buffer solution clearly differs from that in the sodium sulphate solution. Therefore, the presence of sulphate is supposed to be harmful to the passivity of nickel. In order to examine the effect of sulphate ion more precisely, the breakdown potential in borate buffer solutions with additions of 0.001, 0.01, 0.05, 0.1 and 0.3 kmol·m^{-3} Na_2SO_4 was measured at various temperatures. Figure 4-5 shows the potential-temperature diagram

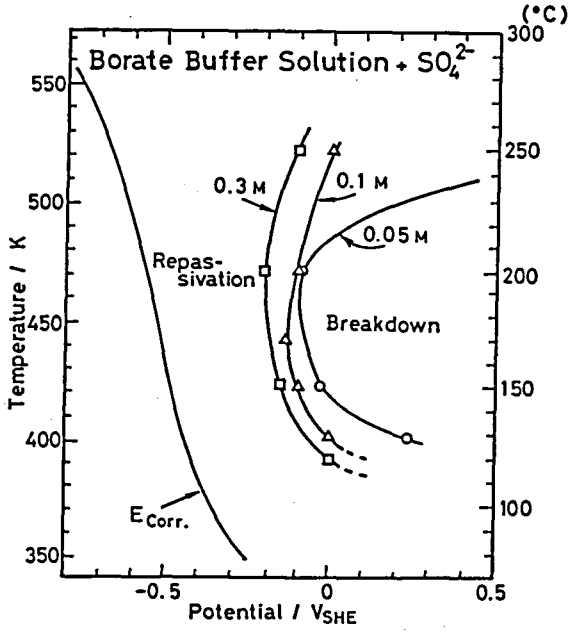

Fig.4-5 Potential-temperature diagram showing the breakdown potential for various sulphate ion concentrations.

of the repassivation/breakdown region. The breakdown potential shifts to less noble direction with increasing concentration of sulphate ion. The breakdown was, however, not observed in the solutions of 0.001 and 0.01 $kmol \cdot m^{-3}$ SO_4^{2-}.

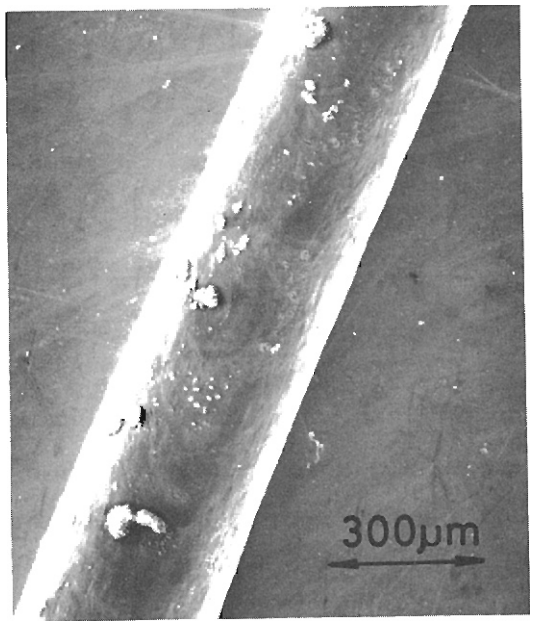

Fig.4-6 SEM morphology of the specimen showing breakdown (523 K, +0.4 V).

4.3.3 SEM observation of specimen surface

A surface morphology of the breakdown specimen was examined with a SEM, which is shown in Fig.4-6. The majority of the surface suffered with no attack, but a small amount of debris was distinctly visible. The debris was yellowish green and identified to be $Ni(OH)_2$ by a powder X-ray diffraction method. On the other hand, the surface of the specimen which showed no breakdown (i.e., repassivation), exhibited no localized corrosion and no debris. Thus, an active dissolution at this pit-like localized corrosion brought about the active dissolution with a large anodic current resulting in the formation of debris.

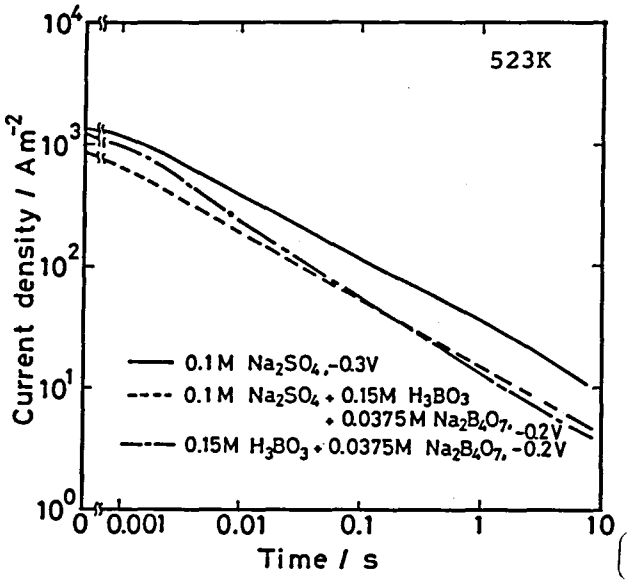

Fig.4-7 Typical changes in the anodic current density on the newly created surface at 523 K under various conditions.

4.3.4 Film formation behavior

During the repassivation, several types of the transient current were found, depending on the composition of solution examined. The transient current followed the power law as shown in Fig.4-7.

$$i = at^{-n} . \qquad (4\text{-}1)$$

The current density immediately after the elongation was stopped, i_0, showed no distinguishable dependence on the applied potential and the solution composition. On the other hand, the repassivation behavior, observed in the change in anodic current with time, was dependent on the applied potential as well as on the concentration of SO_4^{2-} ion. The value of n in Eq.(4-1) was in the range of 0.5 ∿ 0.8 in the borate buffer solution and was approximately 0.5 in 0.1 kmol·m^{-3}Na_2SO_4. The larger n means

the higher repassivation rate. Consequently, it is concluded that . the repassivation rate in the borate buffer solution is higher than that in the sulphate solution.

The repassivation behavior in the borate buffer solution will be discussed in detail in Chapter VI.

4.4 Discussion

4.4.1 Breakdown of passivity of nickel due to SO_4^{2-} ion

Two distinct anodic processes on the bare surface of nickel are possible to occur, at the transition from active to passive state, as described by Sato et al.[2]: the direct film formation and the dissolution-precipitation. The direct film formation (Process A) is the reaction of metal surface with solution to form a compact oxide film, described as follows :

$$\text{Process A} : \quad Ni + H_2O \rightarrow NiO + 2H^+ + 2e^- \quad . \qquad (4\text{-}2)$$

The dissolution-precipitaion (Process B) is a two or three-step process in which dissolved ion precipitates to form an oxide film on the nickel surface :

$$\text{Process B} : \quad Ni \rightarrow Ni^{2+} + 2e^- \qquad (4\text{-}3)$$

$$Ni^{2+} + H_2O \rightarrow (NiOH)^+ + H^+ \qquad (4\text{-}4)$$

$$(NiOH)^+ \rightarrow NiO + H^+ \quad . \qquad (4\text{-}5)$$

If sulphate ion is included in the solution, a preferential adsorption of it will occur simultaneously, and then, a salt forms instead of Eq.(4-4). A further hydrolysis of the salt leads to the formation of a hydroxide by Process C :

Process C : $Ni \rightarrow Ni^{2+} + 2e^{-}$ (4-3)

$Ni^{2+} + SO_4^{2-} \rightarrow Ni^{2+} \cdot SO_4^{2-}$ (4-6)

$Ni^{2+} \cdot SO_4^{2-} + H_2O \rightarrow Ni(OH)_2 + 2H^{+} + SO_4^{2-}$ (4-7)

Nickel oxide, NiO, formed by Process A is supposed to be compact and protective, because NiO is formed directly on metal surface without the dissolution-precipitation process. On the other hand, the oxide formed by Process B is less protective than that formed by Process A. The hydroxide formed by Process C is, however, highly porous as demonstrated in Fig.4-6 and is permeable to ions. If SO_4^{2-} ion is contained in the solution, Process C occurs in parallel with Process A and/or B, and then the repassivation is slowed.

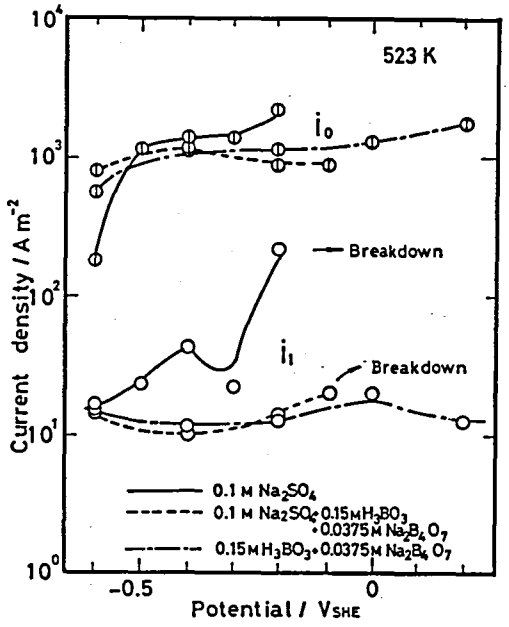

Fig.4-8 Potential dependence of i_0 and i_1, the current density 0 s and 1 s after elongation was stopped in various test solutions.

The effects of SO_4^{2-} and potential on the repassivation rate are more clearly seen in Fig.4-8, in which i_0 and i_1, the current density at 1 s after elongation was stopped, are plotted against the applied potential in three kinds of the solutions : 0.1 kmol·m^{-3} Na_2SO_4, the borate buffer solution, and the borate buffer solution + 0.1 kmol·m^{-3} Na_2SO_4. i_0 shows no distinguishable difference each other in these three solutions. The current density i_1 is independent of the applied potential in the borate buffer solution, but it increases with the potential in the solutions containing SO_4^{2-}. High concentration of sulphate ion and a high electrode potential are considered to accelerate the adsorption of sulphate ion. When the adsorption of SO_4^{2-} exceeds a critical amount, Process C is facilitated. The higher current accelerates the accumulation of SO_4^{2-}, which in turn promotes Process C. Thus, the self-acceleration of dissolution results in the breakdown. This figure also shows that when borate ion is added to the sulphate solution, the retardation of the repassivation with the increase in the potential is suppressed slightly, and E_b shifts to noble potential. The buffer action of borate solution is supposed to restore the concentration of H^+ ion produced by Eqs.(4-2) and (4-5) in the vicinity of the newly created surface. This buffer action promotes the film formation reactions of Processes A and B, and then, the reaction of Process C is effectively inhibited.

Figure 4-9 illustrates the repassivation and breakdown. In the case of the repassivation, the slip step is covered rapidly with a passive film, and then the active dissolution is suppressed. On the other hand, an active dissolution occurs through the slip step to form porous and non-protective corrosion

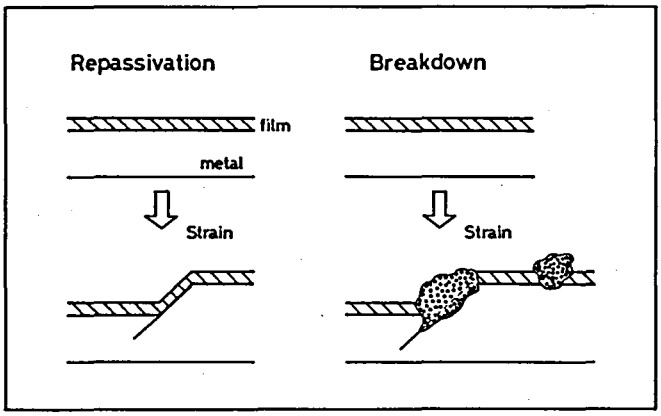

Fig.4-9 Schematic drawing of repassivation and breakdown on the slip step which emerges due to elongation.

products leading to the breakdown when the applied potential is more noble than the critical potential. Furthermore, this figure also describes that the passive film already formed by the repassivation is broken in the breakdown potential region even though no straining is applied in some cases. In other words, the critical potential for breakdown of passivity, E_c, is also found in the polarization curve, as shown in Figs.4-3 and 4-4. These facts mean that SO_4^{2-} ion not only disturbs the repassivation of newly created surface but also breaks down the pre-formed passive film. Similar behavior has been known for Cl^- ion to cause pitting corrosion. Several mechanisms have been proposed[3] for the breakdown of passivity due to the harmful action of Cl^- ion. It seems that a similar mechanism can be applied for the breakdown of passivity by sulphate ions, assuming that SO_4^{2-} breaks the pre-formed passive film. In other words, if SO_4^{2-} ion can reach metal surface through micro defects in the passive film, it promotes the active dissolution in the same way that SO_4^{2-} does at newly created surface emerged due to strain (Process C). Therefore, it is supposed that the critical

potential for SO_4^{2-} ion to break down the passive film is similar to the breakdown potential. However, the critical potential, E_c, is always more noble than E_b at any temperatures tested. An induction period is needed for SO_4^{2-} ion to break down the passive film, because SO_4^{2-} ion has to be transported from solution/film interface to film/metal interface through defects in the passive film. Thus, E_c determined by potentiodynamic polarization curves shows more noble potential than E_b. It is concluded that the straining electrode technique can determine the lowest critical potential for the breakdown of passive film by SO_4^{2-} ion, comparing with any other methods such as the potentiodynamic polarization method.

4.4.2 Effect of temperature and borate ion on the breakdown

The repassivation region extended to noble potential with increasing temperature above 403 K in the solution of 0.1 kmol·m^{-3} Na_2SO_4 as shown in Fig.4-3. The more stable passive film was considered to be formed at a higher temperature in this environment. On the other hand, no breakdown occurred below 403 K. Therefore, a very narrow repassivation region was observed for about 400 $\sim$ 420 K. In other words, the passivity of nickel is unstable in this temperature range. The temperature range of unstable passivity of nickel was also found for around 400 $\sim$ 450 K in the borate buffer solutions added with various concentrations of SO_4^{2-}.

As discussed in Chapter III, the more protective films are formed on iron at the higher temperature above 400 K in 0.1 kmol·m^{-3} Na_2SO_4. A similar change in the property of passive film likely occurs for nickel in this environment. Namely, defects in the passive film on nickel seem to decrease

with increasing temperature.

The higher concentration of SO_4^{2-} ion gives less noble E_b as shown in Fig.4-5. However, E_b in the borate buffer solution with 0.1 kmol·m^{-3} Na_2SO_4 is more noble than that in the sulphate solution without borate. It is concluded that sulphate ions cause the localized attack on nickel, but borate ion inhibits the harmful action of SO_4^{2-}.

4.4.3 Consideration to localized corrosion of high nickel alloys

Much attention has been paid to the fact that sulphur species cause some contamination leading to localized corrosion of both nickel and iron base alloys in high temperature and high pressure water environment[4]-[7]. It was suggested that sulphur species are derived from ion exchange resins[8] and condense in crevice to cause breakdown. It was reported[8] that thick and porous corrosion products were formed on Alloy 600 in acidic solutions. The corrosion products thus formed are quite similar to that found for the breakdown in this study. In the case of Alloy 600, Taylor et al.[9],[10] reported that the accumulation of sulphate ion which leads to acidification is supposed to be the main reason for IGSCC at 561 K.

The breakdown phenomena may provide a key for understanding the mechanism of localized attacks of high nickel alloys in the high temperature and high pressure water environments. The breakdown at higher temperature is highly possible to occur, if enough SO_4^{2-} is enriched in the crevice, even though the breakdown occurred most readily at 403 K in the present experiment. Thus, the contamination with sulphate ion should be avoided as far as possible, in order to use the high nickel

alloys with enough reliability.

4.5 Conclusions

Repassivation behavior on nickel was examined in solutions containing SO_4^{2-} ion.

(1) Repassivation behavior was divided into two types, according to the applied potential and temperature. The first type showed a rapid decay of anodic current and was called the repassivation. In the second type, the anodic current showed no rapid decay and sometimes increased gradually even after straining was stopped. The second type was called the breakdown. The breakdown was observed at potentials more noble than a critical potential, called the breakdown potential. The potential/temperature/SO_4^{2-} concentration diagram showing the breakdown region was shown in Figs.4-3 and 4-5.

(2) The breakdown was caused by the presence of SO_4^{2-}, which adsorbed on the bare surface preferentially to bring about local hydrolysis, resulting in the formation of porous and non-protective hydroxide of $Ni(OH)_2$. Thus, the dissolution of nickel continued, leading to the breakdown. On the other hand, the borate ion inhibited the harmful action of SO_4^{2-} ion.

(3) The breakdown potential shifted to a more noble region with the increase in temperature above 403 K, but breakdown was not observed below 393 K. Therefore, it was concluded that there exists an unstable potential range for passivity of nickel in this environment, around 400 $\sim$ 450 K.

(4) The breakdown phenomena found in this study may provide a clue for understanding the localized attack observed for high nickel alloys in high temperature and high pressure water.

REFERENCES

(1)R. L. Cowan and R. W. Staehle : J. Electrochem. Soc., 118 (1971), 557.

(2)N. Sato and G. Okamoto : J. Electrochem. Soc. 110 (1963), 605.

(3)J. R. Galvele : "Passivity of Metals", Ed. by R. P. Frankenthal and J. Kruger, Electrochemical Society (1978), p.285.

(4)R. C. Newman, R. Roberge and R. Bandy : Corrosion, 39 (1983), 386.

(5)S. Szklarska-Smialowska and G. Cragnolino : Corrosion, 36 (1980), 653.

(6)P. M. Scott, A. E. Truswell and S. G. Druce : Corrosion, 40 (1984), 350.

(7)Wen-Ta Tsai, A. Moccari, S. Szklarska-Smialowska and D. D. MacDonald : Corrosion, 40 (1984), 573.

(8)D. A. Vermilyea : Corrosion, 29 (1973), 442.

(9)D. F. Taylor : Corrosion, 35 (1975), 550.

(10)C. A. Caramihas and D. F. Taylor : Corrosion, 40 (1984), 382.

CHAPTER V

Straining Electrode Behavior of Iron in High Temperature and High Pressure Borate Buffer Solution

5.1 Introduction

Chapter III dealt with the initial stage of anodic behavior on iron in a high temperature and high pressure sodium sulphate solution. A passive film grew following the parabolic growth law, but the reaction constant showed a negative temperature dependence at passive potentials of 503 ∿ 573 K. Therefore, it has been concluded that a more compact and more protective film was formed at the higher temperatures. Furthermore, no passivation was observed in the temperature range between 373 and 463 K.

Sodium sulphate solution has been used widely as an electrolyte for the electrochemical measurements in high temperature and high pressure water. However, SO_4^{2-} ion caused the breakdown of passivity of nickel in the temperature range between about 400 and 450 K, as described in Chapter IV. It was also found for iron that a similar breakdown or no passivation of iron occurred owing to the presence of SO_4^{2-} ion, as discussed in Chapter III. Therefore, the sulphate solution seems to be not suitable for the electrochemical measurements simulating for the corrosion behavior in high temperature and high purity water.

Iron is, however, known to form a stable passive film in the borate buffer solution at room temperature[1]. Therefore, the borate buffer solution was used for the analysis of the initial process of dissolution and repassivation of iron in the present experiment.

5.2 Experimental

Thin iron wire (0.35mm diameter) was used as the working electrode, whose chemical composition is as follows : O 0.029, N 0.0004, C 0.001, Si 0.003, Mn <0.001, Ni <0.001, P 0.002, S 0.001, Al <0.001 (mass %) and Fe balance. The wire specimens were made of electrolytic iron which was remelted in a vacuum. The specimen was degreased in acetone and was solution annealed in a vacuum at 1073 K for 900 s, followed by water quench. The specimen surface was neither polished nor given any further treatment. The electrolyte used in the present experiment was the borate buffer solution of 0.15 kmol·$m^{-3}H_3BO_3$ + 0.0375 kmol·$m^{-3}Na_2B_4O_7$, prepared with reagent grade chemicals and distilled water, and was deaerated with high purity N_2 gas at room temperature before heating.

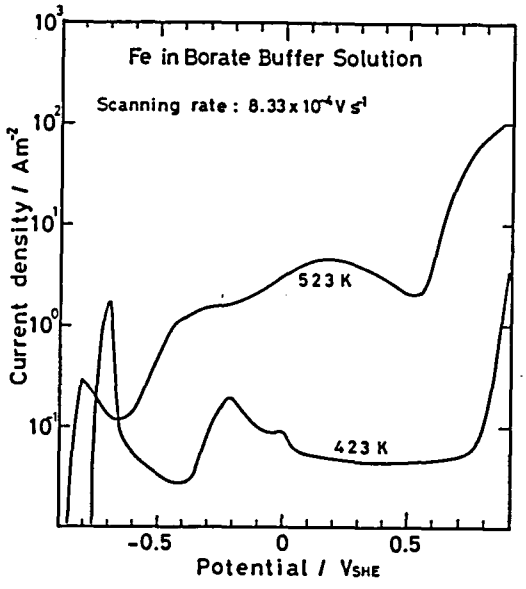

Fig.5-1 Polarization curves of iron in borate buffer solution.

The straining electrode technique has been described in Chapter II. Soon after a test temperature was attained, the potential of specimen was polarized rapidly from the corrosion potential to a noble potential and kept for about 1000 s to obtain a steady passive surface. In the present experiment, the strain given by an elongation was about 0.8 %, with the strain rate being between about 0.3 and 0.4 s^{-1}.

5.3 Results

5.3.1 Polarization curves

Polarization curves of iron in the borate buffer solution at 423 and 523 K are shown in Fig.5-1. Iron shows a wide and steady passive region at the both temperatures, in contrast to that iron showed passive state at 523 K but it showed no passivation at all at 423 K in 0.1 kmol·m^{-3} Na_2SO_4, as stated in Chapter III

It is noticeable that the current density passes a minimum at about -0.5 V, then increases with increasing potential and comes to the secondary passive state in the potential region from 0 to 0.7 V at 423 K and around 0.5 V at 523 K.

5.3.2 Repassivation behavior

Typical changes in the anodic current with time are shown in Fig.5-2. The current density on the newly created surface decayed following the power law :

$$i = at^{-n} . \qquad (5\text{-}1)$$

The value of n was about 0.75 and was almost independent of

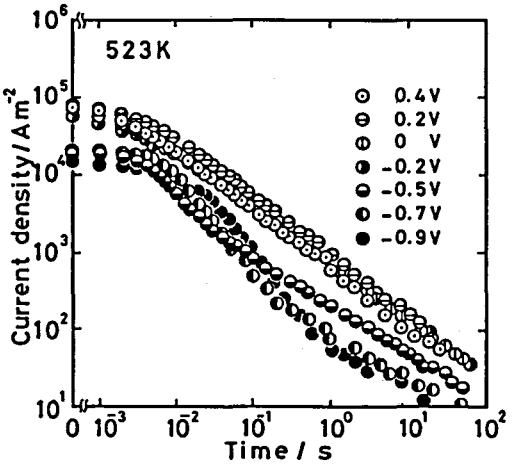

Fig.5-2 Typical changes in the anodic current on the newly created surface of iron at various potentials at 523 K.

potential. The value of n was in the range of 0.7 ∿ 0.8 at temperatures between 473 and 553 K, and changed from about 0.5 to 0.7 with increasing temperature from 313 to 423 K.

Figure 5-3 shows the potential dependence of current density. The suffix to each i indicates the time in second after the elongation was stopped. The transient currents are divided into two groups with respect to their potential dependences. Every current density from i_0 to i_{10} shows no potential dependence in the noble potential region more than -0.2 V. It is called a plateau region. i_0, i_1, and i_{10} increase with increasing potential in a less noble potential region. However, $i_{0.01}$ and $i_{0.1}$ show a small negative potential dependence. These facts suggest that repassivation rate in an early stage in the less noble potential region is different from that in the noble potential region. A similar potential dependence was observed at temperatures between 313 and 553 K.

The mean values of the current density at the plateau region are shown for various temperatures in Fig.5-4. i_0 increases

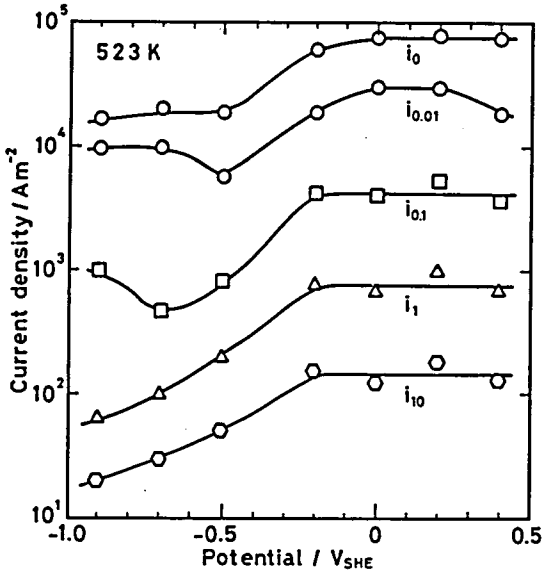

Fig.5-3 Potential dependence of the initial current density, i_0, and transient anodic current density at 0.01, 0.1, 1 and 10 s after elongation was stopped, as indicated by subscripts, at 523 K.

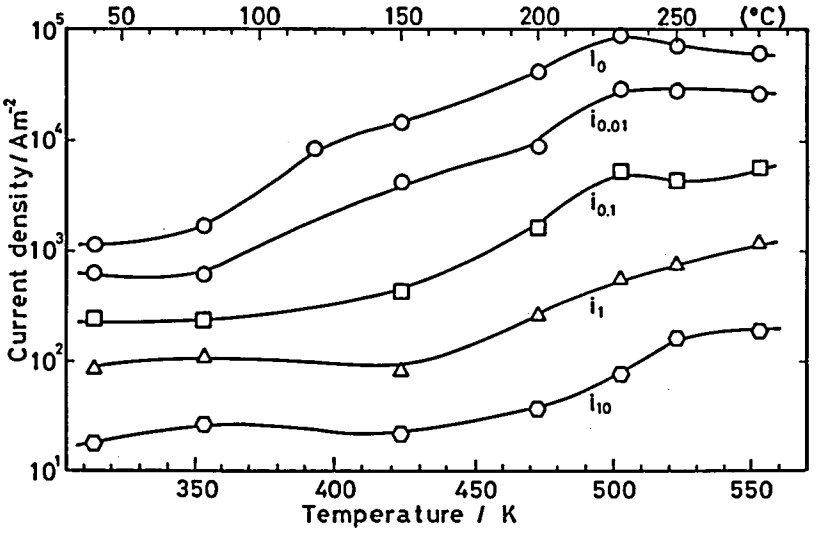

Fig.5-4 Temperature dependence of the transient anodic current density at the plateau potential region shown in Fig.5-3.

with increasing temperature and shows a maximum at 503 K, and then decreases slightly. The distance between each curve in this figure is proportional to the repassivation rate. The wider distance means the faster repassivation. The repassivation rate shows almost no temperature dependence in the temperature range from 423 to 553 K, but decreases with decreasing temperature below 423 K.

The current density passed through the newly created surface is the sum of two currents :

$$i = i_{dis.} + i_{film} , \tag{5-2}$$

where $i_{dis.}$ is the dissolution current and i_{film} is the film formation current. Thus, the observed charge density, Q, is also the sum of two charges, corresponding to the above two currents :

$$Q = Q_{dis.} + Q_{film} . \tag{5-3}$$

There is, however, no decisive method to separate experimentally these two charge densities. It is assumed that the thickness of film is proportional to Q, because a part of Q precipitates as film. Thus, the relation between i and Q, instead of Q_{film}, is analyzed as a function of time.

The charge density that has passed through the newly created surface is estimated by

$$Q(t) = (q_0 + \int_0^t \Delta I(t)dt) / \Delta S , \tag{5-4}$$

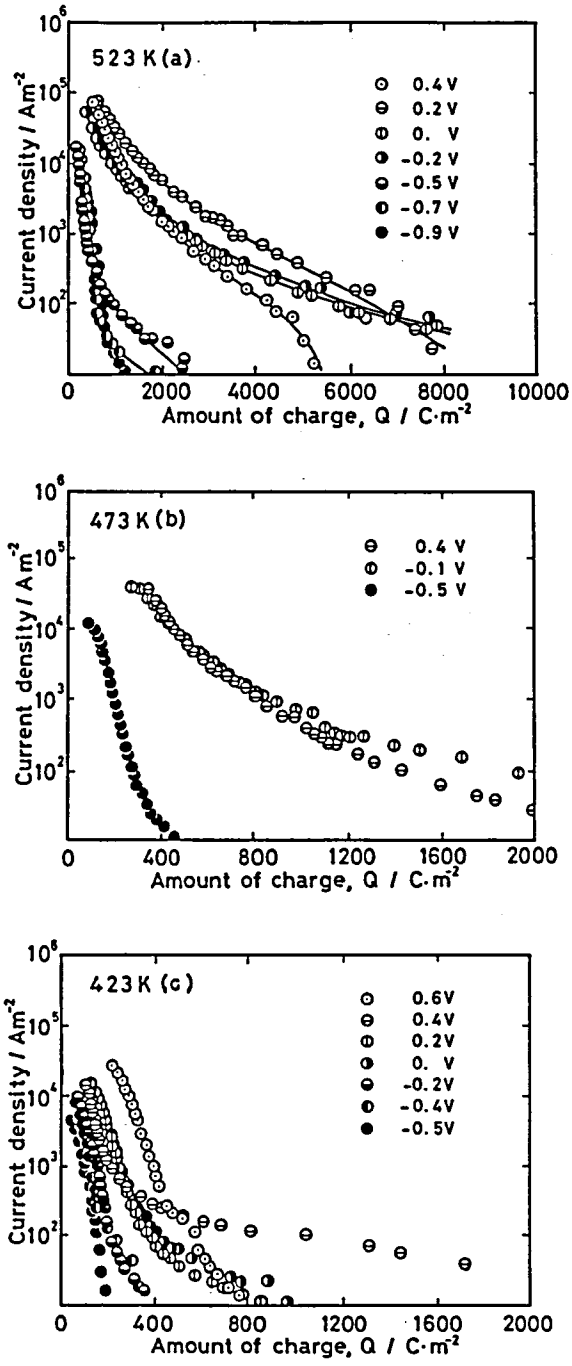

Fig.5-5 Changes in current density, i , with the increase in charge density, Q , at various potentials for (a)523 K, (b)473 K and (c)423 K.

where t is the time elapsed after the straining is stopped and q_0 the charge passed during the elongation. The integration of this equation was performed by a summation of i vs t curves measured in the experiment.

Relations between log i and Q at 523, 473 and 423 K are shown in Fig.5-5. log i vs Q curves at various potentials at 523 K are divided into two groups, as shown in Fig.5-5(a). Decay behavior of log i with the increase in Q shows no apparent potential dependence at noble potentials of 0.4, 0.2, 0, and -0.2 V. The other group of decays at -0.5, -0.7 and -0.9 V also has no potential dependence, although relations between i and t had potential dependence, as shown in Fig.5-3. But, an obvious difference in the log i vs Q relation between these two groups is found. The two groups were also recognized at 473 and 423 K, as shown in Figs.5-5(b) and (c), respectively.

5.5 Discussion

5.5.1 Initial current on the newly created surface

Initial process of the anodic reaction on the newly created surface of iron is supposed to be controlled by dissolution of Fe^{2+} ion at the metal/solution interface, because i_0 showed a positive potential dependence in a potential range near open circuit potential. Thus, the rate determining step of the initial dissolution process seems to be an activation controlled. On the other hand, i_0 showed the plateau region in the more noble potential region as shown in Fig.5-3. i_0 at the plateau region showed a monotonous temperature dependence in a temperature range from 313K to 503K as shown in Fig.5-4. The Arrhenius plot of i_0 at the plateau region is shown in Fig.5-6. A linear relation

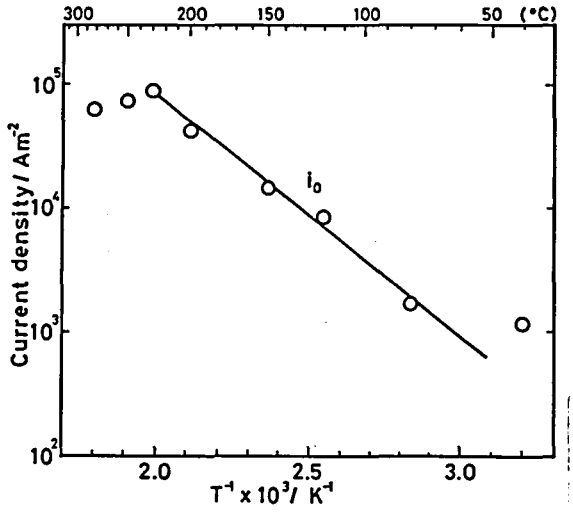

Fig.5-6 Temperature dependence of i_0 in the plateau region as shown in Fig.5-3.

between i_0 and the reciprocal of absolute temperature, 1/T, is recognized, the apparent activation energy being 36 kJ/mol. The value suggests that the initial dissolution of Fe^{2+} in the plateau region is determined by diffusion in aqueous solution and not by the applied potential, because the activation energy for diffusion in aqueous solution is known to be in the range of few tens kJ/mol[2].

On the contrary, i_0 showed a negative temperature dependence above 503 K as can be seen clearly in Figs.5-4 and 5-6. It is unreasonable that the diffusion process shows a negative temperature dependence. It should be noticed that i_0 is actually not the true initial current density on the bare surface. The film formation had been already started even at the time when straining was stopped, because a little time was always needed to give a constant amount of elongation. Therefore, i_0 includes influences of both active dissolution current on the newly created surface and the early stage of repassivation. Thus, it is supposed that the decrease in i_0 above 503 K is due to the

rapid film formation before the elongation is stopped.

5.5.2 Repassivation behavior

Corrosion mechanisms of carbon and low alloy steels in the high temperature water environment were recently reviewed and discussed in detail by Tomlinson[3]. A porous double magnetite layer has been demonstrated to form on iron and carbon steels in high temperature and high pressure aqueous solutions. The corrosion process involves the transportation of reaction species by diffusion in the liquid phase contained in pores or other defects in the magnetite layer[4],[5].

Potter and Mann[6],[7] reported that the corrosion rate of mild steel in high temperature caustic solution decreases with time following the parabolic law. They concluded that the rate of the process is controlled by the diffusion in liquid phase.

The mechanism of magnetite formation is generally accepted as follows. Fe^{2+} ion which is dissolved at the metal/film interface diffuses outward through the diffusion paths which are consist of pores, grain boundaries or other defects in the magnetite layer. Then, Fe^{2+} deposits on the outer surface of the magnetite layer, and also a considerable part of Fe^{2+} ion is dissolved away into bulk solution at the same time. Therefore, the rate of this process is determined by the diffusion of Fe^{2+} ion in the liquid phase which is contained in the diffusion paths. Thus, the parabolic rate law is observed.

An analysis of the relation between the current density and the charge density provides informations about the film formation mechanisms. In the case of parabolic rate law, a linear relation between 1/i and Q is to be expected. This relation, however, was not observed in the present experiment except the cases at 313

and 353 K.

Most of kinetic studies in the past has been performed for rather longer time than that in this study. On the other hand, the straining electrode test examines the very initial process from emergence of bare surface for few tens of seconds. Therefore, the film growth process has not reached to a steady state even at the end of the straining electrode test. In The rate of initial dissolution proved to be determined by diffusion in aqueous solution and not by the applied potential, as stated before. Furthermore, relations between log i and Q showed no potential dependence, as shown in Fig.5-5, although the relations were divided into two groups according to potential. These facts suggest that the film growth is not controlled by the applied potential either. Therefore, the initial process of film formation, observed in the present experiment, is controlled by the diffusion of ion in aqueous solution. The first process at the emergence of bare surface is considered to be the dissolution of Fe^{2+} ion, a part of which is dissolved away into solution and/or precipitates at the outer surface of the magnetite layer. It is also considered that the precipitation/ dissolution ratio changes with time. The change in the structure of diffusion paths with time is expected, in addition to this change in the precipitation ratio. That is, the number of diffusion paths and its shape will alter with time. Consequently, the parabolic rate law has to be modified by assuming the above factors.

In general, the relationship between J, the flux of reaction species through the reaction products, and d, their thickness, is expressed by the following equation.

$$J = k D / d , \qquad (5\text{-}5)$$

where k is constant and D diffusion constant, assuming that the diffusion paths are present uniformly in the reaction products. In the case of anodic film growth, Eq.(5-5) is equivalent to the next equation, which is known as the parabolic law for anodic film growth :

$$i = k' / Q , \qquad (5\text{-}6)$$

assuming that the charge density, Q, is proportional to the film thickness.

The flux of Fe^{2+} ion is proportional to the number of diffusion paths per unit area, N(Q), and their size, A(Q), both of them being functions of Q. In addition, since the film thickness is proportional to the precipitation charge which is a part of the total charge density, the ratio of $Q_{precipitation}/Q_{total}$ is also a function of Q, $\alpha(Q)$. Thus, Eq.(5-6) is modified to the following equation :

$$i = N(Q)\cdot A(Q)\cdot k' / \alpha(Q)\cdot Q , \qquad (5\text{-}7)$$

Figure 5-7 shows the relationship between i and Q in log-log plots at the plateau potential region for various temperatures. Their slopes ranged from -2.5 to -3.5 above 423 K and were about -1 at 313 and 353 K. If the relation between i and Q followed Eq.(5-6), namely the parabolic law, the slope should be -1. This figure shows that the parabolic law can be applied only for 313 and 353 K. The slopes at higher temperatures were rather larger than that expected by Eq.(5-6).

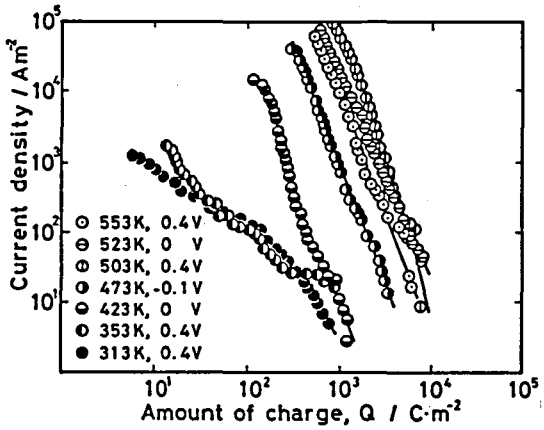

Fig.5-7 Change in the current density, i , with the increase in charge density, Q , at the plateau potential for various temperatures.

This fact suggests that the three factors of N(Q), A(Q) and α(Q) added to Eq.(5-6) depended on Q. Almost linear relations were observed in log i vs log Q plots as shown in Fig.5-7. Consequently, the above three factors are possible to be expressed by power functions of Q as a first approximation. The large change in α(Q), however, can not be expected, because the precipitation ratio, α(Q), is in the range of 0 to 1, and is not so small value at the initial stage of repassivation[8]. Thus, this factor, α(Q), can be equated to a constant value, . Therefore, Eq.(5-7) is modified to

$$i = k'' \cdot Q^{m} \cdot Q^{1} / \alpha \cdot Q \qquad (5\text{-}8)$$

$$= k'' \cdot Q^{m+1} / \alpha \cdot Q \,, \qquad (5\text{-}9)$$

$$= k'' \cdot Q^{m+1-1} / \alpha \,. \qquad (5\text{-}10)$$

The slopes of log i vs log Q plots were -2.5 ∿ -3.5. Thus, m+1 = -1.5 ∿ -2.5 is obtained. This result indicates that a large change in the structure of the magnetite layer took

place with the accumulation of charge density.

As discussed in Chapter III, iron showed very slow repassivation rate in 0.1 kmol·m^{-3} Na_2SO_4 above 503 K, until charge density reached $10^3 \sim 10^4$ C·m^{-2}. After this initial dissolution period, the repassivation followed the parabolic rate law. A considerable amount of charge was consumed by dissolution of ions into solution or formation of non-protective hydroxide in the sulphate solution in the initial period. A porous magnetite layer which was less protective than that formed in the borate buffer solution was formed during the initial dissolution period. Then, this initially formed porous magnetite layer grew continuously with the constant number and the constant size of pores. Therefore, the parabolic law was observed.

On the other hand, it is well known that the magnetite layer formed on iron in high temperature and high pressure water consists of crystalline particles larger than a few μm[3]. Thus, it is supposed that such a large size particle can not fully cover the bare surface during the short time of the straining electrode test. Therefore, the nucleation and rapid growth of the particles occurred with a rapid change in the size and the number of diffusion paths, defined as A(Q) and N(Q) in Eq.(5-7), during the initial period. Thus, a large change in the structural factors of expressed as Q^{m+1} was expected, with the power of m+1 being $-1.5 \sim -2.5$. Consequently, the more rapid repassivation was observed compared with that of the parabolic law.

5.5.3 Effect of potential

The change in current density was divided into two groups

according to the applied potential, namely, the noble and the less noble potential groups. The critical potential for dividing was about -0.5 V at 523 K. The current density of the polarization curves increased slightly from -0.6 V for 523 K and from -0.4 V for 423 K as shown in Fig.5-1. This increase seems to be related to the oxidation of Fe^{2+} ion to Fe^{3+} ion. Fujii et al.[9] observed that the corrosion products formed on mild steel at around the corrosion potential were Fe_3O_4, and that a small amount of α-Fe_2O_3 was also detected together with Fe_3O_4 at higher potentials by a transmission electron diffraction. Thus, they concluded that a peak potential observed in the polarization curve at around -0.25 V at 553 K corresponded to the oxidation of Fe_3O_4 to Fe_2O_3, where this potential was measured by external SCE reference electrode. Thus, the potential seems to be equivalent to about -0.5 V at 553 K. It is supposed that the change in repassivation behavior at the critical potential around -0.5 V is due to the change in the reaction species from Fe^{2+} to Fe^{3+} and/or in the structure of reaction products as film. Thus, the film composition is prone to change from magnetite to hematite in this noble potential region. The larger anodic current flows than that at less noble potentials, because the formation of Fe^{3+} needs more charge than that of Fe^{2+}.

Umemura and Kawamoto investigated the SCC susceptibility of carbon steel in high temperature and high pressure water by SSRT[10]. They reported that carbon steel is susceptible to SCC in aerated pure water at 523 K, namely at a noble corrosion potential, but is not in deaerated pure water, in which corrosion potential is less noble. It is also reported that SCC occurs only in a potential region of more noble than -0.4 V in 0.1 kmol·

$m^{-3}Na_2SO_4$ under controlled potential condition. Thus, it is more likely that the change in repassivation behavior observed for iron at the critical potential has a close relation to the susceptibility of SCC of iron base alloys.

5.5.4 Effect of temperature

There are some reports that the corrosion rate of iron, carbon steels and stainless steels shows a maximum around 523 K in various environments[11]-[13]. The relation between log i and log Q in Fig.5-7 showed the maximum current density at 503 K, and also i_0 showed a maximum at 503 K. The passive film on a newly created surface of iron grew following a parabolic growth law : $i = k/Q$, in 0.1 kmol·$m^{-3}Na_2SO_4$ above 503 K up to 573 K, as discussed in Chapter III. The rate constant, k, however, showed negative temperature dependence. Namely, the repassivation rate showed a minimum at 503 K in the temperature range. Moreover, the initial dissolution charge, $Q_{d,i}$, which passed before the parabolic film growth started, showed a maximum at 503 K. It should be noted that the maximum repassivation rate was observed at around 500 ∿ 500 K not only for the long time but also for the very early period examined by the straining electrode test.

The repassivation rate was independent of temperature above 423 K, and the maximum initial current density was found at 503 K as discussed in Fig.5-4. Consequently, a favorable condition for SCC could be attained at 503 K, at which the highest dissolution on the bare surface took place with a rapid repassivation, because SCC is supposed to occur when the active dissolution is fast and the repassivation is rapid. The maximum susceptibility to SCC of iron base alloys actually has been reported around 523 K in the literature[14],[15],

corresponding to this condition. Thus, the straining electrode technique could clarify a favorable condition for SCC propagation.

5.5 Conclusions

The initial stage of the repassivation process of iron was investigated in the high temperature and high pressure borate buffer solution.

(1) The current density on the newly created surface decayed following the power law : $i = at^{-n}$ with n ranging from 0.7 to 0.8 above 473 K.

(2) The repassivation process seemed to be controlled by the diffusion in aqueous solution, but was more rapid than that expected for the parabolic rate law.

(3) The repassivation process was controlled by the diffusion of Fe^{2+} ions in the diffusion paths, which consist of pores or other defects in the magnetite layer. The rapid repassivation rate was supposed to be caused by the decrease in the number and the size of these diffusion paths with time during the initial stage of film formation.

(4) The repassivation behavior was divided into two groups according to the applied potential, the critical potential being around -0.5 V at 523 K. The more rapid repassivation was observed at the more noble potentials. A change in reaction products from Fe_3O_4 to Fe_2O_3 seemed to occur above the critical potential.

(5) A favorable condition for SCC was attained at 503 K, at which the highest dissolution on the bare surface took place with a rapid repassivation.

REFERENCES

(1)M. Nagayama and M. Cohen : J. Electrochem. Soc., 109 (1962), 781.

(2)R. Parsons : "Handbook of Electrochemical Constants", Butterworth Sci. Publ., London (1959).

(3)L. Tomlinson : Corrosion, 37 (1981), 591.

(4)J. E. Castle and H. G. Masterson : Corros. Sci., 6 (1966), 93.

(5)G. J. Bignold, R. Garnsey, and G. M. W. Mann : Corros. Sci., 12 (1972), 325.

(6)E. C. Potter and G. M. W. Mann : Proc. 1st Int. Cong. on Metallic Corros., London, (1961), p.417.

(7)G. M. W. Mann : " High Temperature High Pressure Electrochemistry in Aqueous Solution", NACE (1976), p.34.

(8)J. B. Lumsden and R. W. Staehle : "High Temperature and High Pressure Electrochemistry in Aqueous Solution", NACE (1976), p.400.

(9)T. Fujii, T. Kobayashi, and G. Ito : " High Temperature High Pressure Electrochemistry in Aqueous Solution, NACE (1976), p.416.

(10)F. Umemura and T. Kawamoto : Boshoku Gijutsu, 30 (1981), 276.

(11)T. Maekawa, M. Kagawa and N. Nakajima : J. Japan Inst. of Metals, 31 (1967), 1213.

(12)M. Warzee, J. Hennaut, M. Maurice, C. Sonnen, J. Waty and Ph. Berge : J. Electrochem. Soc., 112 (1965), 670.

(13)G. Ito, Y. Shimizu and S. Sato : Boshoku Gijutsu, 18 (1969), 345.

(14)H. Choi, F. H. Beck, Z. Szklarska-Smialowska, and D. D. MacDonald : Corrosion, 38 (1982), 136.

(15)N. Ohnaka, S. Shoji, E. Kikuchi, A. Minato and H. Ito : Boshoku Gijutsu, 32 (1983), 214.

CHAPTER VI

Repassivation Behavior of Newly Created Surface of Nickel in High Temperature and High Pressure Neutral Solution

6.1 Introduction

A large number of work has been performed on the kinetics of active dissolution and film growth on nickel in acidic and neutral solutions at room temperature[1]-[4]. Little work, however, has been performed on the basic electrochemical process of nickel or high nickel alloys in the high temperature and high pressure water environment[5]. Chapter IV dealt with the rapid straining electrode behavior of nickel in high temperature and high pressure aqueous solution containing sulphate ion. It was revealed that the passive film of nickel is broken down locally due to an aggressive action of sulphate ion in a specific temperature range. In the present experiment, the initial process of anodic behavior of newly created surface on nickel is examined in the neutral borate buffer solution.

6.2 Experimental

The specimen used for the present experiment was a nickel wire (0.35 mm diameter) of commercial purity, whose chemical composition was : 0.028 C, 0.0032 P, 0.0037 S, 0.06 Si, 0.38 Mn, 0.29 Co, 0.09 Fe, 0.007 Cu, 0.001 Cr (mass %), and balance Ni. The wire was degreased in acetone and then annealed in a vacuum at 1073 K for 900 s, followed by water quench. The specimen surface was neither polished nor given any further treatments. The electrolyte used was the borate buffer solution of 0.15 kmol·

$m^{-3}H_3BO_3$ + 0.0375 $kmol \cdot m^{-3}Na_2B_4O_7$ (pH=8.5 at room temperature), prepared with reagent grade chemicals and distilled water.

The straining electrode technique has been described in Chapter II. The experimental procedures were almost the same as that described in Chapter V. The strain given for an elongation was about 1.5 %, with strain rate being approximately 0.5 s^{-1}.

III. Results

6.3.1 Polarization curves

Polarization curves of nickel in the borate buffer solution at several temperatures are shown in Fig.6-1. There always exists the stable and wide passive potential region at any temperature tested, in contrast that nickel showed no stable passive state in solutions containing SO_4^{2-} ion in a specified temperature range, as described in Chapter IV.

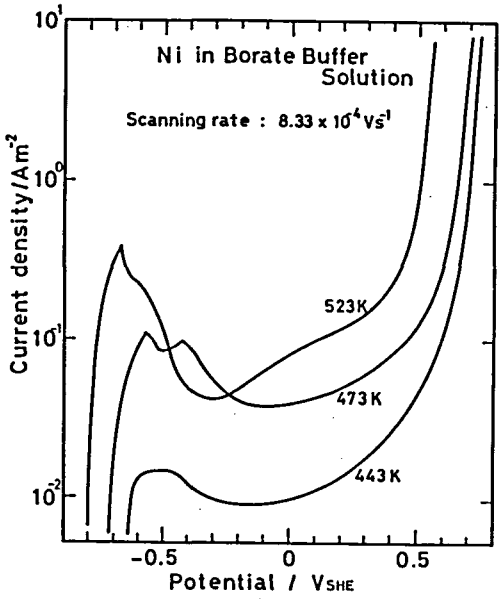

Fig.6-1 Anodic polarization curves of nickel in borate buffer solution.

The straining electrode test was conducted at the passive potentials observed in these polarization curves.

6.3.2 Straining electrode behavior

Typical changes in anodic current with time are shown in Fig.6-2. The current density on the newly created surface decayed following the power law :

$$i = a\, t^{-n}. \qquad (6\text{-}1)$$

The value n ranged from 0.5 to 0.8. In the most cases, the relation described by Eq.(6-1) was observed from about 5 ms for 3 decades. The value of n showed no considerable dependence upon temperature and also upon potential.

In order to discuss the repassivation behavior on the newly created surface, it is necessary to estimate the accumulated charge density that has passed through the newly created surface,

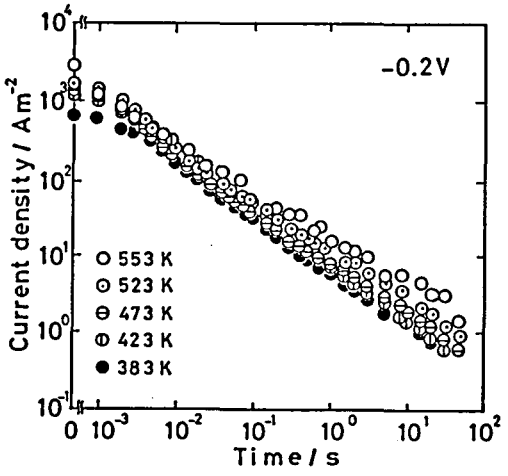

Fig.6-2 Typical changes in the anodic current density with time on the newly created surface of nickel.

In the literature[6], the passive film formation and its growth are described by several kinetics : a logarithmic rate law, inverse logarithmic rate law, parabolic rate law, power law and others. The first three kinetics are expressed by the following equations as functional relations between current density, i, and accumulated charge density, Q_{film}, which is proportional to the thickness of the passive film :

$$\text{Logarithmic} \quad : \quad i = A \exp (bE - cQ_{film}) \qquad (6\text{-}2)$$

$$\text{Inv. logarithmic} \quad : \quad i = i_0 \exp (aE / Q_{film}) \qquad (6\text{-}3)$$

$$\text{Parabolic} \quad : \quad i = k / Q_{film} , \qquad (6\text{-}4)$$

where E is an applied potential and i_0, a, b, c, and A are constants.

By examining the experimental data in log i vs Q, log i vs 1/Q and 1/i vs Q plots, the proper relation can be determined.

Examples of plots in log i vs Q and in 1/i vs Q using the same experimental data are shown in Figs.6-3(a) and (b), respectively. These figures revealed that the data obtained in the present experiment can not be described in a single kinetics. Most of data, however, fitted with a logarithmic rate law in the initial stage and with a parabolic rate law in the later stage. This behavior corresponds to the two stage process as discussed later. The linear region of curves in Fig.6-3(a) does not intersect with y-axis(Q=0), because some charge less than 10 $C \cdot m^{-2}$ flows during the elongation. Thus, the maximum current density, i_0, was not the true current density on the newly created surface, because the film formation already occurred during the elongation. If the logarithmic rate law could be applied to the initial stage of the film growth, the

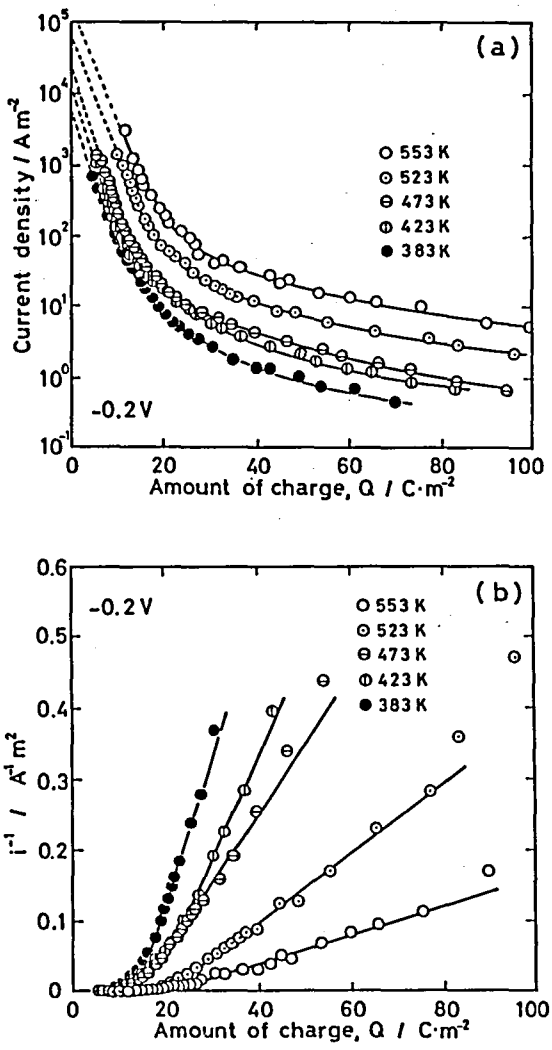

Fig.6-3 Typical changes in the current density, i, with increasing charge density, Q, plotted as (a)log i vs Q, and (b) 1/i vs Q.

current density at Q=0 is estimated by an extrapolation of the linear portion of curves in Fig.6-3(a) to y-axis. The value given above is called $i_{Q=0}$. The values of $i_{Q=0}$ are shown in Fig.6-4 as a function of potential at various temperatures. $i_{Q=0}$ increases with increasing potential in a less noble potential region, then exhibits a plateau in the noble potential region. $i_{Q=0}$ in the plateau region increases with increasing temperature, although a scatter is observed. Similar plateau was also observed in other metal/environment systems, as discussed in Chapters III, IV and V.

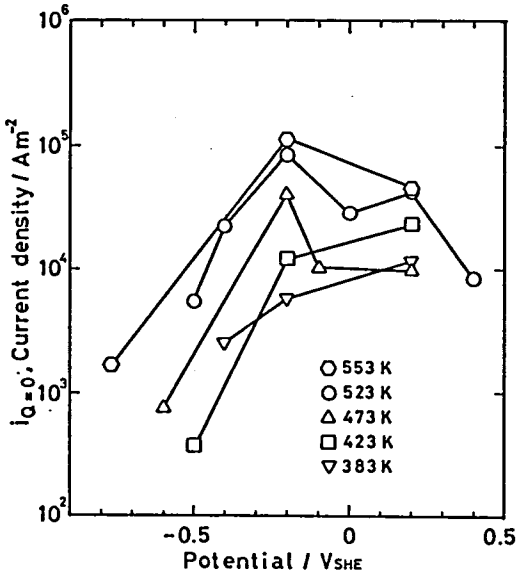

Fig.6-4 Potential dependence of the estimated current density on the bare surface, $i_{Q=0}$, which was obtained by extrapolation of the linear portion of curves in Fig.6-3(a) to Q=0.

6.4 Discussion

6.4.1 Early stage of behavior on newly created surface

In this section, the early stage is discussed, because

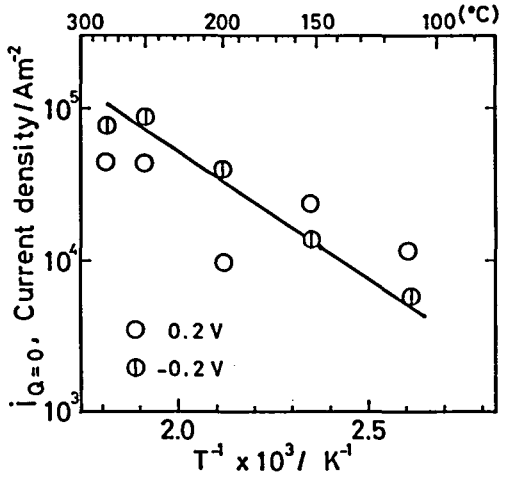

Fig.6-5 Temperature dependence of $i_{Q=0}$ in the plateau region shown in Fig.6-4.

Figs.6-3(a) and (b) showed two distinct stages in the repassivation process. The temperature dependence of $i_{Q=0}$ in the plateau region is described as a function of 1/T in Fig.6-5. A linear relation between $i_{Q=0}$ and 1/T is recognized, even though the values show a scatter. From this figure, the apparent activation energy, ΔH_a, is estimated to be 32 kJ/mol, which is of the same order as that of the activation energy for diffusion in aqueous solution[5]. Thus, the reaction rate just after the bare surface was exposed could be explained by the diffusion of dissolved species from bare surface to bulk solution. The film formation initiated immediately following this initial process.

log i varied linearly with Q in the early stage of repassivation or the film formation, as shown in Fig.6-3(a). Thus, the decay of current density is described in the logarithmic rate law :

$$i = i_{Q=0} \exp(-Q/C) \quad , \qquad (6\text{-}5)$$

The decay parameter, C, is shown in Fig.6-6 as a function of potential at various temperatures. The value of C is independent of potential and temperature. The change in the kinetics from the logarithmic to the parabolic took place at a critical amount of charge density, Q_c. The value of Q_c can be determined by comparing Figs.6-3(a) and (b). Q_c was actually estimated by the extrapolation of the linear portion of parabolic plots toward 1/i=0. Q_c thus estimated increased with increasing temperature, but did not depend on the applied potential, and was almost in the range of 5 to 25 $C \cdot m^{-2}$. If the passive film is assumed to be NiO, whose density is 7.55 g/cm^2, the anodic charge density required for the monolayer oxide formation is calculated to be about 5 $C \cdot m^{-2}$. Therefore, the measured value of Q_c corresponds to 1 ∿ 5 layers of oxide film. Q_c also contains a contribution by the dissolution, because the dissolution current is included in Q, as stated before. In addition, the roughness of the newly created surface was not considered. If these two factors are taken into consideration,

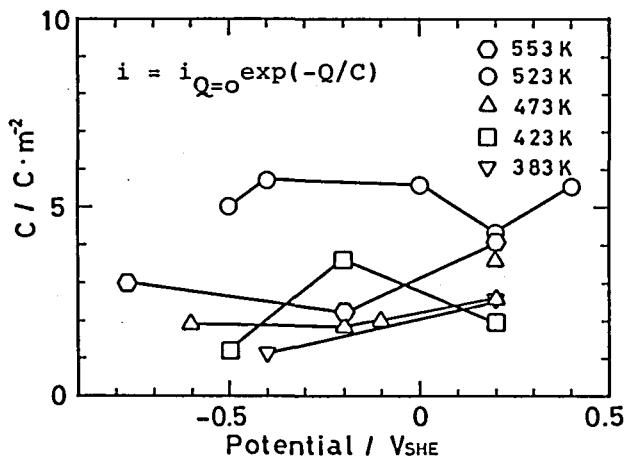

Fig.6-6 Potential and temperature dependence of the decay parameter, C , in the logarithmic rate law described in Eq.(6-5).

the exact accumulated charge corresponding to the change in the kinetics becomes roughly equivalent to the formation of monolayer oxide. Therefore, it can be concluded that the accumulation of charge in the early stage is controlled by the logarithmic rate law until the bare surface is covered with monolayer of oxide film.

Several mechanisms to explain the logarithmic rate law were proposed for formation of the first monolayer of oxide[8]-[10], the process of which involves nucleation and two dimensional extension. In the case of the straining electrode, a newly created surface emerges as slip steps which break down a preformed oxide. Thus, the newly created surface is surrounded by the oxide layer already formed. Therefore, the early stage of the repassivation is the process of filling the emergent slip steps with oxide, which comes from dissolved Ni^{2+} ion and OH^- ion. Consequently, the rate of film growth is determined by the number of slip steps emerged at straining and also the rate of decrease in the number of slip steps. This behavior could be properly explained by the mutual-blockage model proposed by Evans[11].

When the rate of oxide accumulation is proportional to the number of slip steps produced by straining, the following equation is introduced :

$$dQ/dt = k_1 N \quad , \qquad (6\text{-}6)$$

where N is the number of step at time t. According to the mutually-blocking pore mechanism, the process of oxide accumulation in a slip step also affects the decreasing rate of neighboring slip steps. Thus, the chance of decrease of the

steps, -dN, is formulated as follows.

$$-dN = k_2 N dQ \quad . \tag{6-7}$$

The integration of Eq.(6-7) with the condition of $N=N_0$ at $Q=0$, gives

$$\ln(N/N_0) = -k_2 Q \ , \tag{6-8}$$

or

$$N = N_0 \exp(-k_2 Q) \quad . \tag{6-9}$$

From Eqs.(6-6) and (6-9), the rate of oxide accumulation is expressed as

$$dQ/dt = k_1 N_0 \exp(-k_2 Q). \tag{6-10}$$

This equation is equivalent to Eq.(6-5), which was in a good agreement with the experimental results in the early stage.

6.4.2 Steady state growth

The anodic current decayed following the parabolic rate law after the formation of first monolayer oxide, as shown in 1/i vs Q plot of Fig.6-3(b). The parabolic law thus observed suggests that the film growth rate is determined by the diffusion and/or migration of reaction species through the reaction products. The parabolic rate law is described in the following equation, as stated before :

$$i = k / Q \ . \tag{6-11}$$

The rate constant k obtained by the experiment is shown in Fig.6-7 as a function of potential at various temperatures. k is positively dependent not only on temperature but also on potential. This fact suggests that the reaction species move through the film owing to partly a migration of charged ion under a potential gradient in addition to the diffusion under a concentration gradient.

The flux, J, of ions under both the concentration gradient, dC/dx, and the potential gradient, dE/dx, is generally described by

$$J = DdC/dx + ZFC\,\omega dE/dx \quad . \qquad (6\text{-}12)$$

where D and ω are diffusion constant and mobility of moving species, respectively, Z valency of charged ion and F

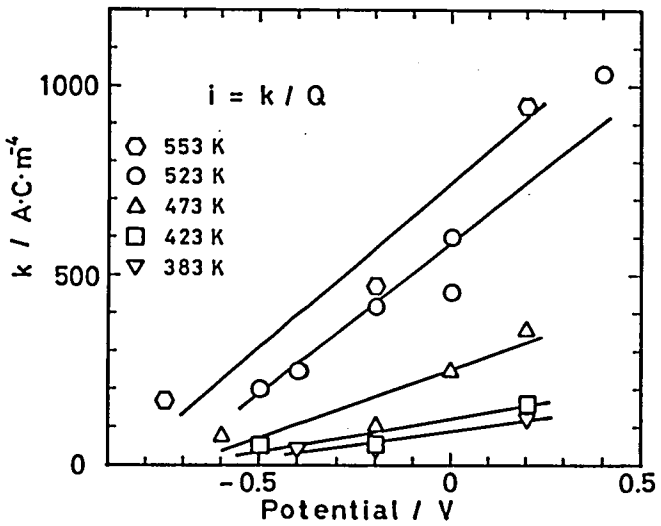

Fig.6-7 Potential dependence of the rate constant k in the parabolic growth law described in Eq.(6-11), at various temperatures.

Faraday's constant. When the length of mass transfer path is small, dC/dx and dE/dx are expressed approximately as $\Delta C/\Delta x$ and $\Delta E/\Delta x$, respectively, where ΔC and ΔE are differences of concentration and potential between two sides of mass transfer path, and Δx its thickness. Thus, Eq.(6-12) is modified to

$$J = D\,\Delta C/\Delta x + ZF\omega C_i \Delta E/\Delta x \qquad (6\text{-}13)$$

$$= D(C_i - C_0)/\Delta x + ZF\omega C_i \Delta E/\Delta x, \qquad (6\text{-}14)$$

where C_i and C_0 are concentration of ion at interfaces of metal/film and film/solution, respectively. Since the concentration of ion in the solution side is almost zero in this experiment, C_0 can be neglected. Thus, Eq.(6-14) is reduced to

$$J = (D + ZF\omega\Delta E)\, C_i / \Delta x \quad . \qquad (6\text{-}15)$$

This equation is equivalent to Eq.(6-11) because Δx is proportional to Q. By comparing Eq.(6-11) with Eq.(6-15), k in Eq.(6-11) can be equated as follows :

$$k \propto (D + ZF\omega\Delta E) \quad . \qquad (6\text{-}16)$$

That is, the rate constant k in the parabolic law includes two factors corresponding to diffusion and migration.

It is difficult to separate above two factors from observed rate constant. Thus, temperature dependence of diffusion constant, D, can not be calculated. However, the temperature dependence of mobility, ω , can be estimated by plotting $\partial k/\partial E$ against 1/T, because $\partial k/\partial E = zF\omega$. The temperature dependence of $\partial k/\partial E$ shows that activation energy of mobility

is 27 kJ/mol, as shown in Fig.6-8. This value is in the range generally accepted for the ion's mobility in aqueous solution[12]. Therefore, it is concluded that the observed parabolic growth is controlled by diffusion and migration in aqueous liquid under the concentration gradient and the potential gradient. It is difficult to estimate which factor of diffusion or migration is more dominant. However, the distinct potential dependence of k in Fig.6-7 suggests that the migration under potential gradient has a large contribution.

It has been reported that the growth of passive film in neutral solutions at room temperature takes place by field assisted ion conduction[13],[14] or place exchange mechanism[15], which follows the inverse logarithmic or the direct logarithmic rate law. Namely, both processes occur in a thin oxide film under a high electric field in solid state. However, the film growth on nickel in high temperature water

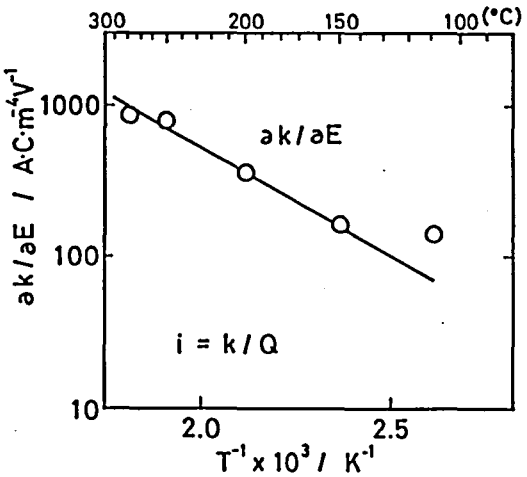

Fig.6-8 Temperature dependence of $\partial k/\partial E$. k is the rate constant of the parabolic growth law shown in Fig.6-7. The temperature dependence of $\partial k/\partial E$ shows that of mobility, ω, of ion, because $\partial k/\partial E = ZF\omega$.

environment observed in this experiment is determined by the parabolic law.

The logarithmic law observed in the early stage and the parabolic law in the later stage suggest the following repassivation mechanism as shown schematically in Fig.6-9. The metal is covered uniformly with a passive film before being provided with the elongation (Fig.6-9(a)). When a strain is given, the preformed passive film is broken by the emergence of many slip steps. The newly created surface, namely, the slip step, is surrounded by preformed passive film, and then nucleation of the oxide film starts at the edge of the preformed film (Fig.6-9(b)). The oxide film extends two dimensionally following the logarithmic rate law, until the newly created surface is covered with monolayer of the film. The surface film has heterogeneous structure, because the metal surface is covered with a mixture of the preformed thick passive film and

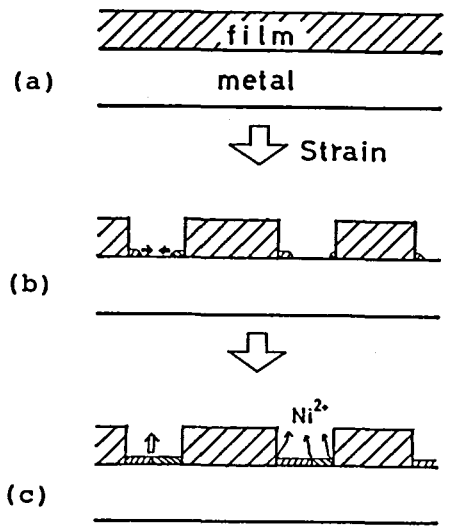

Fig.6-9 A schematic model of the repassivation process of nickel on the newly created surface which emerged due to elongation.

the newly formed thin film. Thus, there are many pores and other defects which contain liquid phase and give paths for transportation of ion. The Ni^{2+} ion dissolved into the pore and/or the other defects at metal/film interface is transferred outward through these paths, and then Ni^{2+} ion deposits as oxide on the outer surface of the passive film(Fig.6-9(c)). This process corresponds to the parabolic growth observed in the later stage. Thus, the rate is determined by diffusion and migration through the liquid phase contained in the defects in the passive film under not only the concentration gradient but also the potential gradient.

It should be emphasized that the specific condition given by the rapid straining provides the heterogeneity of passive film. In addition, the structure of passive film formed at high temperature is quite different from that formed at room temperature.

6.5 Conclusions

Repassivation process of nickel was investigated in high temperature and high pressure borate buffer solution at temperatures up to 553 K.

(1) The current density on the newly created surface decayed following the power law : $i=at^{-n}$ with n ranging from 0.5 to 0.8.

(2) The repassivation process consisted of two stages : the early stage and the later stage.

(3) During the early stage, the newly created surface was covered with monolayer of oxide film following the logarithmic rate law, which was explained by the mutual-blockage model proposed by Evans.

(4) In the later stage, the passive film thickened following the parabolic law with the rate determined by diffusion and migration of Ni^{2+} ion under both the concentration and the potential gradient through liquid phase contained in many pores and other defects in the passive film.

REFERENCES

(1)G. Okamoto and N. Sato : Denki-Kagaku, 27 (1959), 321.

(2)J. L. Ord, J. C. Clayton, and D. J. DeSmet : J. Electrochem. Soc., 124 (1977), 1714.

(3)B. MacDougall and M. Cohen : J. Electrochem. Soc., 124 (1977), 1185.

(4)B. MacDougall and M. J. Graham : J. Electrochem. Soc., 128 (1981), 2321.

(5)R. L. Cowan and R. W. Staehle : J. Electrochem. Soc., 118 (1971), 557.

(6)N. Sato : Bull. Japan Inst. Metals, 7 (1968), 617.

(7)R. Parsons : " Handbook of Electrochemical Constants", Butterworth Sci. Publ., London (1959).

(8)M. A. H. Lanyon and B. M. W. Trapnell : Proc. Roy. Soc., A227 (1955), 387.

(9)S. W. Feldberg, C. G. Enke and C. E. Bricker : J. Electrochem. Soc., 110 (1963), 826.

(10)U. R. Evans : Trans. Electrochem. Soc., 83 (1943), 335.

(11)U. R. Evans : "The Corrosion and Oxidation of Metals", Edward Arnold, London (1960), p.834.

(12)R. A. Robinson and R. H. Stokes : "Electrolyte Solutions", Butterworth Sci. Publ., London (1959).

(13)K. J. Vetter : Z. Elektrochem., 58 (1954), 230.

(14)N. Cabrera and N. Motto : Rep. Progr. Physics, 12 (1949), 163.

(15)N. Sato and M. Cohen : J. Electrochem Soc., 111 (1964), 512.

CHAPTER VII

Straining Electrode Behavior of Fe-Cr and Ni-Cr Alloys in High Temperature and High Pressure Borate Buffer Solution

7.1 Introduction

Stainless steels and high nickel alloys have been widely used in the high temperature and high pressure water environment of light water nuclear power plants[1),(2)]. Extensive studies have been performed on these commercial materials to understand and prevent corrosion failures including SCC, IGA, crevice corrosion and others[3),(4)]. It is commonly accepted that alloying elements, such as chromium, nickel and molybdenum play important roles to provide corrosion resistance to these alloys. However, few studies to understand the basic electrochemical influences of alloying elements have been performed in this environment.

In this chapter, in order to discuss the role of chromium in the initial process of repassivation, the results of the rapid straining electrode test are described for two series of binary alloys of Fe-Cr and Ni-Cr. The high temperature and high pressure borate buffer solution was used as the test environment, because iron and nickel showed no localized corrosion in this solution as discussed in Chapters V and VI.

The composition of passive film formed on the alloys in the same environment was analyzed by Auger electron spectroscopy, referring to their repassivation behavior.

7.2 Experimental

Materials used in the present study are Fe-xCr and Ni-xCr alloys (X = 3, 8, 18 and 22 in mass%) in addition to iron and nickel. Their chemical compositions are shown in Table 7-1. These materials were melted in a vacuum, cast and drawn to thin wire of 0.35 mm diameter. The wire specimens were degreased, then annealed in a vacuum, followed by water quench. The annealing temperature was 1073 K for nickel, iron and iron base alloys, and 1323 K for nickel base alloys. The electrolyte used was the borate buffer solution of 0.15 kmol·m^{-3} H_3BO_3 + 0.0375 kmol·m^{-3} $Na_2B_4O_7$, prepared with reagent grade chemicals and distilled water, and deaerated with high purity N_2 gas at room temperature before heating.

The straining electrode technique used here has been already described in Chapter II.

The specimen for Auger analysis was prepared as follows. 10 mm x 15 mm coupons were cut from a sheet of 2 mm thickness,

Table 7-1 Chemical composition of the specimen materials (mass%).

	C	N	Si	Mn	P	S	Al	Ni	Cr	Fe
Fe	0.001	0.0004	0.003	<0.001	0.002	0.001	<0.001	<0.001	-	bal.
Ni	0.028	-	0.066	0.38	0.003	0.004	-	bal.	0.001	0.09
3Cr-Fe	0.039	0.0069	0.32	0.31	0.003	0.002	0.15	<0.01	3.20	bal.
8Cr-Fe	0.028	0.0049	0.28	0.30	0.003	0.002	0.14	<0.01	8.23	bal.
18Cr-Fe	0.025	0.0064	0.30	0.30	0.003	0.002	0.17	<0.01	18.59	bal.
22Cr-Fe	0.025	0.0099	0.30	0.30	0.003	0.002	0.15	<0.01	22.48	bal.
3Cr-Ni	0.027	0.0019	0.27	0.30	0.002	0.001	0.14	bal.	3.26	0.17
8Cr-Ni	0.025	0.0037	0.27	0.30	0.002	0.001	0.15	bal.	7.66	0.01
18Cr-Ni	0.027	0.0045	0.30	0.31	0.002	0.001	0.13	bal.	18.07	<0.01
22Cr-Ni	0.024	0.0044	0.27	0.31	0.002	0.001	0.16	bal.	21.92	<0.01

which were obtained from the same materials used for the straining electrode test. The specimen surface was polished with SiC paper up to 1500 grid and finished with 0.3 μm alumina paste, then degreased with acetone and methanol in an ultrasonic bath. The passive films were formed at 523 K and at a constant potential of -0.2 V for 3.6k s in the borate buffer solution.

7.3 Results

7.3.1 Polarization curves

Polarization curves of the iron base alloys and the nickel base alloys in the borate buffer solution at 523 K are shown in Fig.7-1.

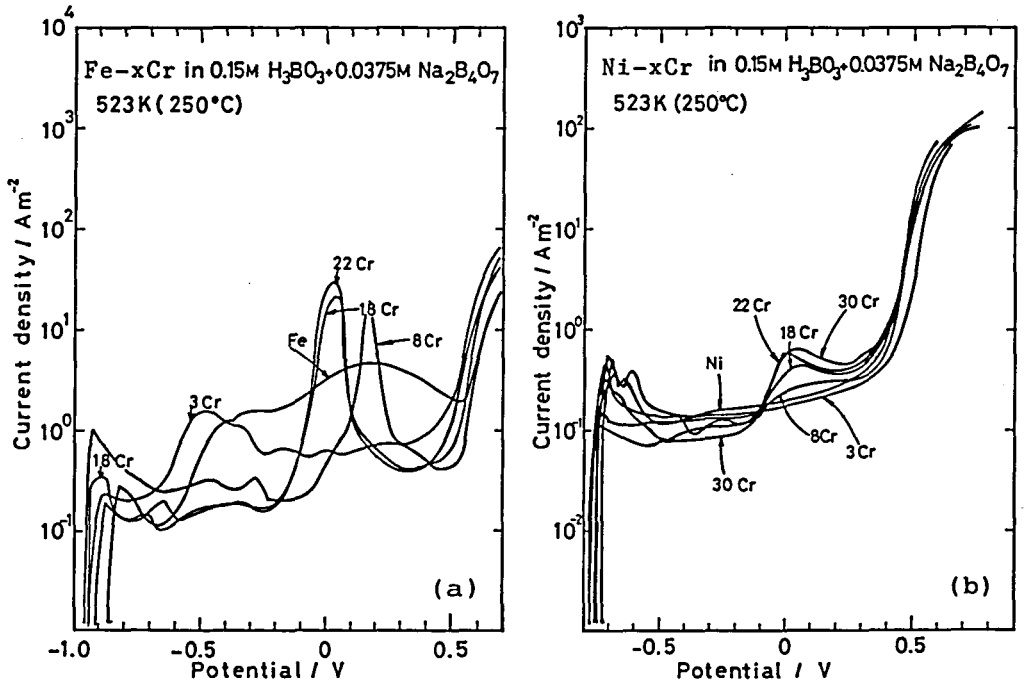

Fig.7-1 Polarization curves of (a)the Fe-Cr alloys and (b)the Ni-Cr alloys in borate buffer solution at 523 K.

For the iron base alloys, the current density in the passive region decreased with increasing chromium content. A small peak of current density was observed around -0.5 V for Fe-3Cr alloy. A similar peak was also recognized for iron. Another peak appeared at around 0 V for 8Cr, 18Cr and 22Cr-Fe alloys except for Fe and Fe-3Cr alloy. This peak is called the over passive peak. After the over passive peak, the secondary passive region was observed for every alloy.

The nickel base alloys showed more noble corrosion potentials than the iron base alloys. The over passive peak was also observed for the nickel base alloys around 0 V. Therefore, the passive potential region for the nickel alloys were narrower than that of the iron base alloys. The current density at the passive state for the Ni-Cr alloys did not depend so much on the chromium content, and was in the same order as that for Fe-18Cr and Fe-22Cr alloys. In contrast, the over passive peak current density for the Ni-Cr alloys depended clearly on the chromium content, but was fairly smaller than that of the Fe-Cr alloys.

Consequently, it can be concluded that the anodic polarization curves of Fe-Cr alloys clearly change with the chromium content. On the other hand, the Ni-Cr alloys showed almost the same polarization curves except for the over passive peak.

7.3.2 Straining electrode behavior of Fe-Cr alloys

Figure 7-2(a) shows the changes in the current density with time on the newly created surface of the Fe-Cr alloys at -0.2 V for 523 K. The current density, i, decayed following the power law :

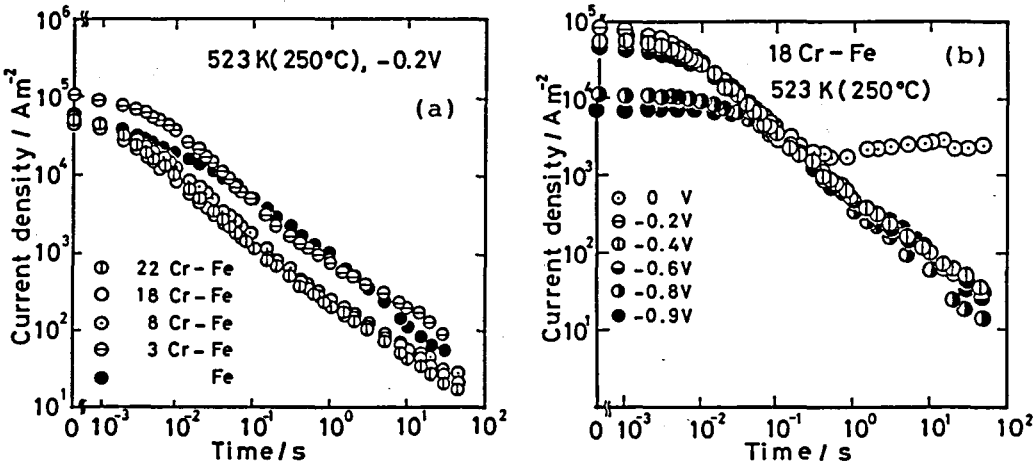

Fig.7-2 Changes in the anodic current density with time on the newly created surface of (a)the Fe-Cr alloys of various chromium contents at 523 K and -0.2 V, and (b)Fe-18Cr alloy at various potentials for 523 K.

$$i = at^{-n} \quad , \tag{7-1}$$

from few ms for about 3 decades. The power, n, was in the range of 0.8 ∿ 0.95 for Fe-Cr alloys and was larger than that of iron in the same environment, as described in Chapter V. The dependence of i on the chromium content, however, can not be seen clearly in the log i - log t plot. Figure 7-2(b) shows the changes in the current density of Fe-18Cr alloy for various potentials at 523 K. The current density on the newly created surface decayed following also the power law. i in the early stage for about 100 ms showed a positive potential dependence, but, in the later stage, the current density did not show any significant potential dependence. The current density, however, stopped decreasing at around 0.5 s and remained at a large value for few tens seconds at 0 V. This potential was in the over passive region observed in the polarization curves. This change

in the feature of the repassivation behavior in this potential region seems to be brought about by the oxidation of chromium, which was enriched in the initially formed film, from Cr^{3+} to Cr^{6+} as discussed later.

Figure 7-3 shows the decay in the current density on the newly created surface, i, with the increase in charge density, Q, for the Fe-Cr alloys at -0.2 V and 523 K. The alloy with the higher chromium content has a smaller current density at the same charge density Q except for Fe-3Cr alloy. On the other hand, Fe and Fe-3Cr alloy showed the larger current density than that of the other alloys at the same Q. In other words, the repassivation of Fe and Fe-3Cr alloy was slower than that of the other alloys. Similar log i to Q plots for Fe and Fe-Cr alloys were observed at 423, 473 and 553 K.

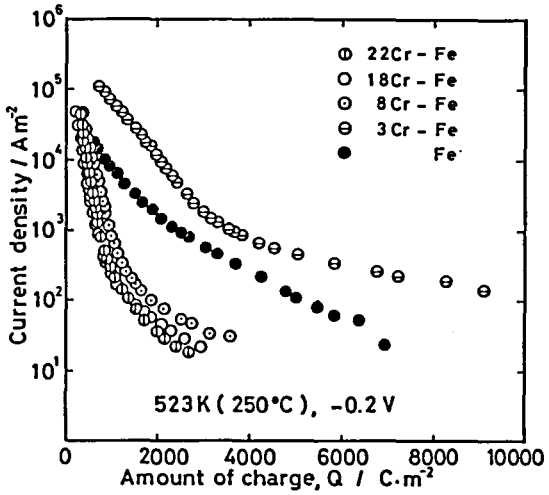

Fig.7-3 Changes in the current density, i, with increasing charge density, Q, for the Fe-Cr alloys of various chromium contents at 523 K and -0.2 V.

7.3.3 Straining electrode behavior of Ni-Cr alloys

Figures 7-4(a) and (b) show the change in i with time for the Ni-Cr alloys at 0.2 V for 523 K, and for Fe-18Cr alloy at various potentials for 523 K, respectively. A significant difference in log i vs log t curve was observed for nickel and the Ni-Cr alloys. Decays of the current density on both nickel and the Ni-Cr alloys followed the power law of Eq.(7-1), but the values of n were found to be 0.5 ∿ 0.8 for nickel and 0.8 ∿ 0.95 for the Ni-Cr alloys. The initial current density, i_0, for the Ni-Cr alloys was fairly larger than that for nickel, and increased with the increase in the chromium content.

The potential dependence of i vs t curve is shown in Fig.7-4(b). The current density increased with increasing applied potential. On the other hand, the value n in Eq.(7-1) did not depend on the applied potential. Namely, the repassivation rate of Ni-18Cr alloy was independent of potential, contrasting to that of Fe-18Cr alloy which depends on potential.

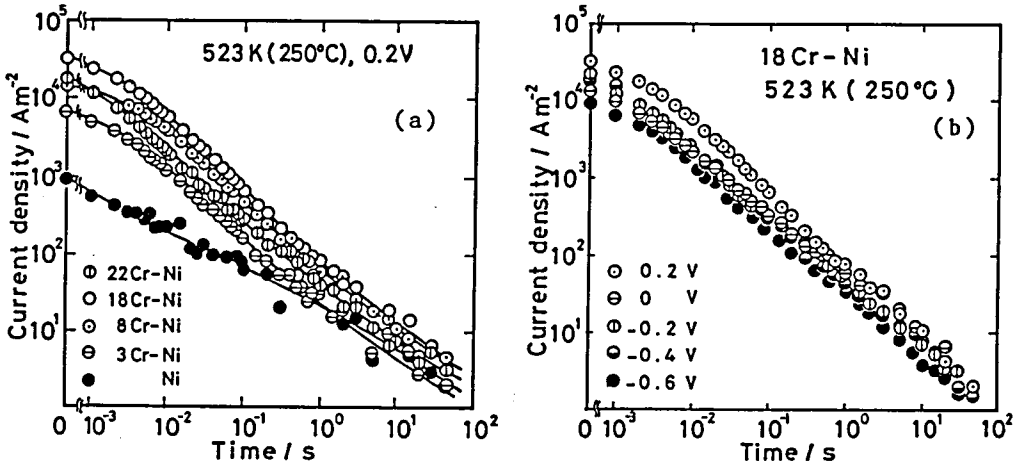

Fig.7-4 Changes in the anodic current density with time on the newly created surface of (a)the Ni-Cr alloys of various chromium contents at 523 K and 0.2 V, and (b)Ni-18Cr alloy at various potentials at 523 K.

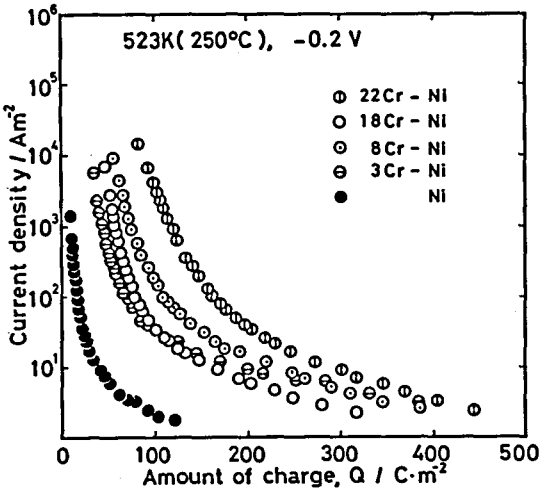

Fig.7-5 Changes in the current density, i , with increasing charge density, Q , for the Ni-Cr alloys of various chromium contents at 523 K and -0.2 V.

Relations between the current density and the charge density for the Ni-Cr alloys at -0.2 V and 523 K are shown in Fig.7-5. A similar repassivation behavior was observed for all the Ni-Cr alloys examined, although a larger current density during repassivation was observed for a higher chromium content alloy.

7.3.4 Auger electron spectroscopy

Auger analysis of the film was conducted for Fe-8C, Fe-18Cr, Ni-8Cr, Ni-18Cr and Ni-30Cr alloys. Figure 7-6 shows the depth profiles for (a) Fe-8Cr and (b) Fe-18Cr alloys. It is difficult to estimate the exact thickness of the film from sputtering time, because the sputtering rate for the oxide film formed on each alloy was not determined directly. The sputtering rate, however, was measured for SiO_2 which is indicated with the figures. The sputtering rate for Fe-8Cr was larger than that for Fe-18Cr. Furthermore, Fe-8Cr alloy needed a longer sputtering time for the peak to peak height of Fe

reaching a constant value, comparing to Fe-18Cr alloy. Therefore, it can be concluded that a fairly thicker film was formed on Fe-8Cr alloy than on Fe-18Cr alloy. This result was confirmed again by the fact that a brown interference color was observed for Fe-8Cr alloy specimen, while Fe-18Cr alloy showed only metallic luster with no color. Figure 7-7 shows depth profiles for (a) Ni-8Cr, (b) Ni-18Cr and (c) Ni-30Cr alloys. An identical sputtering rate was used for all Ni-Cr alloys. By comparing these three figures, it is readily seen that the

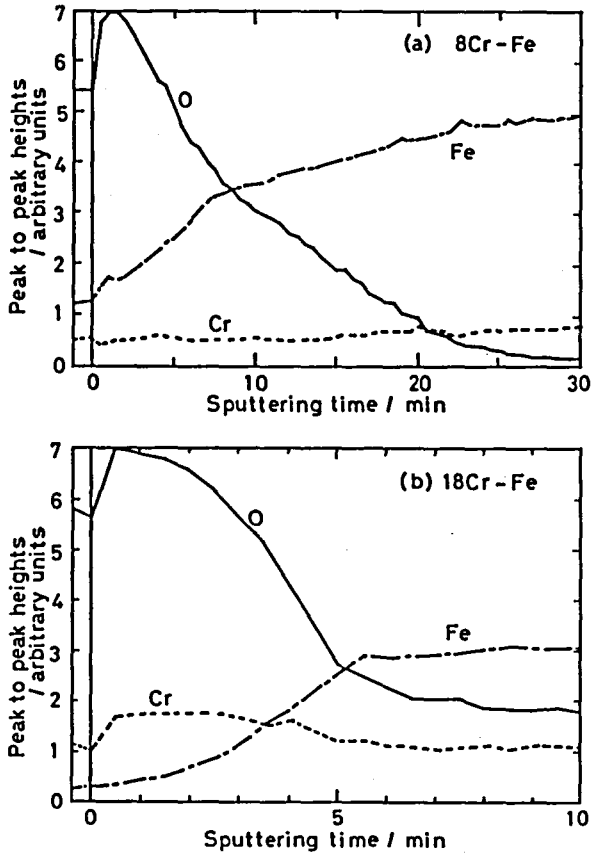

Fig.7-6 Auger depth profiles for the films formed on (a)Fe-8Cr and (b)Fe-18Cr alloys in the borate buffer solution at 523 K and -0.2 V for 3.6 ks. (Sputtering rate : (a) 231 Å/min as SiO_2, (b) 25 Å/min as SiO_2)

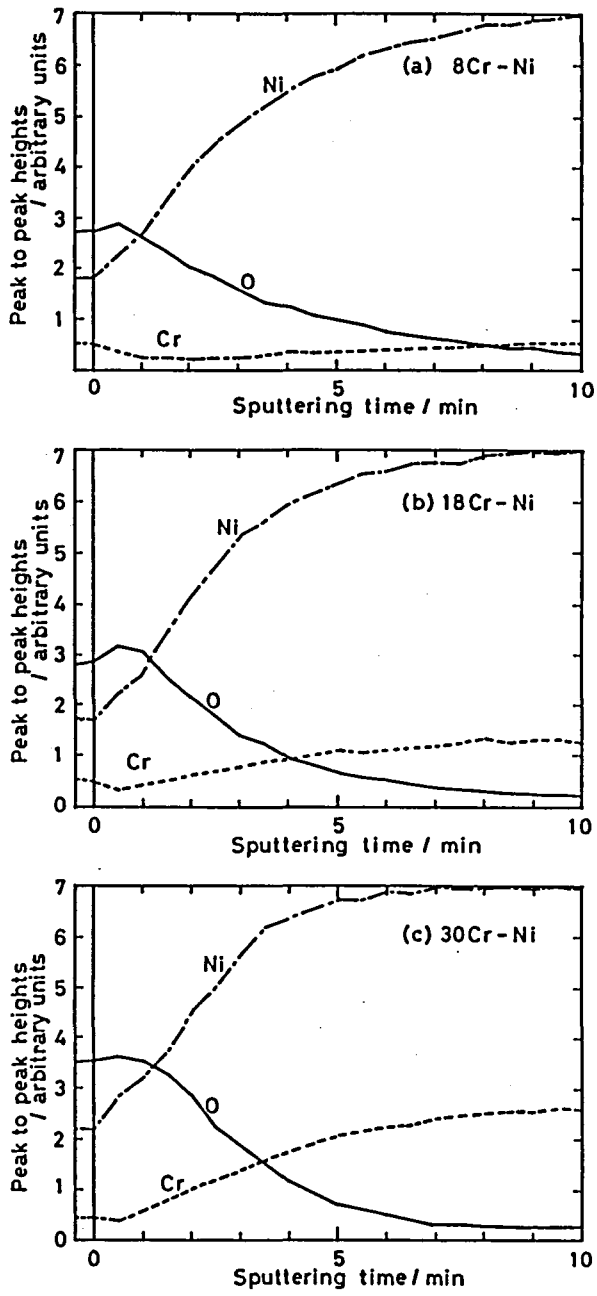

Fig.7-7 Auger depth profiles for the films formed on (a)Ni-8Cr, (b)Ni-18Cr and (c)Ni-30Cr alloys at 523 K and -0.2 V. (Sputtering rate : 231 A/min as SiO_2)

thicknesses of the films formed on the Ni-Cr alloys were almost the same. In addition, the surface of the Ni-Cr alloys showed the same metallic luster without interference color.

The peak to peak heights of chromium and iron in the depth profile for Fe-8Cr alloy simply increased with the sputtering time as shown in Fig.7-6(a). No enrichment of chromium in the film occurred, although a slight increase of the Cr/Fe ratio in the outer layer was observed. On the other hand, a significant enrichment of chromium could be clearly observed for Fe-18Cr alloy. The profile for Fe-18Cr alloy showed a maximum peak to peak height of chromium in the outer layer of the film, while the peak to peak height of iron in the outer layer increased with the depth. Thus, it can be concluded that the outer layer of the film for Fe-18Cr alloy consists mainly of chromium oxide.

The peak to peak height profiles for every Ni-Cr alloy show that a nearly constant Cr/Ni ratio was attained throughout the whole profile from outer surface to bulk alloy. Therefore, it is concluded that the Cr/Ni ratio in the film is nearly equivalent to that of the substrate alloy. It should be noted that no enrichment of chromium in the film occurs for the Ni-Cr alloys, contrasting to the remarkable chromium enrichment for Fe-18Cr alloy.

7.4 Discussion

7.4.1 Active dissolution on the newly created surface

The initial stage of repassivation showed that the anodic current tends to increase with increasing chromium content. It is reasonable to suppose that the initial current density is

proportional to the activity of metal or alloy for active dissolution.

The initial current density, i_0, is, however, not the true initial current density on the bare surface, because a short time of about 20 ms is always needed to give a constant amount of elongation. Thus, the film formation had already started even before the straining was stopped. Therefore, i_0 includes the influence of both active dissolution and the early stage of the film formation.

In the following discussion, a bare surface current density with no influence of film formation is estimated quantitatively by a numerical method, the outline of which is shown as follows.

It is assumed that the current density on a bare surface which emerges instantaneously follows an unknown function, C(t),

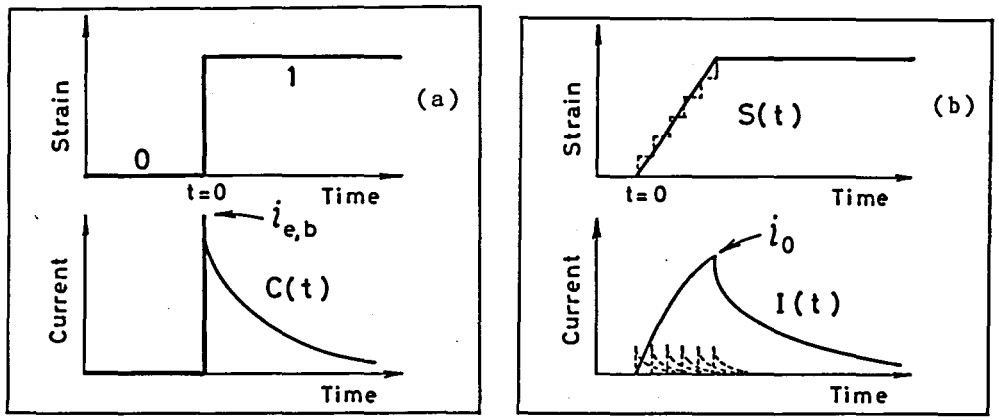

Fig.7-8 Schematic drawings of (a)strain which is introduced immediately and the change in the current, C(t), as a response of the input step function of the strain, and (b)actual changes in strain, S(t), and current, I(t), which is a convolution of C(t) and S(t).

as illustrated in Fig.7-8(a). In actual, the area of the bare surface changes with time during the limited time to reach a constant value, because an emergence of bare surface needs a limited time. Namely, the area of the bare surface can be described as a function of time, S(t). Thus, the observed change in current with time, I(t), is expressed as a convolution of S(t) and C(t), as shown in the following equation :

$$I(t) = \int_0^t C(\tau)\, S(t - \tau)\, d\tau \quad . \qquad (7\text{-}2)$$

In the present experiment, I(t) and S(t) can be expressed as series of data with the same intervals, because I(t) and S(t) are recorded as digital data measured at constant intervals. This relation is schematically shown in Fig.7-8(b). Therefore, if C(t) is also defined as a series of variables, the integral in Eq.(7-2) for a given t can be modified to a polynomial. Thus, Eq.(7-2) is also modified to a series of polynomials, namely, simultaneous equations. Thus, the unknown function C(t) can be obtained by solving these simultaneous equations. Consequently, the estimated bare surface current density, $i_{e,b}$, is given from the function C(t) thus obtained.

Figure 7-9 shows $i_{e,b}$ of the iron and nickel alloys at 523 K and -0.2 V as a function of chromium content. In this figure, i_0 is also plotted in broken lines. The initial current density, $i_{e,b}$, of both the Fe-Cr and the Ni-Cr alloys increases with increasing chromium content as similar as i_0. $i_{e,b}$, of iron is larger than that of nickel by about one order. It is also clearly shown that the addition of chromium to iron and nickel increases the initial current of both metals.

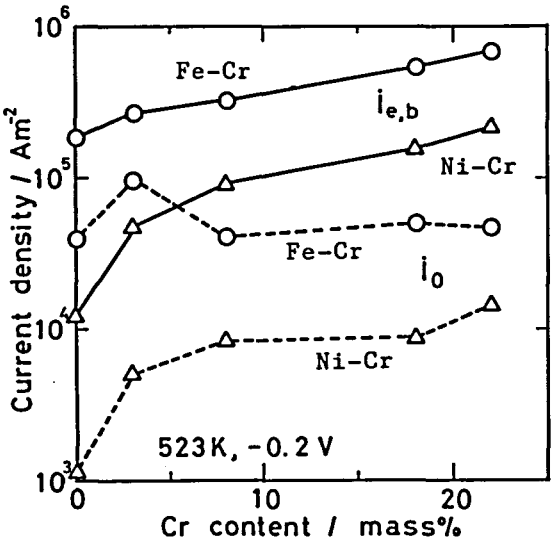

Fig.7-9 Effect of chromium content on the estimated bare surface current density, $i_{e,b}$, and the current density immediately after straining was stopped, i_0, for the Fe-Cr and the Ni-Cr alloys at 523 K for -0.2 V.

Therefore, it is concluded that the activity for dissolution of chromium is larger than that of iron and nickel. It is noticeable that the effect of chromium content on the current density is more pronounced for the Ni-Cr alloys than for the Fe-Cr alloys.

There have been few reports which dealt with the anodic dissolution of alloys thermodynamically. Bockris et al.[5] discussed on the partial dissolution current of constituent elements in a binary alloy considering the change in activation energy for dissolution of elements due to alloying. It is known that the reversible potential for an element in an alloy can be defined considering the change in activity of the element in the alloy. It has been reported that the partial dissolution current density of the element vs potential curves for the binary alloy obey the Tafel's relation. For this case, the decrease in

the logarithm of the partial anodic current density is proportional to the increase in the reversible potential[6]. In the present experiment, however, the detailed discussion on the contribution of chromium to the total dissolution current could not be given, because the observed current density could not be separated into each partial current.

On the other hand, Mueller[7] discussed on the derivation of the anodic polarization curves of alloy from its constituent elements, assuming that the alloy is a heterogeneous mixture of the single metallic components, and that each component contributes a fraction of the total current density :

$$I_a = I_x(A_x/A_a) + I_y(A_y/A_a) + I_z(A_z/A_a) + \cdots\cdots , \qquad (7\text{-}3)$$

where, I_a is current density of the alloy. I_x, I_y and I_z are current densities of the single metals of x, y and z. A_x, A_y and A_z are exposed areas of the metals, and A_a is the total exposed area of the alloy.

The dissolution current of $i_{e,b}$ at -0.2 V is controlled by diffusion, because $i_{e,b}$ showed no potential dependence above -0.2 V. Therefore, the dissolution rate is determined by the concentration of metal ion adjacent to the metal surface. It may be fairly accepted that the concentration of each element adjacent to the bare metal is proportional to the ratio in the substrate alloy at the very initial period after the emergence of bare surface. If there is no interaction between alloying elements, the relation presented in Eq.(7-3) holds. Thus, if the data exhibited in Fig.7-9 are plotted in $i_{e,b}$ vs the chromium content in normal scales, the extrapolation of the plots to 100 % chromium content provides I_{Cr}, i.e., the current density

on bare surface of chromium. The current density on the bare surface of chromium thus obtained is in the range between 10^6 and 10^7 Am^{-2}. This is more than one order larger than that of iron, and in turn the value for iron is about one order larger than that of nickel. Consequently, the contribution of chromium to the initial current density of alloys is apparently larger for the Ni-Cr alloys than for the Fe-Cr alloys as can be seen in Figs.7-2(a), 7-4(a) and 7-9.

In other words, most of current in the initial period of repassivation of the Fe-Cr and the Ni-Cr alloys derives from dissolution of chromium. This fact seems to be important for considering mechanisms of localized corrosion of the Fe-Cr-Ni alloys, because the larger dissolution rate is expected for the larger chromium content alloys at the very initial period after the film breakdown, in spite of their improved passivity. Moreover, the faster initial dissolution seems to enhance the localized corrosion.

7.4.2 Repassivation rate

As stated before, the chromium addition to Ni-Cr alloys simply increased the current density during repassivation but did not accelerate the repassivation. On the other hand, the addition of chromium to Fe-Cr alloys also increased the initial dissolution current, and more than 8 mass% chromium alloying increased the repassivation rate of Fe-Cr alloys. The addition of 3 mass% chromium, however, rather retarded the repassivation of Fe-Cr alloy, as shown in Fig.7-3.

The transient current density on the newly created surface should be discussed by considering not only the active dissolution rate but also the nature of film formed during the

repassivation. Informations about the nature of the passive film on these alloys are provided by the polarization curves and the results of Auger analysis.

The Auger electron analysis showed that the enrichment of chromium in the film occurs for Fe-18Cr alloy, whereas no enrichment of chromium occurs for Fe-8Cr alloy and all the Ni-Cr alloys. It is very likely that the change in polarization curves with chromium content corresponds to the chromium content in the passive film. The small current density in the passive region for Fe-18Cr and Fe-22Cr seems to be caused by the chromium enrichment in the passive film. It is also supposed that the large over passive peak current density is brought about by the oxidation of chromium from Cr^{3+} to Cr^{6+}, thus enriched in the film. On the other hand, the small contribution of chromium to decrease the passive current density and the small over passive peak for the Ni-Cr alloys compared with that of the Fe-Cr alloys are the result of no enrichment of chromium in the film for the Ni-Cr alloys.

It is considered that the enrichment of chromium in the steady state film corresponds to the change in the repassivation behavior observed in the straining electrode test, although the films analyzed by Auger were formed after a long time passivation compared with the short time of the straining electrode test.

The more rapid decrease in the current density, namely, the faster repassivation was always observed for the higher chromium content Fe-Cr alloys as shown in Fig.7-3. It is reasonably assumed that the chromium enriched passive film depresses effectively the dissolution current, although the larger anodic current flows at the very initial period owing to the higher activity of chromium. On the other hand, the small addition of

chromium also enhances the initial dissolution. However, it does not suppress effectively the repassivation process, because the chromium content in the alloy is not sufficient to form chromium enriched passive film. Consequently, the repassivation current of Fe-3Cr alloy was larger than that of the other Fe-Cr alloys. The enrichment of chromium, however, did not occur for Fe-8Cr, as shown in Fig.7-6, but the enhancement of the repassivation was observed for this alloy. It seems that the structure of the newly created surface was different from the surface prepared for Auger specimen. Therefore, the repassivation behavior in the straining electrode did not correspond to the film composition for the Fe-Cr alloy of the intermediate chromium content.

In the case of the Ni-Cr alloys, the chromium addition increases significantly the initial current, because the dissolution activity of chromium is fairly larger than that of nickel as mentioned before. However, changes in the current density with time or charge density are quite similar for all the Ni-Cr alloys, regardless of the chromium content. In other words, chromium addition has no effect on the repassivation rate for the Ni-Cr alloys, corresponding to no enrichment of chromium in the passive film formed on the Ni-Cr alloys.

7.5 Conclusions

The initial stage of repassivation process of Fe-Cr and Ni-Cr alloys of various chromium contents was investigated in the high temperature and high pressure borate buffer solution. Moreover, the composition of the passive film formed on these alloys was analyzed by Auger electron spectroscopy.

(1) The initial current on the newly created surface increased with increasing chromium content for both the Fe-Cr and Ni-Cr alloys. The chromium addition of more than 8 mass% accelerated the repassivation of the Fe-Cr alloys, but the addition of 3 mass% chromium rather retarded it. On the other hand, the chromium addition to the Ni-Cr alloys simply increased the current density during repassivation, although it did not accelerate the repassivation.

(2) A bare surface current density with no influence of film formation was estimated by a numerical method. It was concluded that the bare surface current density of chromium was more than one order larger than that of iron. The bare surface current density of iron was in turn also about one order larger than that of nickel.

(3) Auger analysis showed that chromium was enriched in the passive film of Fe-18Cr alloy, while chromium enrichment did not take place for the Fe-Cr alloy of small chromium content and all the Ni-Cr alloys examined.

(4) The results of straining electrode tests and the Auger analysis showed that the acceleration of repassivation was always associated with the chromium enrichment in the passive film.

REFERENCES

(1)S. J. Green and J. Peter N. Paine : Nucl. Tech., 55 (1981), 10.

(2)Ph. Berge and J. R. Donati : Nucl. Tech., 55 (1981), 88.

(3)S. Szklarska-Smialowska and G. Cragnolino : Corrosion, 36 (1980), 653.

(4)D. Van Rooyen : Corrosion, 31 (1975), 327.

(5)J. O'M. Bockris, B. T. Rubin, A. Despic and B. Lovrecek : Electrochimica Acta, 17 (1972), 973.

(6)M. Okuyama : Denki-Kagaku, 50 (1982), 320.

(7)W. A. Mueller : Corrosion, 18 (1962), 74.

CHAPTER VIII

Straining Electrode Behavior of Fe-Cr-Ni Alloys in High Temperature and High Pressure Borate Buffer Solution

8.1 Introduction

In the previous chapters, the repassivation behavior on the newly created surface of iron and nickel, and also that of the Fe-Cr and the Ni-Cr alloys have been investigated. The commercial materials that are used actually in the high temperature and high pressure water environment are mainly Fe-Cr-Ni ternary alloys. This chapter deals with the repassivation behavior of Fe-Cr-Ni alloys, whose chemical compositions are similar to that of the commercial alloys. In the previous chapter, it has been revealed that the Fe-Cr alloys and the Ni-Cr alloys show quite different repassivation behavior. In this chapter, in order to discuss the role of iron and nickel, the repassivation behavior of Fe-Cr-Ni alloys which contain various amounts of iron and nickel with a constant amount of chromium of 18 mass% were analyzed. Auger analysis of the films formed on these alloys was also conducted in order to compare the repassivation behavior of these alloys with the composition of the film.

8.2 Experimental

The materials used in the present experiment were 75Ni-18Cr-7Fe, 33Ni-18Cr-49Fe and 8Ni-18Cr-74Fe alloys, whose chemical composition are shown in Table 8-1. The former two alloys were prepared in the same way for the Ni-Cr alloys described in the

Table 8-1 Chemical composition of the specimen alloys (mass%).

	C	N	Si	Mn	P	S	Al	Ni	Cr	Fe
75Ni-18Cr- 7Fe	0.028	0.0037	0.30	0.30	0.002	0.001	0.16	bal.	17.74	6.99
33Ni-18Cr-49Fe	0.026	0.0062	0.30	0.30	0.002	0.002	0.16	bal.	17.88	45.33
SUS304	0.073	0.038	0.51	0.80	0.034	0.002	-	8.47	18.29	bal.

previous chapter. 8Ni-18Cr-74Fe alloy is commercial SUS304 stainless steel. The former two alloys were prepared in order to simulate the composition of commercial alloys of Alloy 600 and Alloy 800, respectively. These high nickel alloys are widely used as steam generator (SG) tubing materials in PWR.

The straining electrode test procedures were the same as

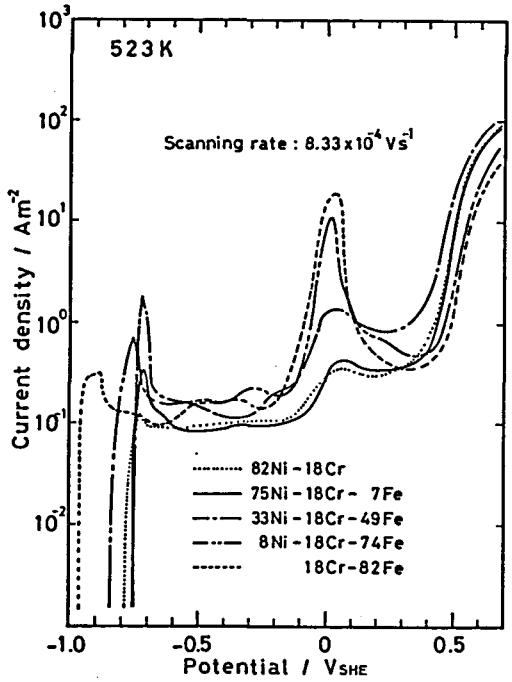

Fig.8-1 Polarization curves of the Fe-18Cr-Ni alloys in borate buffer solution at 523 K.

described in the early chapters. The electrolyte used was the borate buffer solution.

The specimens used for Auger analysis were prepared also in the same way as described in Chapter VII.

8.3 .Results

8.3.1 Polarization curves

Polarization curves of 75Ni-18Cr-7Fe, 33Ni-18Cr-49Fe and 8Ni-18Cr-74Fe (SUS304) alloys measured in the borate buffer solution at 523 K are shown in Fig.8-1, in which polarization curves of Fe-18Cr and Ni-18Cr alloys already shown in the previous chapter are also presented. The corrosion potential, $E_{Corr.}$ shifted to less noble value with increasing iron content. $E_{Corr.}$ of Fe-18Cr alloy was fairly less noble than that of the other alloys. On the other hand, these five alloys showed the same over passive peak potentials at around 0 V. Therefore, it is concluded that the Fe-Cr-Ni alloy system, including binary alloys of the Fe-Cr and Ni-Cr alloys, shows a constant over passive peak potential.

The current density in the passive potential region increased with the increase in the iron content, although its dependence was not so large. On the other hand, the over passive peak current density clearly depended on the Fe/Ni ratio. Namely, the current density of the over passive peak increased with increasing iron content.

8.3.2 Auger electron spectroscopy

Figure 8-2 shows the differential Auger electron spectrum of the anodic film formed on 33Ni-18Cr-49Fe alloy in the borate

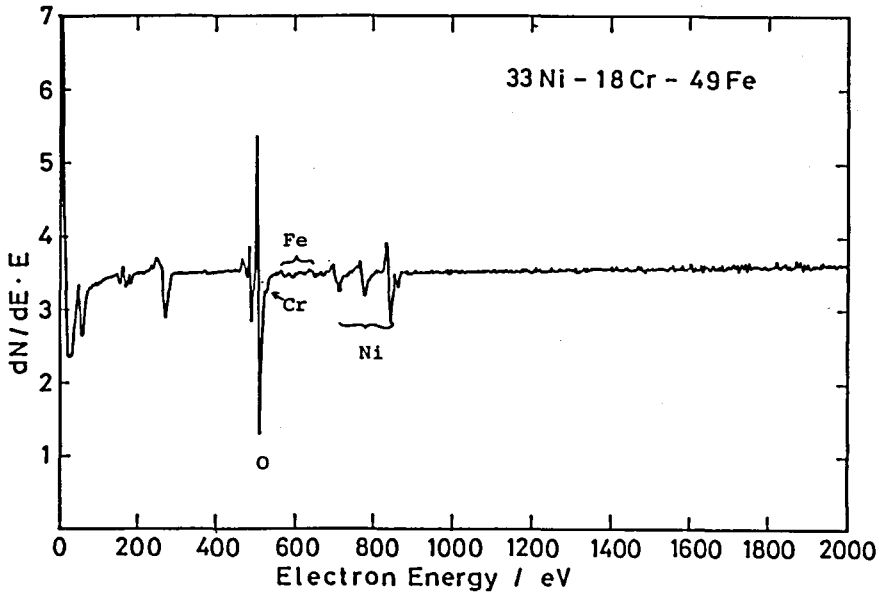

Fig.8-2 Auger differential spectrum of the film formed on 33Ni-18Cr-49Fe alloy, before sputtering.

buffer solution. The depth profiles of film formed on 75Ni-18Cr-7Fe, 33Ni-18Cr-49Fe and 8Ni-18Cr-74Fe alloys are shown in Fig.8-3 (a), (b) and (c), respectively. These profiles were obtained with an identical sputtering rate. Thus, the thickness of the films can be compared directly from these profiles. There seems to be no significant difference in thickness among these three alloys.

The depth profile of 75Ni-18Cr-7Fe alloy shows that the peak to peak heights of Ni, Cr and Fe increase from outer surface to inner layer. The Ni/Cr/Fe ratio is almost constant throughout the profile except for a small increase of chromium near the surface. In other words, the cation ratio in the film is almost the same as that of the substrate alloy. Almost constant Cr/Ni ratio throughout the depth is also observed for 33Ni-18Cr-49Fe alloy. On the other hand, the ratio of Fe to Cr and Ni at the

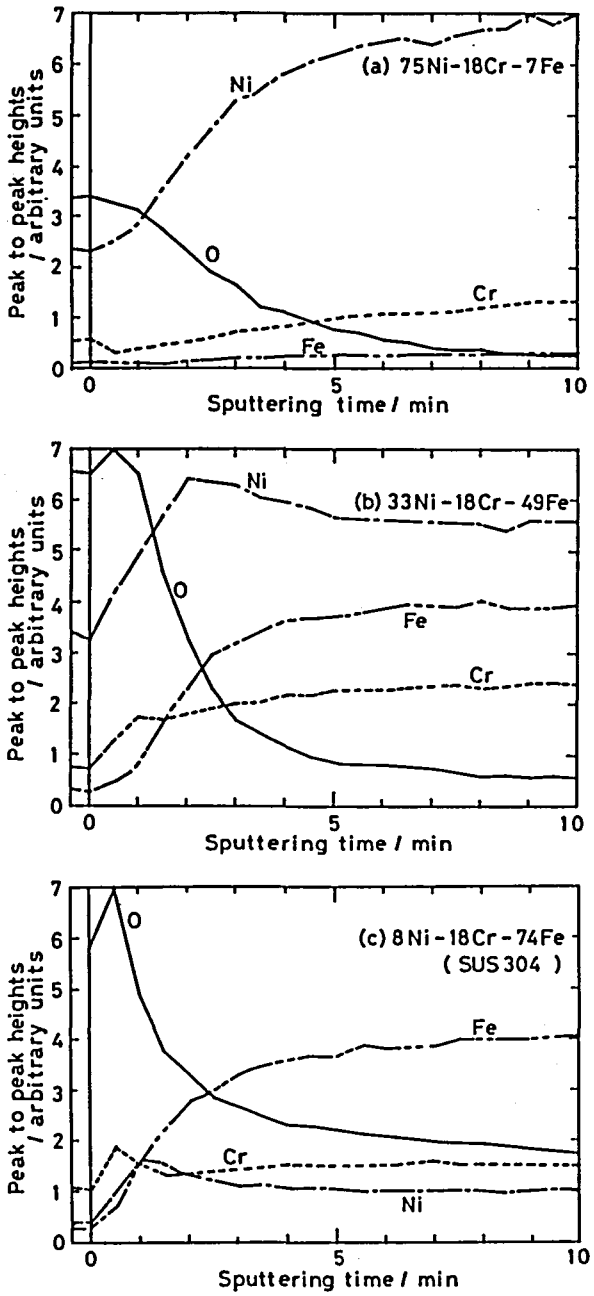

Fig.8-3 Auger depth profiles for the films formed on (a)75Ni-18Cr-7Fe, (b)33Ni-18Cr-49Fe and (c)8Ni-18Cr-74Fe 74Fe alloys at 523 K and -0.2 V for 3.6 ks. (Sputtering rate : 231 Å/min as SiO_2)

surface is fairly smaller than that at the substrate. In other words, the height of Fe at the surface is smaller than that of Cr, whereas the height of Fe is larger than that of Cr in the substrate in accordance with the alloy composition. Thus, a depletion of iron in the film was surely occurred. In the case of 8Ni-18Cr-74Fe alloy, Fe in the film decreased distinctly. From these facts, it can be easily concluded that the most part of cation in the film is chromium.

8.3.3 Straining electrode behavior

The changes in current density on the newly created surface of the alloys at -0.2 V for 523 K, and at -0.05 V for 423 K are shown in Figs.8-4(a) and (b), respectively. The current density decayed with time following the power law, the power n being about 0.8 ∿ 0.95. These figures clearly show that the changes in the current density with time were very similar for 82Ni-18Cr, 75Ni-18Cr-7Fe, 33Ni-18Cr-49Fe and 8Ni-18Cr-74Fe alloys

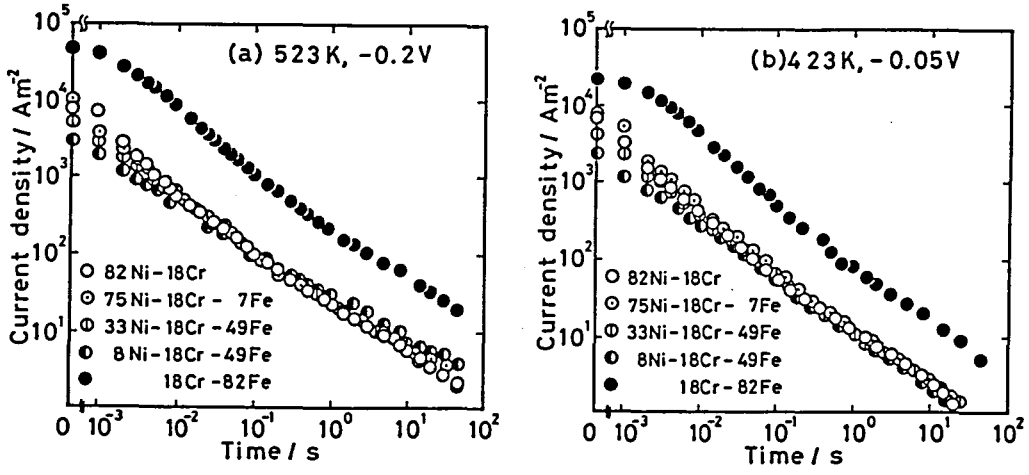

Fig.8-4 Changes in the anodic current density with time on the newly created surface of the Fe-18Cr-Ni alloys at (a)523K and -0.2 V, and at (b)423 K and -0.05 V.

to one another, except for the initial period less than 10 ms. The larger current density flowed for the larger nickel contents alloys during this initial period. On the other hand, the transient current density for 82Fe-18Cr was fairly larger than that of the other alloys.

The changes in the current density on the newly created surface with increasing charge density, Q, at -0.2 V for 523 K are shown in Fig.8-5. The difference in the changes of the current density in the initial period can be observed more apparently compared with the log i vs log t curves. It is obviously recognized that the larger charge density was needed for decay of current density for the larger nickel content alloy. However, the larger current density flowed for the larger iron content alloy in the later period. On the other hand, the change in current density with Q for 18Cr-82Fe alloy was quite different from that for the others.

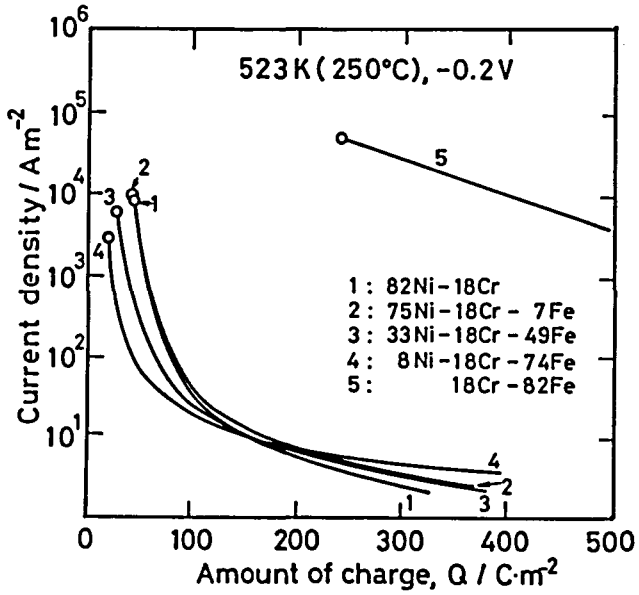

Fig.8-5 Changes in the current density with increasing charge density, Q , for the Fe-18Cr-Ni alloys at 523 K and -0.2 V.

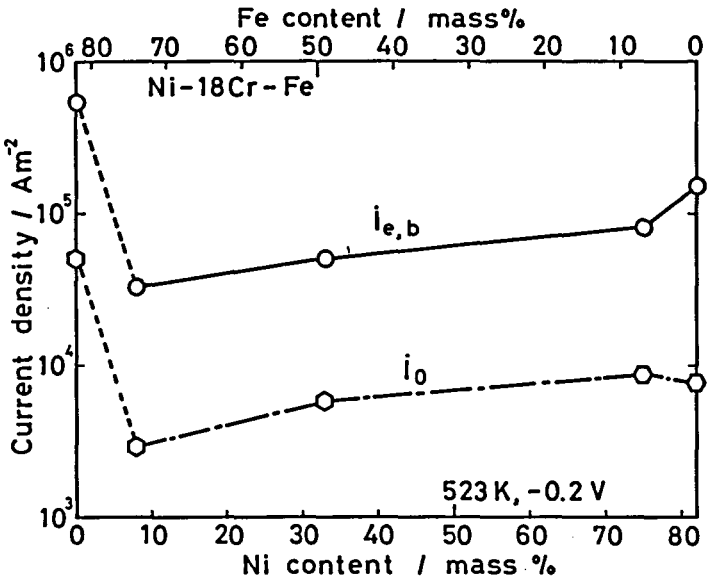

Fig.8-6 Effect of the alloy composition on the estimated bare surface current density, $i_{e,b}$, and on the current density immediately after straining was stopped, i_0, for the Fe-18Cr-Ni alloys.

As already discussed in the previous chapters, the observed initial current density is not the true bare surface current density. The true bare surface current density was estimated in the same way introduced in Chapter VII. Figure 8-6 shows the current density, $i_{e,b}$, calculated for Fe-18Cr-Ni alloys at -0.2 V for 523 K. The current density immediately after straining was stopped, i_0, is also plotted in a broken line. It is shown that $i_{e,b}$ slightly increased with the increase in the nickel content above 8 mass% Ni. On the other hand, 0 mass% Ni, namely, Fe-18Cr alloy showed fairly larger $i_{e,b}$ than that of the other alloys.

8.4 Discussion

8.4.1 The initial current density

As discussed in Chapter VII, i_0 or $i_{e,b}$ for the Fe-Cr alloys

was larger than that for Ni-Cr alloys. Therefore, it is expected that the initial current increases with increasing Fe/Ni ratio for the Fe-18Cr-Ni alloys. However, $i_{e,b}$ increased slightly with increasing nickel content except for Fe-18Cr alloy, contrary to the expectation. If the initial current derives mostly from the dissolution of chromium, the initial currents for alloys of the same chromium content have to be almost equal. Then, it is necessary to consider another parameter for the initial dissolution. It is likely that the dissolution on a bare surface starts at active sites which include edges of plane, kinks and other defects. Thus, the initial current is proportional to the number of these active sites and the chromium content. Therefore, it is important to consider the structure of defects on the newly created surface. In the case of the straining electrode test, since the newly created surface emerges owing to the formation of slip steps, the edges of slip step act as active sites for dissolution. The number of slip step is directly related to the dislocation density and its structure[1),(2)]. An illustration of the structure of the slip step and the active sites on it[3)] is presented in Fig.8-7.

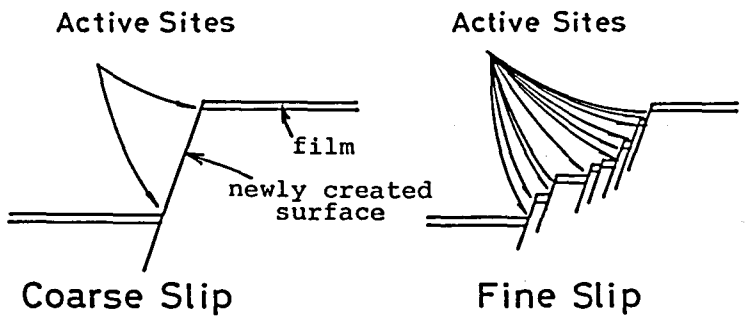

Fig.8-7 Schematic sketch of two kinds of slip steps.

Among the Fe-Cr-Ni alloys examined, only Fe-18Cr alloy was ferritic phase, the others being austenitic phase. It is known that ferritic phase (b.c.c.) has many slip systems compared with that of austenitic phase (f.c.c.). Therefore, ferritic alloy forms finer slip steps than an austenitic alloy. Thus, the more dissolution sites emerged for the ferritic alloys than for the austenitic alloys at the same elongation. Consequently, Fe-18Cr alloy showed the larger initial current than the other austenitic Fe-18Cr-Ni alloys.

Assuming that the initial current is proportional to the chromium content and the number of slip step emerged at a given elongation, the initial current for the austenitic Fe-18Cr-Ni alloys of various nickel contents has to depend on the number of slip step, because the chromium content in the alloys was constant. Stacking fault affects the structure of dislocation for austenitic alloys[1]. It is known that high stacking fault energy of pure nickel is reduced by alloying of iron and chromium[4]. Dislocations introduced by the deformation for the alloys of low stacking fault energy are widely extended and exist as piled up groups, namely, coplanar arrays[5],[6]. Thus, dislocations tend to remain in their slip steps to produce coarse slip steps. The alloys with high stacking fault energy, on the other hand, exhibit tangles or cell boundaries of dislocations to form many slip planes. Thus, a deformation produces many or fine slip steps. The stacking fault energy of the Fe-Cr-Ni alloys of about 18 mass% chromium has been reported to increase with increasing nickel content[4]. Figure 8-8 shows the variation of the stacking fault energy of Fe-Cr-Ni alloys reported by some authors[4]. Consequently, the alloy of the larger Ni/Fe ratio exhibits the higher stacking fault energy to produce the finer

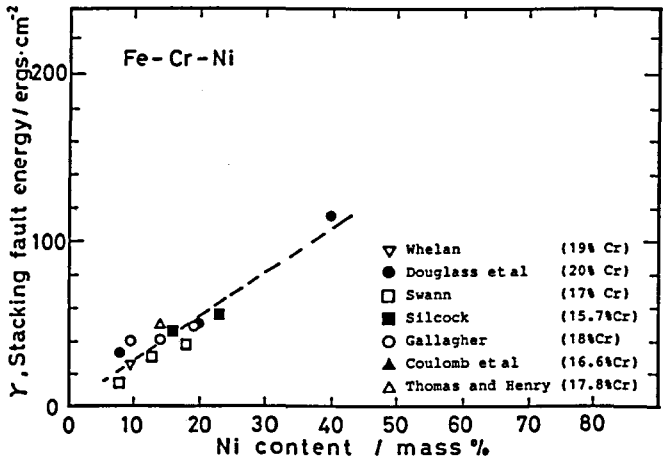

Fig.8-8 Variation of the stacking fault energy in Fe-Cr-Ni alloys[4].

slip steps, resulting in the formation of a larger number of active sites for dissolution. Therefore, the initial current on the bare surface of the austenitic Fe-18Cr-Ni alloy increases with increasing nickel content as a result of the change in the dislocation structure.

8.4.2 Film formation behavior

The change of current density in the later period showed a small difference among the Fe-18Cr-Ni alloys except for Fe-18Cr alloy. That is, the larger current density tends to flow for the larger iron content alloys contrary to the initial period, although the difference is not so large, as shown in Fig.8-5. The newly created surface seems to be covered uniformly with the passive film in the later period. Then, it is supposed that the dissolution activity of the substrate alloy determines the repassivation current in the later period, regardless of the number of active site formed by the deformation. The larger current density was actually observed in the passive potential

range for the higher iron content alloy in the polarization curve which represents the dissolution rate on the film-covered surface. Thus, it seems that the larger iron content alloy shows the higher dissolution activity.

The ferritic 18Cr-Fe alloy, however, showed the fairly larger current density than the other alloys not only in the initial period but also in the later period until which the nucleation and two dimensional extension of the film has been already completed. Therefore, the difference in the repassivation behavior between austenitic alloy and the ferritic alloy can not be explained only by the difference in the structure of the newly created surface. Thus, the difference in the property of film must be considered.

As discussed in Chapter VII, the cation ratio in the film on the Ni-Cr alloys is almost the same as that of the substrate alloys. On the other hand, enrichment of chromium in the film occurs for the chromium rich Fe-Cr alloys. The Cr/Ni ratios in the films on the Fe-18Cr-Ni alloys examined are approximately constant throughout the depth. Namely, the Cr/Ni ratio in the film is roughly the same as that for the substrate alloys. On the other hand, the Fe/Cr or Fe/Ni ratio in the film on the Fe-18Cr-Ni alloys are smaller than that of the substrate alloys. Thus, if the iron content in an alloy is large, the proportion of chromium and nickel in the film becomes relatively larger than that of the substrate alloy. Therefore, the larger iron content alloy forms the more chromium enriched film, because the iron rich alloy contains relatively a small content of nickel. In fact, the passive film formed on SUS304 steel consists of chromium oxide to a large extent as already shown in Fig.8-3(c). Therefore, it is concluded that the selective dissolution of iron

occurs during the repassivation process. In other words, the selective dissolution leads to the lower deposition ratio of iron as the film than that of chromium and nickel. On the other hand, the deposition ratio of chromium and nickel seems to be approximately equal, because no change of the Cr/Ni ratio in the film was observed.

The difference in the film composition shows no noticeable effect on the changes in the current density with time for Fe-18Cr-Ni alloys except for Fe-18Cr alloy in a short period of about 50 s in the straining electrode test. Alloying elements such as nickel and chromium in the iron base alloys are enriched in the film as a result of the selective dissolution of iron as discussed above. Thus, a small addition of nickel into Cr-Fe alloy is supposed to change the property of the film. Then, this is considered to be one of the main factors which result in the difference in the repassivation behavior between 18Cr-Fe alloy and the other Ni-18Cr-Fe alloys.

8.4.3 Consideration of SCC susceptibility

There was no noticeable difference in polarization curves between Fe-18Cr alloy and the other Fe-Cr-Ni alloys. This fact suggests that the character of film formed on the newly created surface emerged by straining is different from that formed on the polished surface of polarization specimen. Thus, the deformation, namely straining, has affected not only the structure of the newly created surface but also the property of the film.

It is considered that SCC of metals and alloys in a given environment is likely to occur under the following condition[7] : the initial dissolution rate on the newly created surface emerged

by a deformation is larger and the repassivation due to film formation is more rapid. Such condition seems to be attained for the high nickel austenitic alloys, because the larger initial current on the newly created surface was observed for the higher nickel content alloy and the repassivation rate of the austenitic alloy is fairly larger than that of ferritic Fe-18Cr alloy.

It has been discussed that ferritic stainless steels are immune to SCC in such environments as chloride solutions[8],[9], while austenitic stainless steels in the same environments are highly susceptible to SCC[7]. However, austenitic 13Cr-8Mn alloy is known to be resistant to SCC[10]. On the other hand, ferritic stainless steels which contains a small amount of nickel are reported to show SCC susceptibility[11]. These facts suggest that the difference in the structure is not the only factor determining the SCC susceptibility. Thus, it is thought that not only the crystal structure but also the chemical properties for the dissolution and the film formation of alloys are important for considering the susceptibility to SCC. It should be pointed out that a small addition of nickel to the iron base alloys changes the both factors and affects the SCC susceptibility.

8.5 Conclusions

The repassivation behavior on the newly created surface of the Fe-18Cr-Ni alloys of various Fe/Ni ratio with the constant chromium content was investigated in the high temperature and high pressure borate buffer solution. The Auger electron analysis of the films formed on these alloys was also conducted.

(1) The difference in the alloy structure remarkably

affected the initial period of repassivation behavior on the newly created surface.

(2) Fe-18Cr alloy showed a fairly larger current density on the newly created surface compared with the austenitic Fe-18Cr-Ni alloys. On the other hand, the austenitic alloys showed similar changes in the current density in spite of a large difference in the Fe/Ni ratio.

(3) The initial current on the newly created surface of the austenitic Ni-18Cr-Fe alloys increased with the increase in the nickel content. The change in structure of slip step affects the initial current. The stacking fault energy increases with increasing nickel content to form the finer slip steps, which give many sites for active dissolution. Therefore, the initial current density increased with increasing nickel content.

(4) The chromium content in the film increased with increasing iron content. The selective dissolution of iron was thought to be the reason for the chromium enrichment.

(5) The higher SCC susceptibility is likely to be attained for the higher nickel content austenitic Fe-Cr-Ni alloys.

REFERENCES

(1)P. R. Swann and J. D. Embury : "High Strength Materials", Wiley and Sons, New York (1965), p.327.

(2)A. W. Thompson and I. M. Bernstein : "Advances in Corrosion Science and Technology", Plenum (1980), Vol.7, p.53.

(3)T. Shibata and R. W. Staehle : Proc. Int. Cong. on Metall. Corros., (1974), p.487.

(4)P. C. J. Gallagher : Metall. Trans., 1 (1962), 343.

(5)P. R. Swann : Corrosion, 19 (1963), 102.

(6)D. L. Douglass, G. Thomas and W. R. Roser : Corrosion, 20 (1964), 15.

(7)R. M. Latanision and R. W. Staehle : "Fundamental Aspects of Stress Corrosion Cracking", NACE (1969), 214.

(8)R. T. Newberg and H. H. Uhlig : J. Electrochem. Soc., 119 (1972), 981.

(9)A. P. Bond and H. J. Dundas : Corrosion, 24 (1968), 344.

(10)M. A. Stricker : Stainless Steel, 77 (1977), 1.

(11)R. F. Steigelwald, A. P. Bond, H. J. Dundas and E. A. Lizlov : Corrosion, 33 (1977), 279.

CHAPTER IX

SUMMARY

The dissolution and the subsequent film formation of iron, nickel and their chromium alloys were investigated by a rapid straining electrode technique, in order to obtain the basic electrochemical information of iron and nickel base alloys in the high temperature and high pressure water environments.

In Chapter I, the historical background of corrosion failures in the high temperature and high pressure water environments was described and the aim of this work was stated.

The history, the principle and the experimental apparatus of the straining electrode technique were described in Chapter II. A thin wire electrode was elongated rapidly to yield a newly created surface at a constant potential. The anodic current increased rapidly to a maximum, then decayed. The change in current density on the newly created surface with time was analyzed at various potentials and temperatures up to 573 K.

The straining electrode behavior of iron in a sodium sulphate solution was analyzed in Chapter III. The anodic current density decayed following a power law : $i = at^{-n}$, except for the initial period of 0.01 $\sim$ 0.1 s. A thick magnetite layer formed in the passive potential region above 503 K, its growth following a parabolic law. The rate constant for the growth showed a negative temperature dependence. It was concluded that a more compact film was formed to suppress diffusion of reaction species through the film at a higher temperature. Iron, however, showed no passive state and dissolved away rapidly in a temperature range of 423 $\sim$ 463 K. On the basis of the active dissolution rate and the repassivation rate on the newly created

surface a favorable condition to assist SCC of iron could be attained under the condition of 503 K and +0.3 V in the 0.1 kmol·m^{-3} Na_2SO_4.

The rapid straining electrode technique was applied to investigate the initial process of anodic dissolution and the subsequent film formation on nickel in solutions containing sulphate ion in Chapter IV. Two types of the changes in the anodic current were found for the newly created surface. The first showed a rapid decay and was called the repassivation type. The anodic current, however, showed no rapid decay and sometimes increased gradually in the second type. The second was called the breakdown type because the passive film was broken locally, showing no repassivation. The breakdown was observed at potentials more noble than a critical potential, which was called the breakdown potential. The breakdown potential shifted more noble with the increase in temperature above 403 K, but the breakdown was not observed below 393 K. Thus, it was found that there existed an unstable temperature range for the passivity of nickel in the sulphate ion containing solutions around 400 $\sim$ 450 K. It was considered that the sulphate ion promoted the formation of non-protective $Ni(OH)_2$, prior to the passive film formation. Thus, the dissolution of nickel continued, leading to the breakdown.

Based on the results of previous two chapters that SO_4^{2-} ion caused the breakdown of passivity of iron and nickel, a borate buffer solution was used as the electrolyte in the experiments described in the following chapters.

In Chapter V, the repassivation behavior of iron was investigated in the borate buffer solution. The repassivation seemed to be controlled by diffusion in aqueous solution, but

proceeded more rapidly than expected from the parabolic rate low. Fe^{2+} ion diffused in aqueous phase contained in pores or other defects in the oxide layer. The rapid repassivation rate was attained owing to the decrease in the number and size of these diffusion paths before the growth of magnetite layer reached to a steady state. The repassivation behavior was divided into two groups according to the applied potential, the critical potential being around -0.5 V at 523 K. The slower repassivation rate was observed at the more noble potentials than the critical potential. The change in the reaction product from Fe_3O_4 to Fe_2O_3 seemed to occur at the critical potential. Based on the experimental results, a favorable condition for SCC of the iron base alloys was discussed.

The repassivation process of nickel in the borate buffer solution was investigated in Chapter VI. The repassivation process consisted of early and later stages. In the early stage, the newly created surface was covered with monolayer of oxide film. The rate of this process followed a direct logarithmic law, showing neither potential nor temperature dependence. The mechanism of this stage was explained by a mutually-blocking pore model proposed by Evans. In the later stage, the passive film grew following a parabolic law with the rate constant depending on both temperature and potential. The rate of this process was concluded to be determined by migration and diffusion of Ni^{2+} ion in liquid phase under the potential and the concentration gradient through pores and other defects contained in the passive film.

In order to discuss the role of chromium for the passivity of Fe-Cr and Ni-Cr alloys, the initial process of repassivation on the newly created surface was analyzed, and also the depth

profile of composition of the film formed on these alloys were examined by Auger electron spectroscopy in Chapter VII. It was observed that chromium addition simply increased the initial current density on the bare surface of both the Fe-Cr and the Ni-Cr alloys. The repassivation of the Fe-Cr alloys was enhanced by the chromium addition of more than 8 mass%, but was rather retarded by 3 mass% chromium. On the other hand, the repassivation currents of the Ni-Cr alloys were increased by chromium addition but the passivation rate was not enhanced during the short period of the straining electrode test. Auger analysis proved that enrichment of chromium in the film occurred only for the high chromium Fe-Cr alloys, but no enrichment occurred for the low Fe-Cr alloys and for every Ni-Cr alloy. The contribution of chromium addition for the repassivation behavior of the Fe-Cr and the Ni-Cr alloys was discussed by considering the effect of chromium on the film composition.

Chapter VIII dealt with the repassivation behavior of Fe-Cr-Ni ternary alloys containing various amount of iron and nickel with the constant amount of chromium of 18 mass%. The repassivation behavior was discussed with the results of Auger electron spectroscopy. The initial current density was affected by the structure of the newly created surface, which was determined by the structure of dislocation. The ferritic Fe-18Cr alloy showed a fairly larger current density compared with the austenitic Fe-18Cr-Ni alloys. On the other hand, the austenitic alloys showed similar changes in the current density in spite of the large difference in the Fe/Ni ratio. Auger analysis showed that a selective dissolution of iron enriched chromium in the film. Therefore, the chromium content in the film increased relatively with the increase in the iron content

in the substrate alloy. Difference in the SCC susceptibility between the ferritic alloys and the austenitic alloys were discussed in terms of the structure of alloy and the film properties formed on it.

Publications Relevant to the Thesis

The major part of the present thesis is based on the following publications.

1. Straining Electrode Behavior of Pure Iron in High Temperature and High Pressure Aqueous Solution.

   T. Shibata and S. Fujimoto : Trans. JIM, 25 (1984), 553.

2. Breakdown of Passivity on Pure Nickel by Sulfate ion in High Temperature Aqueous Solution.

   T. Shibata and S. Fujimoto : Corrosion, 41 (1985), 177.

3. Analysis of Anodic Behavior of Iron Electrode in High Temperature and High Pressure Aqueous Solution by Straining Electrode.

   T. Shibata and S. Fujimoto : Boshoku Gijutsu, 34 (1985), 72.

4. Straining Electrode Behavior of Pure Nickel in High Temperature and High Pressure Aqueous Solution Containing Sulphate Ion.

   T. Shibata and S. Fujimoto : Boshoku Gijutsu, 35 (1986), 276.

5. Repassivation Behavior of Newly Created Surface of Pure Nickel in High Temperature and High Pressure Neutral Solution.

   T. Shibata and S. Fujimoto : Trans. JIM (to be published).

6. Straining Electrode Behavior of Pure Iron in High Temperature and High Pressure Borate Buffer Solution.

   T. Shibata and S. Fujimoto : Trans. JIM (to be published).

7. Straining Electrode Behavior of Fe-Cr and Ni-Cr Alloys in High Temperature and High Pressure Borate Buffer Solution.

   T. Shibata and S. Fujimoto : Trans. JIM (to be published).

* Straining Electrode Behavior of Pure Iron in High Temperature and High Pressure Water.

T. Shibata and S. Fujimoto : Proc. 9th International Congress on Metallic Corrosion, Toronto June, 1984. Vol.3, p.526.

* Film Formation and Dissolution of Nickel in High Temperature and High Pressure Aqueous Solution.

T. Shibata and S. Fujimoto : Proc. 4th Asian-Pacific Corrosion Control Conference, Tokyo May, 1985. Vol.1, p166.